Charles University in Prague
Faculty of Mathematics and Physics

DOCTORAL THESIS

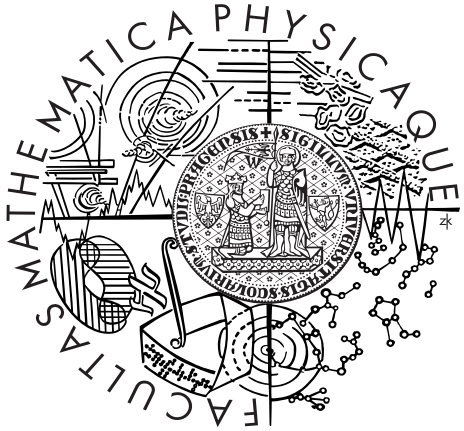

Jan Michálek

Source Parameters of Microearthquakes and their Uncertainties

Department of Geophysics

Supervisor of the doctoral thesis: Doc. RNDr. Tomáš Fischer, PhD.
Study programme: Physics
Specialization: Geophysics

Prague 2014

Acknowledgments

First of all I would like to thank my supervisor Tomáš Fischer for fruitful discussions and positive motivation during the whole PhD. study. Additionally, I would like to thank all my colleagues from the Department of Seismology of the Institute of Geophysics AS CR, namely Josef Horálek for many useful advices and kindness help, Alena Boušková for her support with processing of WEBNET data, Jana Doubravová for her help with SEISMON implementation, Václav Vavryčuk for providing the AMT code and specialized discussions, Hana Čermáková for providing double-difference locations, Bohuslav Růžek for discussions on the inversion problems and statistics and technical staff like Petr Jedlička, Josef Kotek and Jakub Klicpera for keeping the WEBNET seismic network running in the best possible conditions. My thanks also belong to Jiří Zahradník for his advices on attenuation aspects. Last but not least, special thanks go to my family, especially to my wife Pavla, for her ability to create suitable conditions and extraordinary patience during the finalization of the thesis.

The research was financially supported by the Grant Agency of the Charles University; grants No. 105707, *The type analysis of seismograms of earthquakes in West Bohemia* (2007) and No. 171310, *Source parameters of microearthquakes in West Bohemia and South Iceland* (2010-2012).

Prohlašuji, že jsem tuto disertační práci vypracoval samostatně a výhradně s použitím citovaných pramenů, literatury a dalších odborných zdrojů.

Beru na vědomí, že se na moji práci vztahují práva a povinnosti vyplývající ze zákona č. 121/2000 Sb., autorského zákona v platném znění, zejména skutečnost, že Univerzita Karlova v Praze má právo na uzavření licenční smlouvy o užití této práce jako školního díla podle § 60 odst. 1 autorského zákona.

V Praze dne .....

Název práce: Zdrojové parametry mikrozemětřesení a jejich neurčitost

Autor: Jan Michálek

Katedra: Katedra geofyziky MFF UK

Vedoucí: Doc. RNDr. Tomáš Fischer, PhD., Ústav hydrogeologie, inženýrské geologie a užité geofyziky, Přírodovědecká fakulta, Univerzita Karlova v Praze

Abstrakt: Náplní této práce je analyzovat spektrální metody používané pro určení zdrojových parametrů zemětřesení jako je seismický moment M_0 a rohová frekvence f_c a jejich aplikace na data ze západočeské seismické oblasti. Uvážením dalších předpokladů o zdroji lze dále odhadnout některé důležité parametry jako je poloměr zdroje *r* nebo pokles napětí ve zdroji $\Delta\sigma$. Určení parametrů je prováděno ve spektrální oblasti pomocí porovnání jednoduchého Bruneho modelu zdroje (nekauzální skluz na kruhové trhlině; spektrální spád ω^{-2}) se záznamem posunutí přímé P nebo S vlny. Metody byly aplikovány na 56 vybraných rojových zemětřesení z oblasti západních Čech z let 2000 a 2008 absolutním a relativním přístupem v několika modifikacích. Absolutní metoda kromě parametrů zdroje umožňuje získat také faktor kvality Q (útlum vlivem prostředí), který zásadním způsobem ovlivňuje určení f_c. Proto byla absolutní metoda aplikována také v modifikaci hromadné inverze, kdy je *Q* stabilizováno. Ukázalo se, že relativní metoda aplikovaná pomocí poměrů spekter trpí větší nestabilitou a nepřesností řešení. Výsledky obou metod nepotvrdily obecně předpokládanou platnost vzájemné podobnosti slabých a silných zemětřesení, pro kterou je uvažován konstantní pokles napětí. Neurčitost výsledků použitých metod a předpokladů jednoduchosti zdroje ovšem umožňuje pouze hrubý odhad parametrů zdroje.

Klíčová slova: zdrojové parametry, podobnost zemětřesení, spektrální analýza

Title: Source Parameters of Microearthquakes and their Uncertainty

Author: Jan Michálek

Department: Department of Geophysics

Supervisor: Doc. RNDr. Tomáš Fischer, PhD., Institute of Hydrogeology, Engineering Geology and Applied Geophysics, Charles University in Prague

Abstract: The aim of this thesis is to analyze the spectral methods used for the determination of the earthquake source parameters like the seismic moment M_0 and the corner frequency f_c and to apply these methods to seismic data from the West Bohemian region. Considering some assumptions about the source the other important parameters like the source radius r or the stress drop in the source $\Delta\sigma$ can be evaluated. Determination of the parameters is performed in the spectral domain by comparing a simple Brune's source model (non-causal slip on a circular rupture; spectral slope ω^{-2}) with the displacement of the P or S wave. The methods were applied to 56 selected earthquakes of the West Bohemian swarms from 2000 and 2008 by the absolute and relative approach in several modifications. The absolute method allows to determine not only the source parameters but also the quality factor *Q* (attenuation), which significantly affects the determination of f_c. Therefore, the absolute method was applied also as the joint inversion when *Q* is stabilized. It turned out that the relative method applied by using spectral ratios suffer from greater instability and uncertainty of the solution. The results of both methods did not confirm the generally expected self-similarity of weak and strong earthquakes for which the constant stress drop is considered. However, uncertainty of the results of the used methods and assumptions on the source simplicity allows only a rough estimate of the source parameters.

Keywords: source parameters, self-similarity of earthquakes, spectral analysis

Contents

Chapter 1

Introduction

Earthquake source and processes leading to the rupture of the Earth's crust are of interest since people had understood that shaking of the earth is not God's punishment but natural way of stress release locked inside the Earth crust. The milestone in understanding of the consequences was certainly the publication of the theory of continental drift by Alfred Wegener in 1915 (Wegener, 1966) which offered evidence that the Earth is alive and continents are moving and therefore most of the earthquakes occur on boundaries of the continents. First theoretical studies of the earthquake source itself are from the 1960s (Eshelby, 1957) when the theory of mechanics and seismic waves was understood and supported by laboratory experiments. After that many models of the earthquake source were developed theoretically (Haskell, 1964; Brune, 1970; Sato & Hirasawa, 1973; Boatwright, 1980) including the dynamic properties (Madariaga, 1976; Kostrov & Das, 1988) and their reliability was tested by comparison with the real seismograms. The first attempts were limited to very rough estimates of parameters like the size of the source, total radiated energy or final fault displacement (Haskell, 1964). With enhancing the quality of the seismic records, thanks to improved instrumentation, the analysis moved forward, but the unknowns that come from the material properties under the Earth's surface remained unresolved or were resolved only partially. This was probably the reason why the very approximate models of the source become that popular and widely used and applied in almost all seismically active regions. Even though the advanced physical source models were suggested and new sophisticated methods developed allowing to obtain, e.g. the time dependent distribution of the slip over the fault using the inversion of the full waveforms, there is still many unknowns (e.g. properties of the material and its heterogeneity) that bring high uncertainties to the source parameters estimates. Especially the attenuation of the seismic waves and its possible dependence on frequency is still an unresolved problem. Despite the adopted simplifications these methods provide the first necessary estimates of the source parameters that represent a starting point for further more sophisticated analysis. Accordingly I applied one of the most frequently used approaches to the data from the West Bohemia region and evaluated not only the limited number of parameters of the source but also their uncertainties and compared them with results from other studies around the world.

Chapter 2

Theory and Methods

2.1 Source models

According to the description complexity the model can be divided into multiple categories. The complexity of the model we are able to incorporate is conditioned by the quality and amount of the data, which are available in the area of study. This includes not only the quality of the waveforms and focal sphere coverage of the region by stations but also properties of the Earth's model. In the following the types of source models are introduced. Overview of the source model development can be found in, e.g. Gibowicz & Kijko (1994).

The basic classification of earthquake source models is represented by the point source models and finite source models. Finite source does not mean that such source has a finite length but that the distance of the station from the source is in orders comparable to the length of the fault so we can not simplify it by a point source. We could of course apply the finite source model even to a small earthquake but usually scanty information in the observed data would lead to a poorly conditioned inversion of the source parameters.

The finite source models can be divided into two groups – kinematic and dynamic models. Kinematic model is a model of a slip history of the rupture on a fault with arbitrarily specified propagation of the rupture whereas dynamic model describes the rupture propagation on fault based on fracture mechanics (Madariaga, 2011). Kinematic models describe the fracture as a dislocation while the dynamic models describe fracture as a crack (Kostrov & Das, 1988). A dislocation is considered to be a defect in an ideally elastic or viscoelastic medium formed by cut along a given surface and a finite relative displacement of the two faces of the cut, which means that the dislocation is represented by a discontinuity in the displacement; models of this type are the propagating dislocation model of Haskell (1964) and the model of Brune (1970), which assumes an infinite rupture velocity but is rationalized in terms of the dynamic properties of the source (Gibowicz & Kijko, 1994). [1] If the slip on the fault is calculated

[1] In contrast to dislocation models, in crack models an explicit account of the driving and resisting stresses in the source region is taken, and the resulting slip is derived by solving the equations of motion. Thus, to describe the fracture at an earthquake as a crack, it is necessary to know the initial distribution of stress on the fracture surface before the earthquake and the laws governing the fracture propagation

from the stress drop and strength of the fault, the dislocation model is identical to a crack model. The solution to static slip of a circular shear crack is very well known (e.g., Madariaga, 1983). Kinematic dislocation models are simpler than the dynamic cracks, whose physical description is more proper, but parametrization of the kinematic models allows to describe the source processes which are sufficiently realistic (Gibowicz & Kijko, 1994).

2.1.1 Point source model

The earthquake source can be described by more or less complex model. The simplest model is a point source buried in an elastic continuum Madariaga (2011). To describe the properties of this source we can use the equation of elastodynamics, where the zero net force and zero net moment conditions have to be fulfilled. Very good description can be achieved by combination of three orthogonal linear dipoles which together creates a symmetric tensor of rank 2 that is called the seismic moment tensor:

$$\mathbf{M} = \begin{bmatrix} M_{xx} & M_{xy} & M_{xz} \\ M_{xy} & M_{yy} & M_{yz} \\ M_{xz} & M_{yz} & M_{zz} \end{bmatrix} \tag{2.1}$$

The off-diagonal components represent the torque produced by two point forces of direction i separated by infinitesimal distance in direction j. The diagonal elements represent linear dipoles. Radiation of this point moment tensor in a homogeneous, linear elastic medium forms a set of Green functions. Our approximation of source is a point source and we can separate seismic moment tensor into two parts $\mathbf{M} = \mathbf{M_0}(t)\,\delta(r - r_0)$. Its time-dependent part can be written as

$$\mathbf{M_0}(t) = \mathbf{M_0}\Omega(t) \tag{2.2}$$

where M_0 is time-invariant tensor that describes the geometry of the source and $\Omega(t)$ is the time variation of the moment, the source time function.

2.1.2 Finite source models

Source time function

The source time function (STF) is the earthquake signal produced by the faulting. STF is shaped by more processes happening in the source. The main quantities which describe duration of the processes are the rupture duration time T_D and the rise time τ (or characteristic time; Gibowicz & Kijko, 1994). Rupture time T_D is time needed for faults of finite length to propagate the rupture along the fault (neglecting the directivity now)

$$T_D = L/v_r \tag{2.3}$$

and interaction of the fault faces. The distribution of the displacement on the fault becomes then one of the unknowns. (Gibowicz & Kijko, 1994)

where v_r is the rupture velocity and L is the characteristic dimension (or maximum size) of the fault plane (Stein & Wysession, 2003). Rise time τ is duration of the slip function $\Delta u(t)$ from zero to its maximum value at any point on the fault (Stein & Wysession, 2003)

$$\tau = \frac{\mu \bar{D}}{\Delta\sigma\beta} \tag{2.4}$$

where μ is rigidity (or shear modulus), $\bar{D}$ is the average dislocation on the fault, $\Delta\sigma$ is the stress drop and β is the S-wave velocity. STF is then convolution of the derivative of the slip function and the rupture propagation history. For small sources and local seismic network we are usually unable to distinguish between these two processes but the time width of the displacement pulse is generally assumed to be related to duration of the rupture.

Kinematic source models

Shape of the STF depends on the geometry of the fault and on the form how the accumulated stress is released. Numerous source models were suggested and analyzed during the last forty years and I tried to select and describe the most often ones used for analysis of small earthquakes. Usually models of circular shape are used and mainly differ by the history of the stress release and by the speed of the rupture.

Brune (1970) derived a simple source model for small earthquakes for S waves where the pulse shape of the far-field displacement is given by Snoke (1987)

$$u(t) = \Omega_0 \frac{t}{\tau^2} H(t) \exp(-\frac{t}{\tau}) \tag{2.5}$$

where Ω_0 is the amplitude low-frequency spectral level (or plateau) where $\Omega_0 \sim \Omega(f \rightarrow 0)$ and $H(t)$ is the Heaviside function. Amplitude spectrum of such pulse is then

$$|U(f)| = \frac{\Omega_0}{\left[1 + \left(\frac{f}{f_c}\right)^{\gamma n}\right]^{1/\gamma}} \tag{2.6}$$

where f_c is the corner frequency of the earthquake, $\gamma = 1$ and n is the high-frequency spectral falloff (for Brune model $n = 2$). Main advantage of this model is its simplicity. It assumes an instantaneous shear stress release on a circular dislocation (Snoke, 1987). Radius of such circular fault is

$$r = \frac{k_c \beta}{f_c} \tag{2.7}$$

where k_c is the model dependent constant. In case of Brune model $k_c = 0.37$ and is not dependent on the angle of observation and only S waves are considered (Gibowicz & Kijko, 1994). This model has been heavily used and published in numerous studies. Based on results from mines Gibowicz & Kijko (1994) summarizes that this model gives considerably bigger radius than observed in the underground.

Further, quasidynamic circular model was developed by Madariaga (1976) who studied a plane circular faulting with fixed rupture velocity. The model is quasidynamic since the effective stress on the fault is specified (Gibowicz & Kijko, 1994). For this model k_c

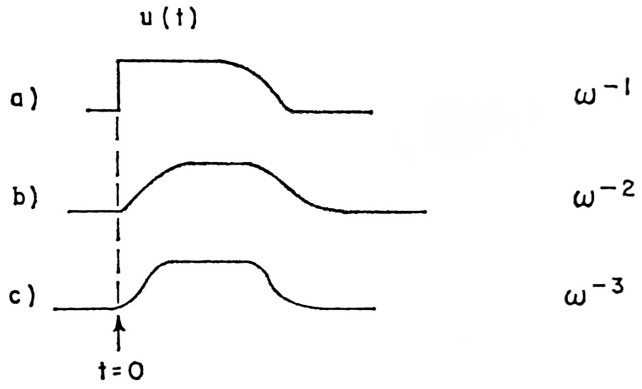

Figure 2.1: Possible pulse shapes of the STFs and their spectral high-frequency falloffs (after Savage, 1972)

is a function of azimuth (i.e. angle between the fault and ray direction) but in case of sufficiently dense network coverage one can apply the average values of the coefficients.

Another modification of the circular source model was developed by Boatwright (1980) who analyzed circular models where the region of stress relaxation grows with a uniform rupture velocity until the rupture front either decelerates continuously or stops abruptly. For this class of models he obtained steeper high-frequency falloff and therefor he used $\gamma = 2$ in Eq. (2.6). Many other kinematic models with circular rupture were proposed, e.g. Savage, 1966; Molnar et al., 1973; Sato & Hirasawa, 1973 (overview in Aki & Richards, 2002), and differ mainly by the shape of the slip function and how the fault rupture is developed and healed. Although the physical reality and causality of the source model is important, it is not possible to reliably obtain such details from the surface observations.

Shape of the STF influences the high-frequency falloff value n. Overview of the basic STF pulse shapes with their spectral high-frequency falloffs is shown in Fig. 2.1.

2.2 Theory of earthquake source

2.2.1 Representation theorem for displacement

The displacement field u_n for any dislocation source (represented by the double couple of acting forces) can be described in the form

$$u_n(x,t) = M_{pq}(\xi,t) * G_{np,q}(x,\xi,t) \tag{2.8}$$

(Aki & Richards, 2002; Jost & Herrmann, 1989, eq. 3.23) where M_{pq} is the time dependent moment tensor of the source which is equal to the integral of the moment density over the fault surface and $G_{np,q}$is the derivative of a Green function which describes the response of the media to the unidirectional unit impulse, or simply describes the medium in which the wave propagates. If the properties of the media are known the source term can be separated and analyzed.

2.2.2 Seismic moment

Seismic moment, as a measure of the size of the earthquake in relation to the ruptured area, is defined as

$$M_0(t) = \mu \bar{D} S \tag{2.9}$$

(Aki & Richards, 2002, eq. 3.16) where μ is the rigidity (or shear modulus), $\bar{D}$ is the average dislocation on the fault and S is the fault area.

Another expression of the seismic moment is possible to get from the moment tensor which can be divided into two independent functions

$$\mathbf{M}(\xi, \mathrm{t}) = \mathbf{M}(\xi)\, \Omega(t) \tag{2.10}$$

where $M_{pq}(\xi)$ is the time-independent moment tensor and $\Omega(t)$ is the source time function, which defines the dislocation function on the fault. The moment tensor $M_{pq}(\xi)$ describes the geometry of the source whereas the source time function describes the amplitude of displacement in time. Seismic moment can be decomposed as

$$M_0(t) = M_0\, \Omega(t) \tag{2.11}$$

where M_0 is the scalar seismic moment of an earthquake and can be expressed from any moment tensor $\boldsymbol{M}(\xi)$ using the suitable norm, e.g.

$$M_0 = \frac{1}{\sqrt{2}} \left(\sum_{ij} M_{ij}^2 \right)^{1/2} \tag{2.12}$$

(Silver & Jordan, 1982; Gibowicz & Kijko, 1994, eq. 9.97; Shearer, 2009, eq. 9.8). The norm can be defined variously and therefore the scalar seismic moments can vary in different studies using different norms and also can differ from results obtained by the definition (2.9). [2]

Displacement in the far field in the homogeneous media due to a point source dislocation of strength $M_0(t)$ is

$$\mathbf{u}(\mathrm{x}, t) = \frac{1}{4\pi\varrho\alpha^3} \Re_\alpha \frac{1}{R} \dot{M}_0 \left(t - \frac{R}{\alpha} \right) + \frac{1}{4\pi\varrho\beta^3} \Re_\beta \frac{1}{R} \dot{M}_0 \left(t - \frac{R}{\beta} \right) \tag{2.13}$$

(Aki & Richards, 2002, eq. 4.32) where α and β are velocities of seismic waves and $\Re_\alpha$ and $\Re_\beta$ are the corresponding radiation pattern (RP) corrections (for details see Aki & Richards, 2002, eq. 4.33). Quantity ρ is density and R is the hypocentral distance. The important message in this equation is that in the far-field we observe a derivative of the permanent displacement step in the source. Therefore the seismic moment in the far field is proportional to the integral value of the displacement pulse and in frequency domain it corresponds to the low frequency spectral plateau Ω_0 (Fig. 2.2). From (2.13)

[2] Units of the seismic moment can be ambiguous. SI units are Nm but in older works usually dyn.cm units are used instead (1 Nm = 1e7 dyn.cm; 1 N = 1e5 dyn).

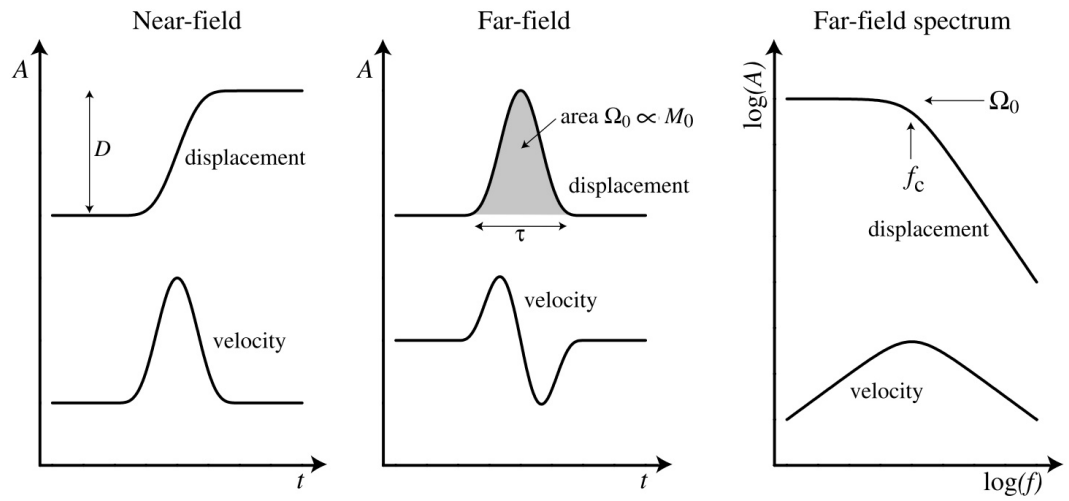

Figure 2.2: The relationships between near-field displacement and far-field displacement and velocity for time series (left two panels) and spectra (right panel).(after Shearer, 2009, Fig. 9.13)

we can formalize the relation for seismic moment

$$M_0 = \frac{4\pi\rho c^3 R\Omega_0}{\Re_c F_c^{surf}} \tag{2.14}$$

where c is the velocity of seismic wave (α or β), $\Re_c$ is corresponding radiation pattern correction and F_c^{surf} is corresponding free surface correction. Calculation of the seismic moment is independent of the source model.

The contribution of P and S wave to displacement amplitude is given by ratio α^3/β^3 which is approximately ~ 5 (neglecting the radiation patterns). This fact is favoring the use of the S waves for analysis because of better signal-to-noise ratio but one should keep in mind that for small hypocentral distances (~ 20 km) the S wave can be contaminated by successive reflections of the P phase or other scattered phases. As the P phases in the West Bohemia region are clear and mostly simple, I prefer this type of waves.

The basic criterion which tells us what details in data we have to take into account and what we can neglect can be described by the distance of an observer to the source. It tells us whether to use the far-field approximation or if the near-field terms are also important. To use the far-field approximation we have to fulfill the criterion

$$L^2 \ll \frac{1}{2}\lambda R \tag{2.15}$$

(Aki & Richards, 2002, eq. 10.12), where L is the characteristic dimension (or maximum size) of the fault plane, λ is the maximum observed wavelength and R is the hypocentral distance.

2.2.3 Size of the source

The corner frequency f_c (or its reciprocal value) is the only quantity which characterizes the duration of the rupture processes. To relate this duration to the size of the zone on which the slip occurred we have to apply one of the source models. In this study I use an approximation after Madariaga (1976). The source radius is calculated according to (2.7) and if I assume that the rupture velocity v_r is 0.9β, then $k_\alpha = 0.32$, $k_\beta = 0.21$ and $\beta = 3.5$ km/s. Model of Madariaga (1976) expects the ratio between corner frequencies of P wave and S wave of about 1.5 ($f_c^P/f_c^S = 1.5$). Here I want to stress that all uncertainties in f_c will transfer to uncertainties of the source radius.

2.2.4 Stress drop

The amount of energy released by the earthquake is determined by the difference between the initial stress before the earthquake and the final stress level after (e.g. Madariaga, 1983). During the rupture the strain accumulated near the fault is released and part of the energy is released in seismic waves (approx. 1/10 of the total energy). For a finite fault we define the static stress drop as stress drop integrated over the fault area normalized by the fault area. Approximating the fault area by a square with side of length $\widetilde{L}$ (characteristic dimension) with an average displacement $\bar{D}$ the static stress drop is related to the strain change $\bar{D}/\tilde{L}$ and according to Hook's law

$$\Delta\sigma = C\mu\frac{\bar{D}}{\widetilde{L}} \tag{2.16}$$

where C is non-dimensional constant that depends on the fault geometry (Lay & Wallace, 1995). For a circular shape with radius r the constant $C = {}^{7\pi}/_{16}$. By substitution of μ from (2.9) we get

$$\Delta\sigma = \frac{7}{16}\frac{M_0}{r^3} \tag{2.17}$$

which is relation obtained by Eshelby (1957). Assuming that $\Delta\sigma = f(C, M_0, r)$ where $r = v_R T_D$ (v_R is the rupture velocity) the uncertainty of stress drop is of a factor 2–3 (having uncertainty of C about 50 % and 25 % of the following quantities; Stein & Wysession, 2003, p. 271). Looking at (2.17), the possible error in r (i.e. f_c) is transferred into the error of stress drop with the third power. This is why one should be cautious when interpreting the results because increase of the corner frequency f_c only by 20 % will double the stress drop $\Delta\sigma$. Relation (2.17) was derived for a circular rupture buried in a homogeneous infinite material which is not valid in the vicinity of the earthquake asperity and also the Hook's law in not valid here and this brings another uncertainty to $\Delta\sigma$. A number of modeling assumptions are made but they are still very likely different from the real physics of the rupture processes; e.g. variations in rupture speed will cause a change in corner frequency even if the stress drop remains constant (Shearer, 2009). Therefore values of the stress drop are only rough estimates and credibility of these values should be considered to be accurate in terms of orders. The stress drop (2.17) is sometimes referred as *Brune-type* stress drop.

2.2.5 Apparent stress

Another quantity characterizing the earthquake process is the apparent stress which is a ratio of radiated energy E_c to seismic moment M_0

$$\sigma_a = \mu \frac{E_c}{M_0} \tag{2.18}$$

(Boatwright, 1984), where index c is related to the specific type of wave (either α or β). This relation expresses the efficiency of the energy radiation. First was assumed that the apparent stress should be constant for all earthquakes but many studies show (e.g. Aki, 1967; Kanamori & Anderson, 1975; Mayeda et al., 2005) that the self-similarity may not be valid for all. But it is still question whether the non-self-similarity is real or comes from uncertainties in estimation of the E_c, M_0 parameters, predominantly the first one. The radiated energy E_c of a particular wave can be calculated from the observations of displacement as

$$E_c = 4\pi\rho\alpha \left\langle \Re_c \right\rangle^2 \frac{R^2}{\Re_c^2} J_c \tag{2.19}$$

(Boore & Boatwright, 1984), where $\langle \Re_c \rangle$ is the average radiation pattern correction which equals to 0.52 and 0.63 for P waves and S waves, respectively. $\Re_c$ is radiation pattern correction for the particular focal mechanism at the particular station. The energy flux J_c is calculated from the squared velocity spectrum as

$$J_c = 2 \int_0^\infty |\dot{u}(f)|^2 df \tag{2.20}$$

integrated over the whole frequency range. The integration, which is in reality strongly band limited, introduces quite large uncertainty to the energy flux and into all quantities derived from it subsequently. As seismologists often work with data from a narrow frequency band, the correction terms to J were introduced by Snoke (1987)

$$J_c = 2\pi \frac{2}{3} \left[\Omega_0 f_1\right]^2 f_1 + 2 \int_{f_1}^{f_2} |\dot{u}(f)|^2 df + 2|\dot{u}(f)|^2 f_2 \tag{2.21}$$

where f_1, f_2 are the instrument band limits or f_1 can be related to reciprocal value of the window length and f_2 to the Nyquist frequency (Gibowicz & Kijko, 1994). According to Snoke (1987) the determination of J_c is totally objective for spectra from broadband instruments and contribution from the correction terms is up to 10 per cent. However, our band limits from 1 to 100 Hz are not broadband and I found that contribution of the high frequency correction term is up to 50 per cent. Ide & Beroza (2001) analyzed the effect of finite bandwidth on energy estimation and found that integration up to approximately ten times the corner frequency is necessary to approach 90 % of the seismic energy. Otherwise the energy estimates may be biased.

Corner frequency - Snoke's approach

As a second approach to retrieve the corner frequency I applied the method of Andrews (1986) and Snoke (1987, eq. 3), which uses the integral of the square of the ground velocity spectrum J (after the attenuation correction; including the correction for limited bandwidth) for direct determination of f_c from the spectrum without the need of inversion:

$$f_c(J) = \left(\frac{J}{2\pi^3 \Omega_0^2} \right)^{\frac{1}{3}} \tag{2.22}$$

This kind of derivation of corner frequency can be easily automated if J and Ω_0 are estimated correctly.

2.3 Signal processing

The recorded displacement at the surface $u(t, R)$ can be decomposed as

$$u(t, R) = \Omega(t) * g(R) * i(t) * p(t) * l(t) \tag{2.23}$$

where $\Omega(t)$ is the source time function, $g(R)$ represents the earth structure as a function of position R, $i(t)$ is the instrument response of the seismometer, $p(t)$ is the anelastic attenuation along the ray path, $l(t)$ is the site effect and $*$ is operator for convolution (e.g., García-García et al., 1996). Transforming this relation to frequency domain using the Fourier transform the form simplifies from convolution in time domain into multiplication in frequency domain

$$U(\omega, R) = \Omega(\omega) G(R) I(\omega) P(\omega) L(\omega) \tag{2.24}$$

where $\omega = 2\pi f$. To get the source time function $\Omega(t)$ we need to remove the other effects behind this term or to make some approximation. The geometrical spreading term $G(R)$ is frequency independent and influences the amplitude of the signal only. The next terms are analyzed in more details in following sections.

2.3.1 Instrumental correction

Instrumental correction is one of the fundamental correction which is applied to the signal routinely. The impulse response (or transform function) of all the modern seismometers is known and described in the documentation of the instrument. If we are processing data from the full frequency range of the instrument the application of the correction is necessary. But if we are processing the signal in a limited frequency band where the response is flat with respect to the recorded quantity, the correction is not needed. It always depends on the ratio of the corner frequency of the analyzed event f_c and the instrument corner frequency f_{ic}.

In Fig. 2.3 the instrument response is simulated by the high-pass Butterworth filter of 2^{nd} order with different corner frequencies $f_{ic} = f_{HP}$ and is applied to the pulse signal

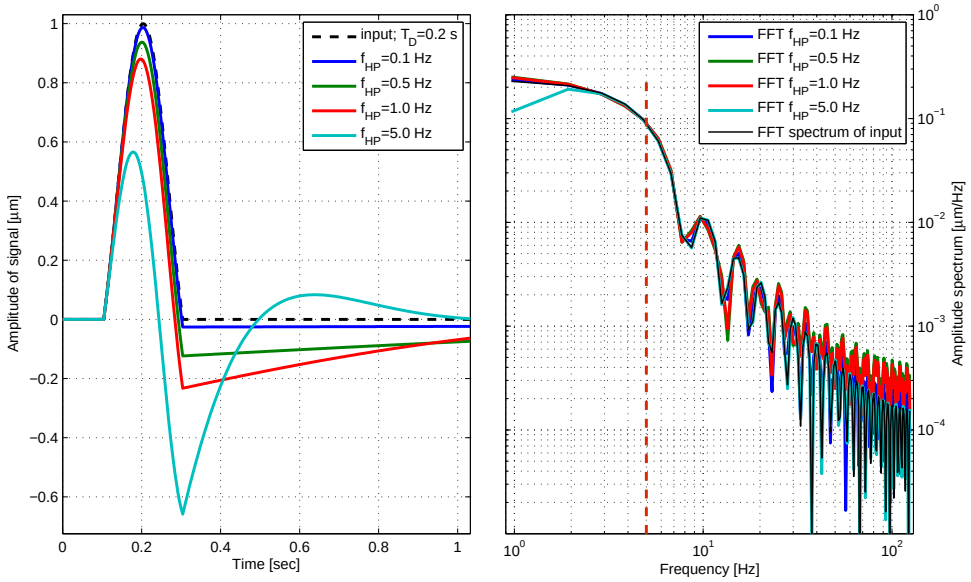

Figure 2.3: Effect of high-pass filtration on the pulse signal of width T_D= 0.2 sec (f_c= 5 Hz) and their FFT spectra. The Butterworth filter of 2^{nd} order is used with different stop-frequencies f_{ic} = 0.1, 0.5, 1.0 and 5 Hz (which corresponds to ratios f_c/f_{ic} = 50, 10, 5 and 1, respectively). The vertical red line shows the f_c = 5 Hz.

of width T_D= 0.2 sec (f_c= 5 Hz). If the ratio f_c/f_{ic} is higher than 50, the influence of the instrument to the signal in time domain is negligible. Decreasing the f_{HP} to value 1 and lower makes serious distortions of the signal in the time domain. Nevertheless, it has minimum influence to the spectra even for the low f_c/f_{ic} values. It does not shift the corner frequency of an event f_c at all and only decreases the spectral amplitude for the very low frequencies. It change the high frequency asymptote also but with respect to oscillations in the high frequency part it is unsubstantial. [3]

In the case of WEBNET data, all the earthquake corner frequencies are at least ten times higher than the corner frequency of the instruments and consequently the instrument correction $I(\omega)$ is not needed. Therefore the analysis is carried out in the interval of the flat response of the instrument (which corresponds to the green curve in Fig. 2.3; $f_{HP} = 0.5$ Hz).

2.3.2 Effect of attenuation

As the Earth crust is not ideally elastic the geometrical spreading and conversion of waves on boundaries are not the only effects that influence the amplitude of the signal. Part of the energy is lost due to irreversible transformation of potential energy into kinetic energy of seismic waves and the related internal friction. This process is called anelastic (intrinsic) attenuation and it can be described by quality factor Q which represents fractional loss of energy per cycle of oscillation

[3] All the simulation is done for the same sampling frequency 250 Hz as the WEBNET data and in 1 sec window length.

$$Q = -\frac{2\pi E}{\Delta E} \tag{2.25}$$

(Lay & Wallace, 1995) and can be simply obtained by a ratio of amplitudes of successive cycles of oscillations

$$Q = \frac{\pi}{ln\left(\frac{A_1}{A_2}\right)}$$

We can write the loss of amplitude as a function of time

$$A(t) = A_0 e^{-\omega_0 \frac{t}{2Q}} = A_0 e^{-\pi f_0 \frac{t}{Q}} \tag{2.26}$$

where $\omega_0 = 2\pi f_0 = \frac{2\pi}{T_0}$ is the prevailing frequency of the wave. Substituting $t = x/c$ into (2.26), where c is the velocity of the wave, the decrease of amplitude can be also expressed as a function of distance $A(x)$. Here we see that for constant Q the amplitudes at higher frequencies will attenuate more than at lower frequencies. It is generally observed that Q is independent of frequency in the range from 0.001 to 0.1 Hz (Fig. 2.4). This frequency independence of Q is inconsistent with the basic physical model of anelasticity which assumes viscoelastic material with greatest attenuation at absorption peak occurring at $\omega\tau = 1$, where τ is the relaxation time constant (Stein & Wysession, 2003). This inconsistency is thought to be explained by superposition of many different mechanisms of absorption, which finally results in a relatively constant Q-value in a broader frequency band. But frequency dependence of Q at frequencies higher than 1 Hz, which I am interested in, is not explained satisfactorily.

Futterman (1962) derived from dispersion of the body waves the following dependence of Q on frequency

$$Q(\omega) = Q_0(1 - \frac{1}{\pi Q_0} ln \frac{\omega}{\omega_0}) \tag{2.27}$$

where Q_0 is quality factor for a specific nominal frequency and $\omega = 2\pi f$. But this relation has a minimal effect on change of $Q(\omega)$ as in our frequency range 1–80 Hz the change of $Q(\omega)$ is up to 2 % only. On the other hand Müller (1983) introduced a power law dependence

$$Q(f) = Q_0 f^n \tag{2.28}$$

where $n = \langle 0.4; 1.1 \rangle$ for the frequency interval from 1 to 30 Hz (Gibowicz & Kijko, 1994, p.163). Oth et al. (2011) obtained $Q_0 = 50 - 130$ and $n = 0.6 - 0.9$ for the southern part of Japan. Such dependence would significantly influence the results because assuming even the weakest frequency dependence $n = 0.4$ the difference for frequencies 1 Hz and 80 Hz would make about 580 %. Generally is observed that Q depends on frequency at higher frequencies and increases with frequency (Lay & Wallace, 1995). Most of the studies derived the attenuation factor Q_c from coda waves whose behavior can be different to attenuation of direct waves.

The Q factor is generally increasing with depth because the structure of the rock is more compact and the micro fractures are closing with increasing lithostatic pressure.

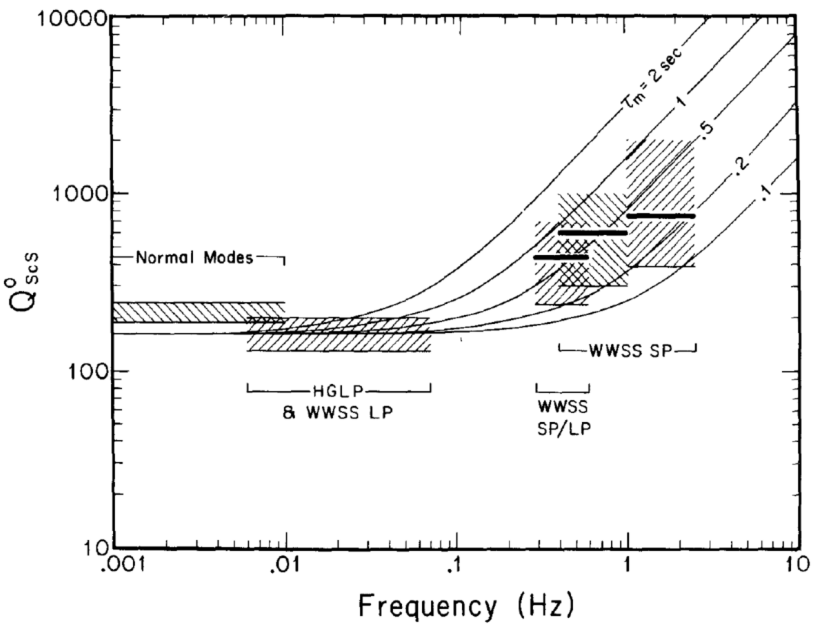

Figure 2.4: Dependence of Q on frequency (after Sipkin & Jordan, 1979).

Despite the major part of the travel path is in the low-attenuating material even the thin surface low-Q layer can cause very strong reduction of amplitude recorded at the surface. This is why the stations tend to be placed in the boreholes either for high detection capability of small earthquakes or for the low distortions of the signal. The effects of attenuation can be described also by an average attenuation operator along the whole raypath

$$t^* = \int_{path} \frac{dt}{Q} = \sum_{i=1}^{N} \frac{t_i}{Q_i} \tag{2.29}$$

where t is the travel time and index i marks individual layers. The near surface attenuation κ (or site effect) is sometimes introduced for the surface layer which can be represented as an attenuation operator $t_1^* = t_1/Q_1$ of the topmost layer.

The frequency-dependent attenuation term in (2.24) is expressed by anelastic attenuation along the path $P(f) = exp[-\pi f t/Q]$ and site effect $L(f) = exp[-\pi f \kappa]$. The unknown parameters t/Q and κ show the same functional dependence on frequency, which makes the distinction between these two impossible without a preceding knowledge of the Q values. Accordingly, I can omit κ and include the appropriate near surface attenuation into a single attenuation term $exp[-\pi f t^*]$. This approach can be justified when the hypocentral area is small and rays are traveling along very similar paths, which is valid for the most seismic activity in the West Bohemia region (see Fig. 3.1).

Despite this discussion of frequency dependence of quality factor, most of the studies regarding the source parameter estimations are using the constant value of Q which is related to the specific wave, either P or S. Sometimes the Q_α or Q_β are derived from Q_c (the coda-Q factor), where $Q_\alpha = 9/4\, Q_c$ (e.g., García-García et al., 1996).

The effect of attenuation on the spectra is shown in Fig. 2.5 where different Q-values ranging from 100 to infinity (curve named Brune) are applied to the spectrum of

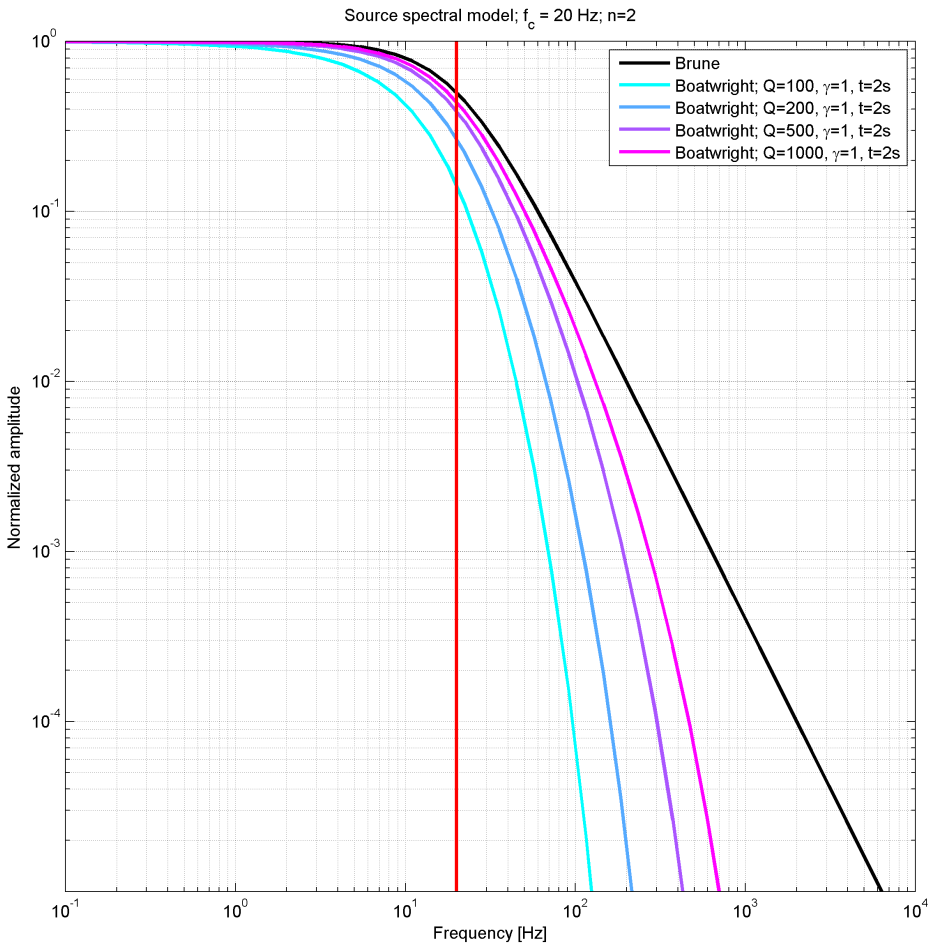

Figure 2.5: Effect of attenuation on the spectra and its relation to f_c

one-sided displacement pulse with $f_c = 20$ Hz. Neglecting of attenuation would lead to underestimation of f_c in the absolute spectral methods.

So for retrieving the amplitude source spectrum $\Omega(\omega)$ two effects must be corrected for: the anelastic attenuation (amplitude decrease with distance and broadening of the pulse in the time domain) and the geometrical spreading (decrease of amplitude with the distance).

2.3.3 Spectra estimation

The way of amplitude spectra estimate affects both the resulting corner frequency f_c and the low frequency level of the amplitude spectrum Ω_0. I have tested two approaches for spectra estimation: the standard fast Fourier transform (FFT; *fft* function in MATLAB) using the 10 % cosine taper and the multitaper approach (MTT; *pmtm* function in MATLAB) that gives smoother spectra. I found that the MTT must be applied with care because using low values of the time-bandwidth product (parameter NW), which favorably flattens the high frequency amplitude oscillations, leads to an artificial increase of corner frequency whereas the high values of NW are lacking of any advantages of MTT compared to FFT in this analysis. Nevertheless, the MTT method is more stable

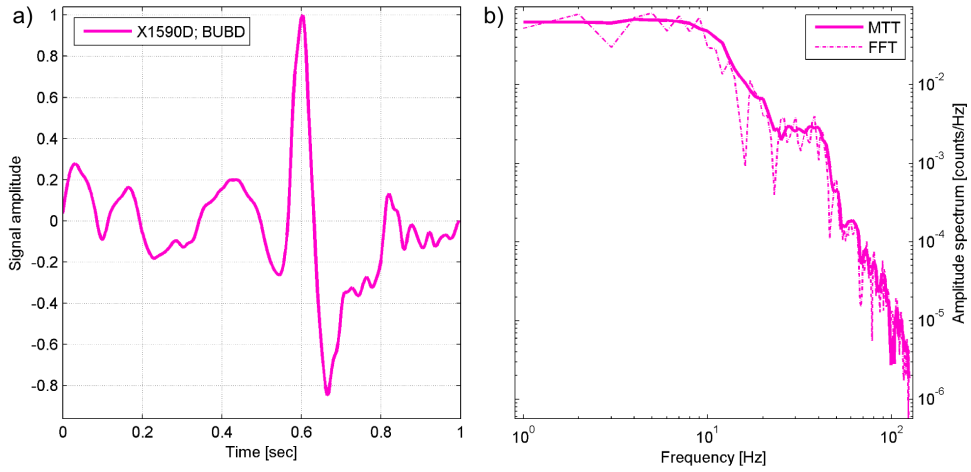

Figure 2.6: Comparison of standard FFT and the MTT method for estimation of the spectra. a) Vertical displacement of the P wave at station BUBD for event X1590D and b) its spectra using FFT method (dashed line) and MTT method (solid line).

also for the low frequency spectra amplitudes where the MTT is less oscillating than the FFT. I demonstrate this effect on the real displacement seismogram in Fig. 2.6 where $NW = 4$ (number of orthogonal Slepian filters is $NS = 2 * NW - 1$). The signal is sampled by 250 sps and is 1 sec in length. In this test the signal of the same length is used as for the real data processing to test also the effect of the window length on the spectral estimate.

As the MTT here is using seven orthogonal tapers it is important to keep the analyzed signal in the middle of the time window (but this effect is not analyzed in this study). In processing of real data in the SEISMON this is assured by fixing the position of the P-wave onset in the middle of the time window.

2.4 Absolute methods

2.4.1 Spectral analysis

The frequency analysis is a common and extensively used method for obtaining basic estimates of the source parameters (e.g. recent studies: Abercrombie & Rice, 2005; Allmann & Shearer, 2007; Dobrynina, 2009; Kwiatek et al., 2011) since the theoretical spectrum of circular rupture model was presented by Brune (1970). Although other improved and more realistic models of earthquake source were proposed (e.g., Sato & Hirasawa, 1973; Boatwright, 1980) I use the Brune (1970) source model because it is widely used and therefore a comparison with other studies can be performed. The advantage of this model is its simplicity. Commonly observed ω^{-2} spectral high-frequency falloff (e.g., Andrews, 1986; Abercrombie, 1995; García-García et al., 1996; Shi et al., 1998; Oth et al., 2010) fits our data well. More precisely, the observed spectra can be adapted to this model by finding the appropriate Q-value. I assume this model being sufficient to describe the sources of $0.8 \leq M_L \leq 3.3$ micro earthquakes at

hypocentral distances of about 6 – 30 km in the West Bohemia region.

For determination of the source parameters I firstly used the absolute spectral approach applied to P waves on the vertical component. The method is designed for routine processing of seismograms from the WEBNET network and is implemented in the SEISMON processing package (described in Appendix A; Mertl & Hausmann, 2009; Michálek et al., 2011). A time window of 1-sec duration was used to calculate the spectrum. It contains 0.5 sec of noise and the remaining part includes the signal of the P wave with almost 100 % of its energy. The noise spectrum was calculated from the first half of the time window and replicated while the spectrum of the signal was calculated from the whole window (Fig. 3) using the MTT. The spectrum was interpolated in order to obtain equidistant frequency spacing in the logarithmic scale (12 points per decade). I did not apply any smoothing operator because the MTT itself smooth the spectrum naturally. The resulting displacement spectra were compared to the model

$$\Omega(f) = \frac{\Omega_0 e^{-\pi f t/Q}}{1 + \left(\frac{f}{f_c}\right)^n} \tag{2.30}$$

(Brune, 1970) with the attenuation term $e^{-\pi f t/Q}$, where Ω_0 is the low frequency spectral level proportional to the seismic moment M_0, t is the P-wave travel time, Q is the quality factor for the whole ray path, f_c is the corner frequency and $n = 2$. The exponential term is responsible for the anelastic attenuation along the ray path. Because I assume a point source (i.e. no effects of source directivity), f_c is assumed to be the same for all stations. The inversion process itself is described in section 3.3.3. Parameters of the source are then derived using formulas (2.7), (2.14) and (2.17).

Various modifications of inversion are used in order to test the stability of the determined parameters. A common f_c for all stations is always assumed and two approaches to obtain Q are applied: (1) a separate Q is determined for each event and station and (2) a common Q is determined for each station using a joint inversion of all events. The details are described in sections 3.3.3 and 3.3.4.

2.5 Relative methods

2.5.1 Spectral ratios - EGF

Absolute methods of the source parameters determination suffer from uncertainties rising from the path effects distortions to the signal. There is a possibility to remove these effects by application of the empirical Green's function (EGF) technique (Hartzell, 1978; Mueller, 1985; Mori & Frankel, 1990). The EGF method (or spectral ratio method) is well known and widely used for analysis of collocated events in variable environments from picoearthquakes (e.g. Kwiatek et al., 2011), microearthquakes (e.g. Abercrombie & Rice, 2005; Fischer, 2005) to big mainshock-aftershock sequences (e.g. Ammon et al., 1993; Plicka et al., 1998; Baltay et al., 2011; Wen, 2014). In this method the weaker event is assumed to be a delta function $\delta(t)$ with respect to the stronger event. Aim

of the EGF method is to separate the STF from the stronger event by deconvolution of the weaker event. In an ideal case, the division of the spectra will remove all effects except for the source properties. The main advantage of this method is that almost all path and site attenuation effects are eliminated by the spectral division. The spectral ratio by using (2.24) is simplified to

$$\Psi^{obs}(f) = \frac{U_1(f)}{U_2(f)} = \frac{\Omega_1(f)}{\Omega_2(f)} \tag{2.31}$$

where $U_1(f)$ and $U_2(f)$ are the displacement spectra of the stronger and weaker events, respectively. The $\Omega_2(f)$ term is the spectrum of the weaker event which has nearly flat amplitude up to its corner frequency f_{c2} and is considered to be similar to a spectrum of the $\delta(t)$ pulse. To apply this technique the following criteria have to be met (e.g. Shearer, 2009; Kane et al., 2011):

1. The events are closely collocated
2. Difference in magnitudes of the events is higher than 1.0 so that the smaller event could be considered as $\delta(t)$
3. Both events have similar focal mechanism, i.e. similar geometry of the source

In addition to criteria above an assumption of the source model have to be included to obtain its parameters. In this study the Brune source model (2.6) is used to be consistent with results from the absolute approach. The spectral ratio is then defined as

$$\Psi^{mod}(f) = \Omega_{0r} \frac{1 + \left(\frac{f}{f_{c2}}\right)^2}{1 + \left(\frac{f}{f_{c1}}\right)^2} \tag{2.32}$$

(e.g. Viegas et al., 2010) where $\Omega_{0r} = \Omega_{01}/\Omega_{02}$ is the low-frequency spectral ratio of the stronger and weaker event and f_{c1} and f_{c2} are their corner frequencies, respectively. The best fit between the observed data ratios and the model is solved as inverse problem by minimizing the differences in L_2 norm. In this analysis the residual function is optimized in the form

$$SR_{EGF} = \sum_{i=1}^{N*M} ||\Psi_i^{obs}(f) - \Psi_i^{mod}(f)||_{L_2} = \min \tag{2.33}$$

(similar to e.g. Kwiatek et al., 2011) where N is the number of event pairs and M is the number of stations. The analysis can be performed for

(a) one pair of events ($N = 1$) at M stations (i.e. I invert for one f_{c1} and one f_{c2} at all stations); or

(b) N event pairs and M stations simultaneously (i.e. I invert for one f_{c1} and N values of f_{c2} for each pair of events).

In addition, case (b) can be turned into (a) by creating one average EGF from more weak events of similar magnitude by stacking of their spectra (Shearer et al., 2006).

There are some numerical difficulties which have to be resolved carefully. First of the tasks is to estimate the amplitude of the spectra correctly; therefore the MTT approach of calculating spectra is used. Second problem can arise from the division by small numbers while evaluating the spectral ratio; namely the high-frequency oscillations can introduce spurious errors. This problem is eliminated by usage of optimum number of tapers ($NS = 7$) in the MTT approach which favorably flattens the high-frequency part of the spectra.[4] Another problem can arise from uneven sampling of the spectrum, i.e. the low-frequency part is sparsely sampled with respect to the high-frequency part and the model will emphasize the denser sampled part of the spectra. Resampling to a fixed number of values per decade (e.g. 12) is a possible solution. Practical implementation of the individual processing steps is given in section 3.5.

[4]The number of tapers is not tested here but this topic was properly discussed personally with G. Prieto and P. Moyer during the ECGS 2012 workshop in Luxembourg (Moyer et al., 2012).

Chapter 3

Source Parameters of the 2000 & 2008 Swarms

3.1 Introduction

The West Bohemia region is the most seismically active region in the Czech Republic and also belongs to one of the most active areas in the middle Europe. Occurrence of earthquakes in this intracontinental region is one of the relicts of the volcanic activity (Mrlina et al., 2009); last known eruptions are dated to 200 ka (Špičák & Horálek, 2001).

3.1.1 Observations from the West Bohemia/Vogtland

The earthquake swarms in West Bohemia/Vogtland pertain to the most striking manifestation of the present geodynamic activity of this intracontinental region (e.g. Horálek & Fischer, 2010). This area is situated in the western part of the Bohemian Massif at a contact of different Variscan tectonic units – the Saxothuringian, Moldanubian, and Teplá-Barrandian (Babuška & Plomerová, 2008). The ENE-WSW trending Eger Rift terminates close to the epicentral area and is intersected by the NNW- SSE striking Mariánské Lázně fault (Bankwitz et al., 2003). The geodynamic activity is manifested by emanations of CO_2 of mantle origin (Bräuer et al., 2011) and by Quaternary volcanism represented by Komorní hůrka, ťelezná hůrka and newly discovered maar structure of Mýtina (Mrlina et al., 2009). The frequently occurring weak earthquake swarms, mostly of magnitudes $M_L < 3.5$, concentrate in multiple focal zones in the depth range from 6 to 25 km (e.g. Horálek & Fischer, 2010). Among them, the area close to the village of Nový Kostel (close to station NKC in Fig. 3.1) dominates with more than 80 % of the released seismic energy. It was the place of all the recent major swarms in the years 1985/86, 1997, 2000, 2008 and 2011 (Fig. 3.1). The recorded seismic data were subject to various studies oriented to get insight into the generating mechanism of the earthquake swarms. The relative hypocenter locations in the area of Nový Kostel show a north-south steeply dipping fault plane of 8 km length in the depth range from 6 to 12 km whose orientation matches well with the source mechanisms (Fischer & Horálek, 2005). The detailed analysis of spatio-temporal distribution of hypocenters

shows that both the elastic stress transfer and high-pressurized fluids are responsible for the driving of the swarm activity (see e.g. Hainzl & Fischer, 2002; Hainzl & Ogata, 2005; Fischer & Horálek, 2005; Fischer & Michálek, 2008; Dahm et al., 2008; Hainzl et al., 2012; Horálek & Fischer, 2008). The source mechanism studies have shown that pure shear faulting prevails (Horálek & Šílený, 2013) compared to tensile faulting that occurs in the case of specific fault plane orientation (Horalek et al., 2002; Vavryčuk, 2002, 2011a).

So far, little attention was devoted to the studies of static source parameters of these earthquakes. First attempts to evaluate the source parameters of the West Bohemian earthquakes were presented by Antonini (1986); Grosser et al. (1986); Plešinger et al. (1986). All the studies are evaluating the standard set of source parameters as seismic moment, source size, static stress drop and average slip from the shear wave displacement spectra by applying the basic assumptions of Brune (1970) and Madariaga (1976) and some using the graphical methods of (Hanks & Thatcher, 1972). The analyses of events from the 1985/86 earthquake swarm are based on data from one (Grosser et al., 1986) to three stations (Antonini, 1986) and are limited to the strongest events only due to large epicentral distances (only 4 stations with digital recordings within the range of 30 km). Although large earthquake swarms occurred within the period 1997-2011, none of the works was aimed to determine the source parameters mentioned above.

The inversion for seismic moment tensors of the year 1997 swarm by Horalek et al. (2002) provided the first estimate of scalar seismic moments, which enabled establishing a scaling relation between the local magnitude and the scalar seismic moment (Hainzl & Fischer, 2002) in the form $\log M_0 = 1.05\ M_L + 11.3$. Fischer (2005) used the EGF method to study the source time functions of the year 2000 swarm events and found that many of them display a complex source time function composed of several pulses. Seismogram modeling revealed that some of these events correspond to a fast stick-slip rupturing composed of several rupture episodes separated in time and space. Analysis of stopping phases of selected 2000-swarm events by Kolar & Ruzek (2012) suggested the constant stress drop scaling of the source radius and seismic moment.

3.1.2 Observations around the world

The scaling between the seismic moment and size of the source with constant stress drop is commonly accepted as suggested by Aki (1967). Since then there are many studies aiming to find the confirmation of this law in the real data, namely for small earthquakes because their more frequent occurrence could help to understand the behavior of the big ones. The constant stress drop was observed e.g. by Abercrombie (1995) for earthquakes (M_L -1 to 5.5; $\Delta\sigma \sim 0.1 - 80$ MPa) in Cajon Pass borehole close to San Andreas Fault in southern California, by Prieto et al. (2004) who analyzed earthquakes (M_L 0.5 to 3.4) recorded by Anza seismic network in southern California, or by Yamada et al. (2007) who studied earthquakes (M_w 0.0 to 1.3; $\Delta\sigma \sim 3.2 - 88$ MPa) in South African gold mine. Also Viegas et al. (2010) reported high constant stress drop ($\Delta\sigma \sim 9.2 - 240$ MPa; median value 104 MPa) for the M5 intraplate earthquake, in 2002 and

its aftershocks in Au Sable Forks, NY and concluded that the apparent breakdown in source dimension scaling is caused by the limited bandwidth of the records. Allmann & Shearer (2007) estimated the source parameters of 42,367 earthquakes from period 1984-2005 in Parkfield, central California; their stress drop varied between 0.1 to 100 MPa with median value of 6.75 MPa also stating that the stress drop is nearly constant with seismic moment, implying self-similarity over the M_L 0.5 to 3.0 range. Similar results were obtained from analysis of about 60,000 earthquakes ($1.5 < M_L < 3.1$) in southern California (Shearer et al., 2006) with static stress drops between 0.2 and 20 MPa. Imanishi et al. (2004) used inversion method based on stopping phases to estimate source parameters of 25 microearthquakes ($1.3 < M < 2.7$) from the western Nagano prefecture, Japan. They found that the static stress drop ranged from 0.1 to 2 MPa only, do not vary with seismic moment and that the apparent breakdown in its scaling is an artifact of attenuation in the crust which mostly influenced the surface observations. They deduced that the earthquakes are similar over a wide range of magnitudes. Similar findings were reported by Kwiatek et al. (2011) in the study of picoseismicity ($-4.1 < M_w < -0.8$) from Mponeng Deep Gold Mine in South Africa ($\Delta\sigma \sim 0.01 - 1.0$ MPa). Oth et al. (2010) investigated the source characteristics of 1,826 events from accelerometric borehole recordings ($M_{JMA} = 2.7 - 8.0$) throughout Japan and confirmed the self-similar scaling with the median stress drop 1.1 MPa for crustal events. On the other hand Harrington & Brodsky (2009) observed pulses of constant width for a group of earthquakes on San Andreas fault (M 1.4 to 3.7), which could be explained as a reactivation of the fault patches of similar size with variable stress drop 0.18 - 68 MPa. Urbancic & Young (1993) analyzed 85 mining-induced events ($-2.2 < M_w < -0.3$) in Strathcona mine (Sudbury, Ontario) at depth 710 m. They obtained also relatively high static stress drops within the range 0.16 - 83 MPa and pointed out to possible non-similar behavior of the small and large events. Oye et al. (2005) analyzed approx. 1500 events ($-1.8 < M_w < 1.2$) from 1400m deep Pyhäsalmi ore mine in Finland. Their static stress drops range between 0.01 and 30 MPa and they noted that there are strong factors which contribute to significant deviations from the constant stress drop. Mayeda et al. (2005) used the coda waves to analyze 4 earthquake sequences (both natural and induced seismicity) in magnitude range $3.7 < M_w < 7.4$ to evaluate the scaling relations and their results strongly suggest the non-self-similarity. Edwards & Rietbrock (2009) studied attenuation and scaling relations of two magnitude-different datasets ($2.0 < M_{JMA} < 4.0$; $3.0 < M_{JMA} < 7.2$) and concluded that the stress drop must increase with M_w; or that increase of the stress drop for the smaller earthquakes is an artifact of the site effect. All the studies report quite wide ranges of the stress drop which were by some authors interpreted as constant at specific sites/regions (valid source scaling relations) and as non-constant elsewhere (break in source scaling) by others. The comparison of the results of these studies is complicated because of different quality of the processed datasets and the methods used. I do not want to emphasize the differences in absolute values of the stress drop in the studies because these are model dependent. But the trends in individual studies differ and source scaling dependence can

be influenced by application of some particular method. Most of the studies addressed above emphasize the importance of the attenuation correction and its strong influence to the results, which can lead to under/overestimation of the source parameters, primarily the corner frequency (e.g. Imanishi et al., 2004) and the other parameters consequently. The specific implementation of the attenuation corrections varies in individual studies and knowing the high tradeoff level between the source parameters and attenuation brings many degrees of freedom to the problem. The relative EGF method should remove the attenuation effects and ambiguity of the source parameters but another uncertainties can arise from the EGF approach and these are discussed in section 3.5.

3.1.3 Aims

In my thesis I aim to examine the scaling between the seismic moment and the source size for the earthquake swarm events in the West Bohemia region, in particular the range of the stress drop and possible anomalies in scaling for the small magnitude events. I present estimates of the static source parameters - source dimension and stress drop of the West-Bohemia swarm earthquakes. I use the absolute approach in frequency domain (similar to that of e.g. Lindley & Archuleta, 1992; Abercrombie, 1995; García-García et al., 1996; Abercrombie & Rice, 2005; Dobrynina, 2009; Kwiatek et al., 2011) and also the relative approach using the EGF methods (Hartzell, 1978, or recently e.g. Shearer et al., 2006; Baltay et al., 2010; Viegas et al., 2010; Kwiatek et al., 2011). I employ the high-quality seismic data recorded by the WEBNET seismic network (Fischer et al., 2010) to bring new insights into understanding of the source processes in this unique area of intracontinental seismicity. A special attention is paid to uncertainties of the source parameters.

The absolute methods were applied to 56 swarm-events from the West Bohemia region in years 2000 and 2008. The first results of the absolute approach applied to the P waves were published in Michálek & Fischer (2013). In this thesis the results were examined in more details extending the error analysis and broadened in terms of new methods and by additional analysis of S waves.

The relative methods were applied to a small group of six events from the 2008-earthquake-swarm. The selection of these events was based on results from the previous cluster analysis (Fischer & Michálek, 2008) where the similarity of the P-wave seismograms was tested by the cross-correlation analysis. The aim of application of the relative methods was not to process a large number of events but to test the stability of the methods and their uncertainties.

Finally, I compared the results from absolute and relative approaches as well as with results of similar studies around the world.

3.2 Data

The seismicity in the West Bohemia (WB) region is monitored for more than two decades by the seismic network WEBNET; for description see, e.g. Fischer et al. (2010). In the

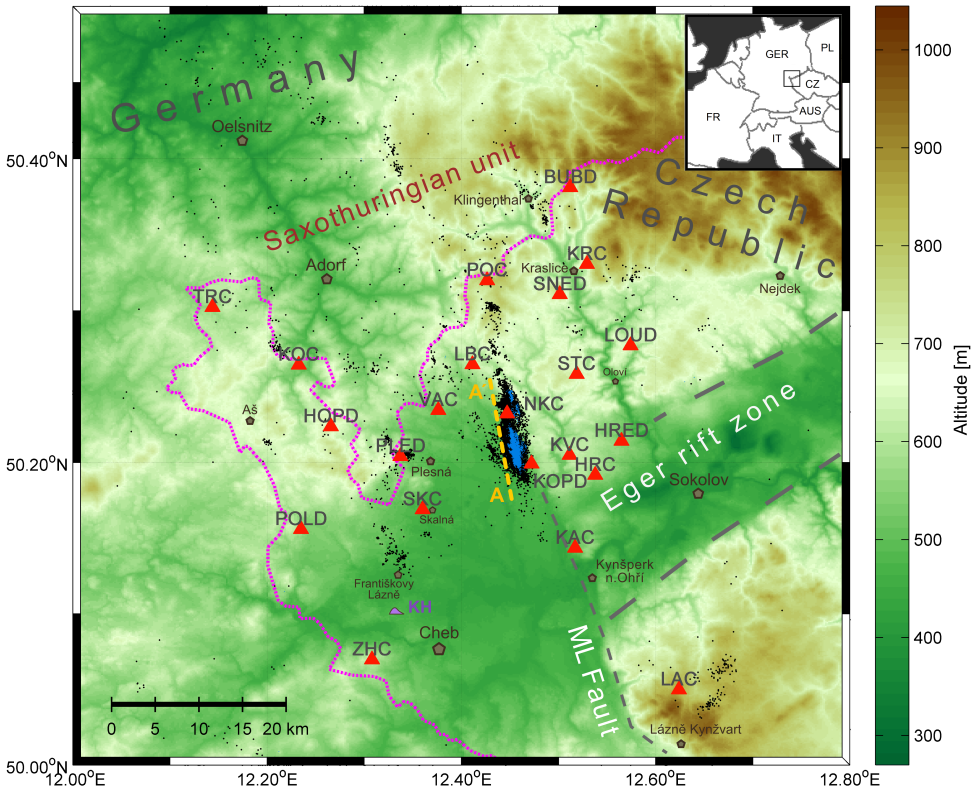

Figure 3.1: Map of WEBNET network and epicenters from 1991 to 2010 (black dots) in the West Bohemia/Vogtland region. The earthquake swarms 2000 and 2008 are highlighted in blue color. The red triangles are WEBNET stations. The depression to the south from the NKC station is the tertiary Cheb basin; its eastern edge is terminated by the intersection with the Eger rift. (topography based on USGS, 2002)

WB region the hypocentral distances R range between 6 to 30 km and the observed wavelengths of P waves are up to 3 km (assuming $v_\alpha = 6$ km/s; $T = 0.5$ s). Fault size L of the local M4.0 earthquake can be up to 0.5 km. From this and (2.15) I get that L^2 =0.25 and $1/2\lambda R = 9$ [km^2]. The L^2 is at least 36 times lower than the the right side of (2.15), which should be sufficient enough to use the far-field approximation.

I processed events ($0.8 \leq M_L \leq 3.3$) from the West Bohemia region (Fig. 3.1), which occurred during the earthquake swarms from August to December in 2000 and in October 2008. Selected events are located on a steeply dipping fault plane (strike 169°, dip 80°) in the depth range 7.5-10 km (Fig. 3.2). The number of stations used for spectral analysis differs for individual events. The configuration of stations in 2000 (12 stations) was less favorable than in 2008 (22 stations) in terms of the coverage of the focal sphere. In 2000 seven stations at maximum (usually 3-4 stations) were found suitable for the analysis because of the azimuthal position with respect to the hypocenters (Fig. 3.1). In 2008 I could use up to 21 stations (usually 12-15). The criteria for selecting events and stations for the inversion were the signal-to-noise ratio > 3 (i.e. ~ 10 dB) in

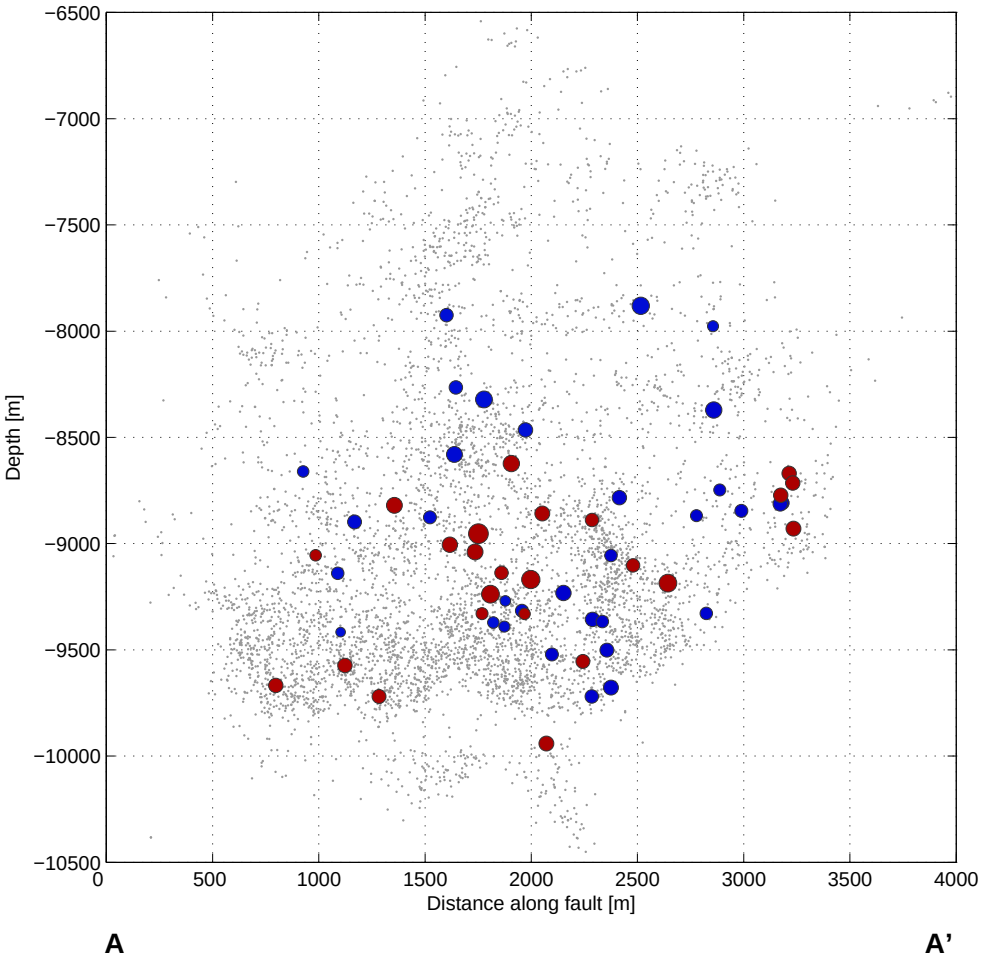

Figure 3.2: Distribution of hypocenters in the 2000 (blue) and 2008 (red) swarms along the fault plane (viewing from ENE to WSW). Size of the circles corresponds to the seismic moment. Hypocenters located by hypoDD location program (Waldhauser & Ellsworth, 2000) in 1D inhomogeneous velocity model (Málek et al., 2000). Locations provided by Hana Čermáková.

the analyzed frequency band of 1-100 Hz. Because of collocation of the events in these two periods I analyzed them together with emphasis on the 2008 swarm. Only events with clear and simple P pulse were selected to eliminate multiple or complicated rupture processes. Accordingly I eliminated the multiple events identified by Fischer (2005). These criteria allowed me to process events down to $M_L = 0.8$. The most limiting criterion was the signal-to-noise ratio, which did not allow to reliably process smaller earthquakes at distant stations. I analyzed P waves recorded on vertical components of short period seismographs SM-3 and LE-3D sampled by 250 sps. The frequency band was limited by the corner frequency of the velocigraphs (0.5 Hz for SM-3 and 1 Hz for LE-3D) and by the sharp anti-alias filter in the recording unit at 80 Hz and 100 Hz for the 2000 swarm and 2008 swarm, respectively. Data were transformed to displacement and no filtration was applied.

3.3 Application of the absolute methods to P waves

3.3.1 Processing

Application of the spectral analysis was initially performed for the P waves because of their clear onset and uncontaminated seismogram by the other wave phases.

In our case, I could neglect the instrument response function $I(f)$ because all the earthquake corner frequencies were at least six times higher than the corner frequency of the instruments – the lower corner frequency limit of the sensors is 1 Hz and the expected/obtained corner frequencies of the events starts at 6.5 Hz (for details see section 2.3.1). Therefore the records were corrected for sensitivities only and the analysis was always carried out in the interval of flat response of the instrument. Hence for retrieving the amplitude source spectrum $\Omega(f)$ two effects must be corrected for:

1. frequency dependent anelastic attenuation (amplitude decrease with distance and broadening of the pulse in the time domain)

2. frequency independent geometrical spreading (amplitude decrease with distance)

The first effect is solved during the inversion process itself while searching for the true earthquake corner frequency over the multiple stations. The second, geometrical spreading effect plays an important role when evaluating the seismic moment from the low frequency amplitude plateau Ω_0 using equation (2.14).

3.3.2 Spectra estimation

A time window of 1 sec duration was used to calculate the spectrum. It contains 0.5 sec of noise and the remaining part includes the signal of the P wave with almost 100 % of its energy. The noise spectrum was calculated from the first half of the time window and replicated while the signal spectrum was calculated from the whole window using the MTT. Spectrum was interpolated in order to obtain equidistant frequency spacing in the logarithmic scale (12 points per decade). I did not apply any smoothing operator

because the MTT smooth the spectrum itself. The resulting displacement spectra were compared to the model (2.30).

3.3.3 Inversion of individual events

The source model represented by (2.30) was parametrized by two free parameters f_c and Q. The model was fitted to the data by searching for the minimum of the residual function in L2 norm (3.1). As an optimization algorithm I used the *Nelder-Mead simplex method* which is implemented in the *fminsearch* MATLAB function. The value of Ω_0 was determined as a mean value from three spectral amplitude values of $\Omega(f)$ at the lowest frequencies between 1-3 Hz, where the spectrum is always flat even for the strongest M3.5 events. The fit was realized in the frequency range 1-100 Hz (or 1-80 Hz for the PCM system; operated at stations KOC and LAC during the 2008 swarm). Because the differences of spectral amplitudes at low and high frequencies are up to two orders I used the logarithm of the values for the model and data and the residual function was defined as

$$SR = \sum_{i=1}^{N} || \log \Omega_{model}(f_i) - \log \Omega_{data}(f_i) ||_{L_2} \tag{3.1}$$

where N is the number of discrete frequencies at which I compare the model and data. The simplex method always converged to the minimum of the residual function when the initial values of fitted parameters were in reasonable intervals. For f_c the initial value should be in the range of the observed data, i.e. 1-100 Hz and for Q the initial value of 200 was used (Stein & Wysession, 2003), because all the stations are surface stations built on a hard rock (crystalline or metamorphic units). Different initial values of fitted parameters did not affect the final solution. To stabilize the inversion I made an assumption of a common f_c for all stations for the analyzed event which can be valid in the first approximation of the source only. The assumption of a common f_c can be used only if one does not expect any directivity effects of the source. The residual function in such case is modified to

$$SR_{all} = \frac{1}{N} \sum_{i=1}^{N} SR_i \tag{3.2}$$

where N is the number of stations where the event was analyzed. Figure 3.3 shows the inversion results at station BUBD as an example for two events of M_L3.1 and M_L1.7.

By minimizing the logarithmic sum of residuals between the model (2.30) and data in L2 norm (3.1) I obtained the single corner frequency f_c for each earthquake and N values of attenuation factors Q (for N stations). In this way multiple Q-factors were retrieved for each station for different events; their variation may account for example for the neglected source directivity and other source-dependent effects.

Using multiple stations for determining f_c led to stabilizing the process of obtaining the corner frequency compared to determining f_c from single-station data, which is also tested before each common inversion process. Stations HRC and SKC with strange pulse shape and $f_c > 50$ Hz obtained from the individual inversion were excluded from

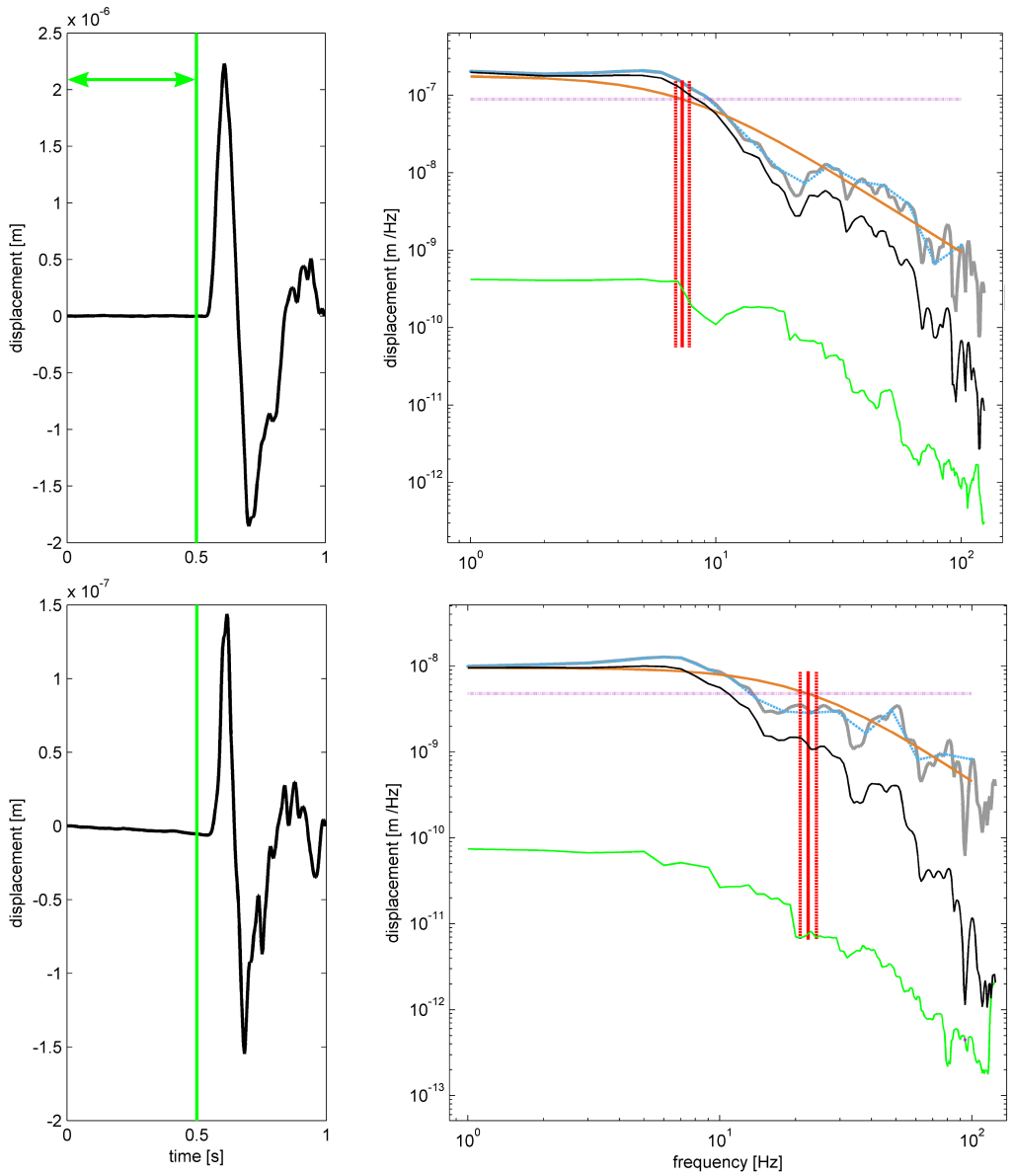

Figure 3.3: Ground displacement of the P pulse (left) with noise window marked by green arrow. Example of the spectral analysis (right) of event with a) M_L3.1 (ID: X2411A) and b) M_L1.7 (ID: X402A) at station BUBD. Black line is the observed spectrum, green line is the noise spectrum, both not corrected for Q. Observed spectrum (gray), interpolated observed spectrum (blue) and model spectrum (orange) are all corrected for $Q = 277$. The pink horizontal line is the half value of Ω_0 (intersection with spectrum line is at f_c for Brune's model). f_c (vertical red line) and its uncertainty estimates (dashed red line) were obtained by a single-station inversion of the corrected spectrum.

the common inversion to eliminate unrealistic results. I also excluded distant station ZHC because of the low signal-to-noise ratio. I evaluated the uncertainty of f_c by testing the shape of the residual function SR, i.e. the flatness of the function around its minimum value. Lower and upper error bounds of f_c were determined at frequencies corresponding to the 5 % increase above the minimum of the SR (Viegas et al., 2010). These error bounds are not errors in terms of the standard deviation but more like an indicator of uncertainty of the result.

I attributed all the deviations of the high-frequency spectral falloff from the ω^{-2} model to the effect of anelastic attenuation and because the site corrections are not known for our stations the all attenuation is gathered in the Q-factor.

Figure 3.4 illustrates how the inversion was performed and how the parameters evolve near the optimal solution. After obtaining the optimal solution (f_c, Q_i; $i \in (1; N)$ stations) I tested the tradeoff between f_c and Q (right column in Fig. 3.4). For this purpose I run repeatedly the inversion for several fixed f_c in the vicinity of its optimal solution to search for the corresponding Q at individual stations. The resulting dependence of Q-factors on the selected f_c shows that Q is almost constant at most of the stations (except for stations NKC and PLED; in this example). This shows that the optimal f_c is robust with respect to the applied correction for attenuation.

To verify the significance of the possible tradeoff between fitted parameters f_c and Q I performed a jackknife test by omitting individual stations from the inversion (Fig. 3.5). The results in Fig. 3.5a show that variations of f_c for individual realizations stay within the range of the standard deviation of the solution found from all stations and omitting the problematic individual station does not decrease significantly the SR. To test the sensitivity of Q at individual stations to omission of other stations from the inversion I plot in Fig. 3.5b the mean values of Q from all jackknife realizations. I found that all, except for three stations, were performing well showing stable Q, independently on inclusion of other stations into inversion. However, despite the three unstable stations, the resulting corner frequency remains stable within the standard deviation found from all stations (Fig. 3.5a). Note that the variation of f_c is within 7 % of the mean value found from all stations.

3.3.4 Joint inversion

For events from the 2008 swarm I performed a joint inversion of corner frequency f_c and quality factor Q over multiple events and all suitable stations. The source model was assumed to be the same as in previous section, i.e. the same f_c over all stations for each particular event. Second constraint was related to the quality factor Q, i.e. the Q was the same for each particular station. This constraint I could use because of similar ray paths from the closely collocated events. The residual function is then defined as

$$SR_{joint} = \sum_{i=1}^{N*M} ||\log \Omega_{model}(f_i) - \log \Omega_{data}(f_i)||_{L_1} = \min \tag{3.3}$$

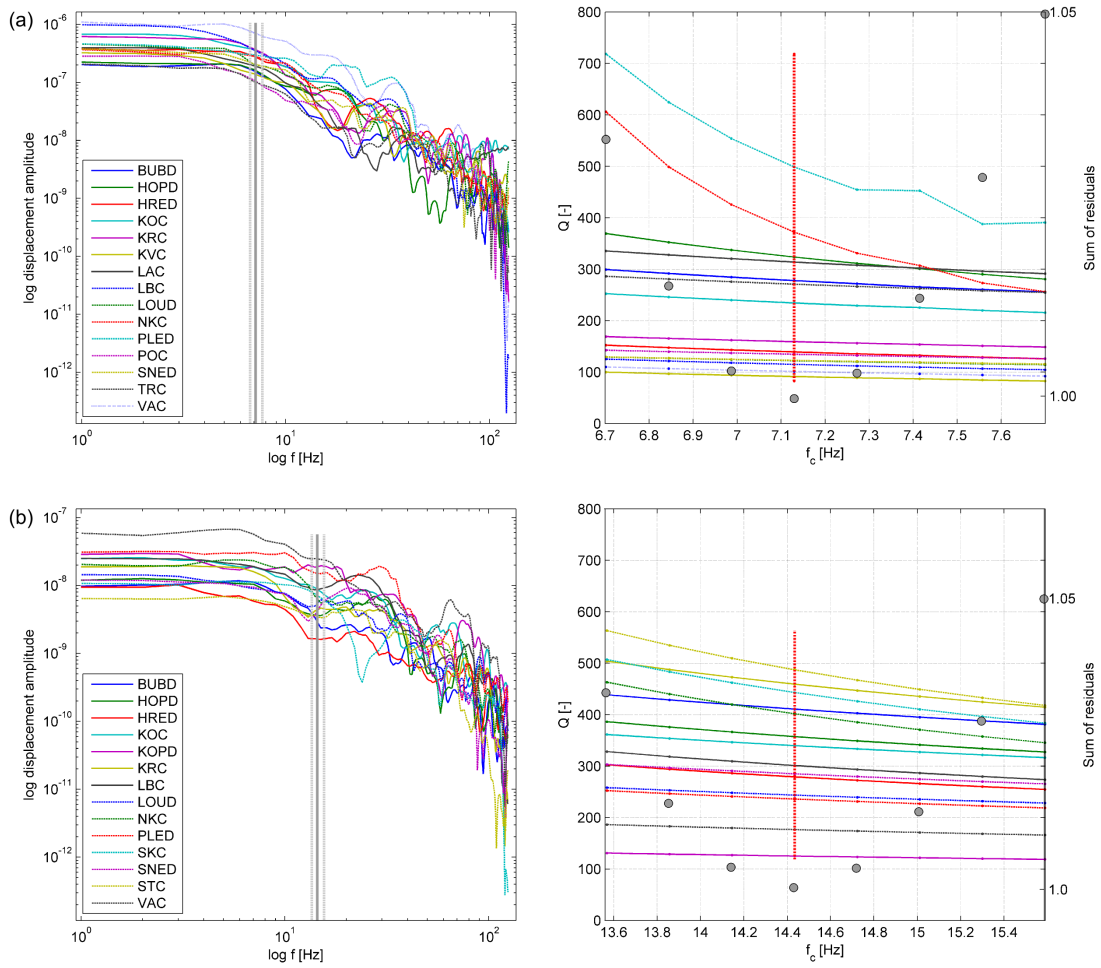

Figure 3.4: Example of inversion for single f_c and station-dependent Q for $M_L = 3.1$ (a) and $M_L = 1.7$ (b) events from Fig. 3. Spectra (left) are corrected for attenuation with Q corresponding to $f_c = 7.13$ and $f_c = 14.42$, respectively. (right) Testing of stability of Q for changing f_c in the range of ± 20 per cent around the minimum of the misfit function (gray circles). The f_c axis limits corresponds to the 5 per cent increase of the misfit function. These limits are plotted in left plots as dashed vertical lines. The legend on the left relates to both plots.

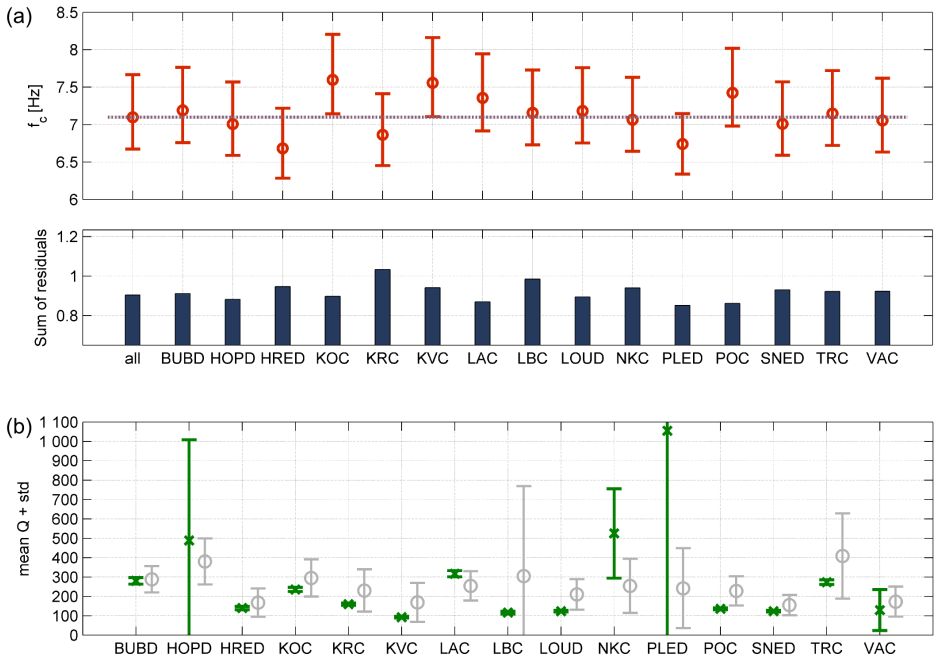

Figure 3.5: (a) Test of stability of the fitted parameter f_c in the inversion using the jackknife test with omitting individual stations for event $M_L = 3.1$ (ID: X2411A). The first column named *all* is result of inversion including all suitable stations. Mean value of this f_c is marked by dashed horizontal purple line. The label on the horizontal axis denotes results while omitting the particular station. (b) The mean values of Q at stations over all realizations of jackknife test (green). The corresponding values of Q resulting from using all events in this study are shown in gray.

where N is the number of stations and M is the number of events; I searched for N unknown Q and M unknown f_c. The low-frequency spectral level was fixed to the same values as in the previous absolute approach and therefore the seismic moment M_0 was not affected the inversion.

3.3.5 Results

Radiation pattern correction

Seismic moment at individual stations was obtained from (2.14) where $\rho = 2700$ kg/m^3, $\alpha = \sqrt{3}\beta = \sqrt{3}\,3500 \doteq 6062$ m/s and F_{surf} is assumed constant and equal to 2 because of the subvertical incidence of the P waves (Horalek et al., 2002). The seismic moment for each event is calculated as a mean of the logarithmic values from available stations.

The individual RP corrections $\Re_\alpha$ applied to the 2000-swarm events were calculated for the typical fault plane orientation (strike = 169°, dip = 80°, rake = -30°), which is almost the same for all events (Fischer & Horálek, 2005). For events from the 2008-swarm I was able to apply the individual RP corrections $\Re_\alpha$ obtained from focal mechanisms of individual events. The comparison of application of the individual RP corrections $\Re_\alpha$ and the average RP corrections $\langle\Re_\alpha\rangle = 0.52$ is shown in Fig. 3.6. The effectivity of the individual RP corrections can be viewed as vertical redistribution of the gray dots along the green values of M_0. If application of the individual RP corrections was successful the dots should gather along the mean M_0 value and should be less scattered in the vertical direction than before application of the RP correction $\Re_\alpha$ (dots along the red values of M_0). Proximity of the mean and median values of M_0 is a similar indication of the successful RP correction. The scatter of M_0 over all stations is often around one order and the individual RP correction $\Re_\alpha$ does not improve the scatter significantly.

Therefore I analyzed contribution of the RP corrections to M_0. From equation (2.14) the RP correction $\Re_\alpha \in < -1; 1 >$ is applied in the denominator. Values of $\Re_\alpha$ close to zero are at stations which are close to nodal lines on the focal hemisphere (Fig. 3.7). Application of $\Re_\alpha$ at these stations introduces division by small number and will cause higher scatter of M_0 with respect to the mean M_0 obtained by including the average RP correction $\langle\Re_\alpha\rangle$. Thus I aimed to find the minimal $\Re_\alpha$ above which the resulting M_0 will show lower scatter than with $\langle\Re_\alpha\rangle$. For each event I sorted the stations with respect to the absolute value of $\Re_\alpha$ in ascending order and successively omitted stations with the lowest $\Re_\alpha$. For each such set of stations I calculated the standard deviation of the individually corrected seismic moment $\sigma(M_0^{RP})$. As expected, $\sigma(M_0^{RP})$ is decreasing with omitting stations having low $\Re_\alpha$. Figure 3.8 shows ratio of $\sigma(M_0^{RP})$ and $\sigma(M_0)$, where M_0 is obtained by involving the average correction$\langle\Re_\alpha\rangle$. Values of RP$_{min}$ where the ratio is lower than 1.0 could be considered as suitable values of $\Re_\alpha$ to be applied individually. For some events inclusion of stations with even low values of $\Re_\alpha = 0.2$ leads to decrease of the ratio, but in average, looking at the thick black line, the improvement of M_0 due to individual RP corrections is for stations with $\Re_\alpha > 0.45$, where the line is below value 1. It is worth noting that limitation to stations with relatively high $\Re_\alpha$ values leads to decrease the number of stations and therefore M_0 is worse conditioned.

It follows from this analysis that inclusion of individual RP correction, included simply as in (2.14), even for relatively precise focal mechanism and good focal sphere coverage by stations, can lead to biased results. In the light of this finding it is probably better to include the average RP correction only.

Free surface correction

The free surface correction F_{surf} in (2.14) is assumed constant and equal to 2.0 throughout the study. This assumption is confirmed by analysis of the 2008 swarm events using the AMT method Vavryčuk (2011b) implemented in SEISMON which uses the raytracing approach for evaluation of the reflection and transmission coefficients in the used velocity model and also including the RP correction coefficient and the free surface correction. From AMT the F_{surf} is ranging between 1.9 and 2.0 over all stations and events with the mean value of 1.94 and standard deviation 0.023. Hence, simplification of the free surface correction F_{surf} to value 2.0 will not distort the results of M_0 by more than 5 %.

AMT approach

The AMT method (Vavryčuk, 2011b) is primarily designed to use the maximum of the P-wave amplitudes as an input which allows to obtain the relative moment tensor and the focal mechanism consequently. If I use Ω_0 together with an information of the P-wave polarity onset as an input, I will obtain directly the absolute moment tensor and by application of the norm (2.12) also the scalar seismic moment M_0. The AMT method calculates rays and reflection and transmission coefficients according to the 1D inhomogeneous velocity model (Málek et al., 2000). Therefore results from this method should be the most accurate with respect to the raypath applicable corrections. Figure 3.9a shows comparison of M_0 from the AMT approach and from absolute approach, including the average or individual RP corrections. Despite the results from both absolute approaches show distinct scatter from the 1:1 reference line, the differences of the logarithms (Fig. 3.9b), which are comparable to magnitudes, are still within the 0.3 level, which is the uncertainty level of the local magnitude in WB and therefore I can say that the seismic moments are similar from all the approaches. Inclusion of individual RP corrections shows slightly higher differences, which again shows that inappropriate RP correction can bias the results. The AMT method gives good results if sufficient focal sphere coverage by stations is available. For this reason the AMT method could be applied only to events from the 2008 earthquake swarm where enough stations were deployed. Therefore the values of the absolute seismic moments with the average RP correction were used in the following analysis, because these values are available also for the 2000 earthquake swarm (this is different to the results presented in Michálek & Fischer, 2013). Numerical values of M_0 are in Tab. 3.1.

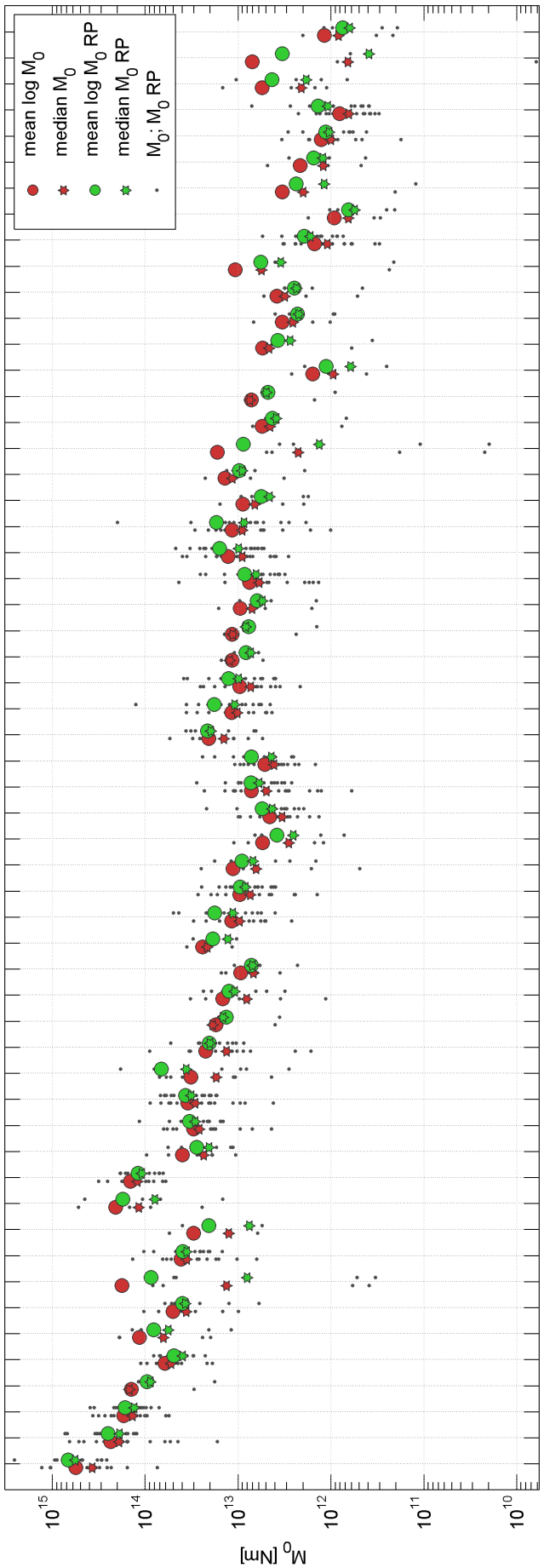

Figure 3.6: Comparison of M_0 obtained by different ways. The red symbols represents values of M_0 with an average RP correction and the green symbols including the individual RP corrections. For the events from the year 2000 (names starting with P) the same typical focal mechanism was used for RP correction in the individual RP approach. The gray dots represents seismic moment observed at individual stations.

Event ID	$M_0^{abs\,indivRP}$	$M_0^{abs\,avgRP}$	M_0^{AMT}	RMS^{AMT}	$nSta$
X1153A	2.37e12	1.98e12	2.92e12	0.325	14
X1240A	1.76e12	1.69e12	1.70e12	0.318	11
X1266A	1.19e13	7.04e12	9.73e12	0.238	15
X1462A	1.51e12	1.21e12	1.31e12	0.576	16
X1466A	7.12e14	4.04e14	6.27e14	0.286	15
X1590C	1.93e14	1.31e14	1.85e14	0.244	11
X1590D	5.82e14	2.92e14	3.54e14	0.278	21
X1732A	1.78e13	8.57e12	1.08e13	0.324	18
X1893A	3.91e13	2.31e13	3.04e13	0.202	16
X1992A	2.36e13	8.90e12	1.50e13	0.554	16
X2002A	9.90e13	8.89e13	1.67e14	0.206	9
X2136A	8.07e13	4.66e13	6.59e13	0.245	18
X2144A	1.01e14	5.70e13	4.69e13	0.907	15
X2263A	1.65e13	7.77e12	9.26e12	0.622	14
X2411A	3.61e14	2.75e14	2.75e14	0.547	14
X2678A	3.17e13	2.34e13	4.05e13	0.584	10
X3143A	1.78e13	1.63e13	3.08e13	0.173	9
X3148A	1.24e13	1.02e13	1.01e13	0.712	18
X3169A	2.34e13	1.81e13	1.99e13	0.696	18
X3730A	5.04e13	2.56e13	2.08e13	0.821	14
X402A	1.13e13	7.99e12	1.09e13	0.197	16
X6694A	1.87e13	1.64e13	1.96e13	0.289	12
X840A	1.08e13	8.17e12	9.47e12	0.350	18
X874A	2.45e13	1.24e13	1.52e13	0.352	16

Table 3.1: Comparison of seismic moments from the absolute approach and from the AMT approach (units of Nm). In the column $M_0^{abs\,indivRP}$ the individual RP corrections were included whereas in column $M_0^{abs\,avgRP}$ the average RP corrections were used. The column M_0^{AMT} and the following are related to results from the AMT approach.

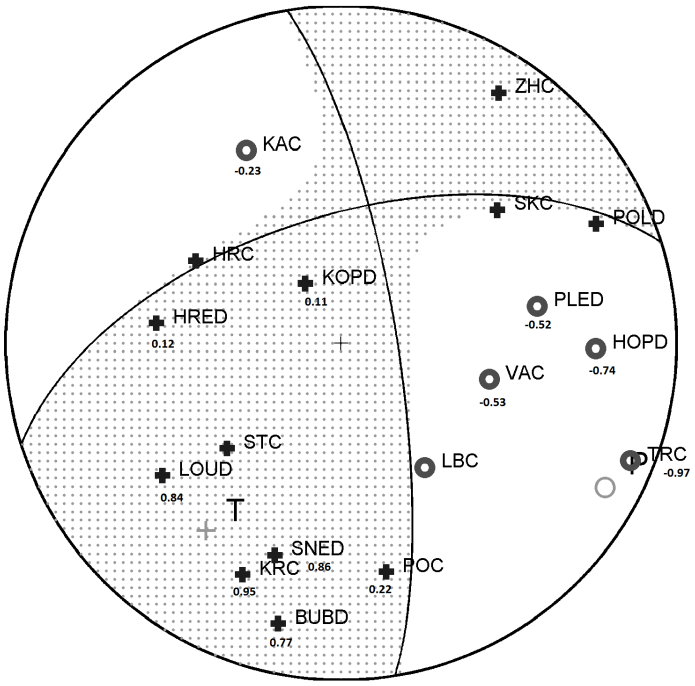

Figure 3.7: Focal mechanism for event X6694A (M_L1.9) from 2008 swarm with stations plotted on the lower hemisphere with denoted values of $\Re_\alpha$ below each station code (only at stations used for spectral analysis). Orientation of the fault plane: strike = 171°, dip = 77°, rake = -32°.

Effects of source mechanisms and directivity to M_0 and Q

In this study I neglected the effects of directivity of the source by using the model of a point source. To test whether this simplification is justified I selected two different focal mechanisms from the 2008 swarm dataset (FM1 and FM3 following Vavryčuk et al., 2013), each including up to 8 events. The directivity effect would be manifested by change of Q at stations, which are close to nodal lines for one FM type and farther away for another FM type. The result of this test is illustrated in Fig. 3.10. The mean Q factors range between 100 - 450 and are quite stable for both groups of events with standard deviation usually around 50. Besides, the Q factors obtained from the two event groups are quite similar. If one omits the stations with small number of events (less than 5) only HOPD and TRC show remarkable difference in Q-factors for the FM1 and FM3 groups. However, these two stations show almost the same position on the focal sphere for both FM types, which suggests that the possible directivity does not influence the station Q-factors and indirectly also the corner frequency. This simple test shows that for the purpose of inversion for f_c the directivity effects can be included in the event dependent attenuation. Group FM1 includes stronger events than FM3 (Fig. 3.10c) and therefore the FM1 events were registered at more stations.

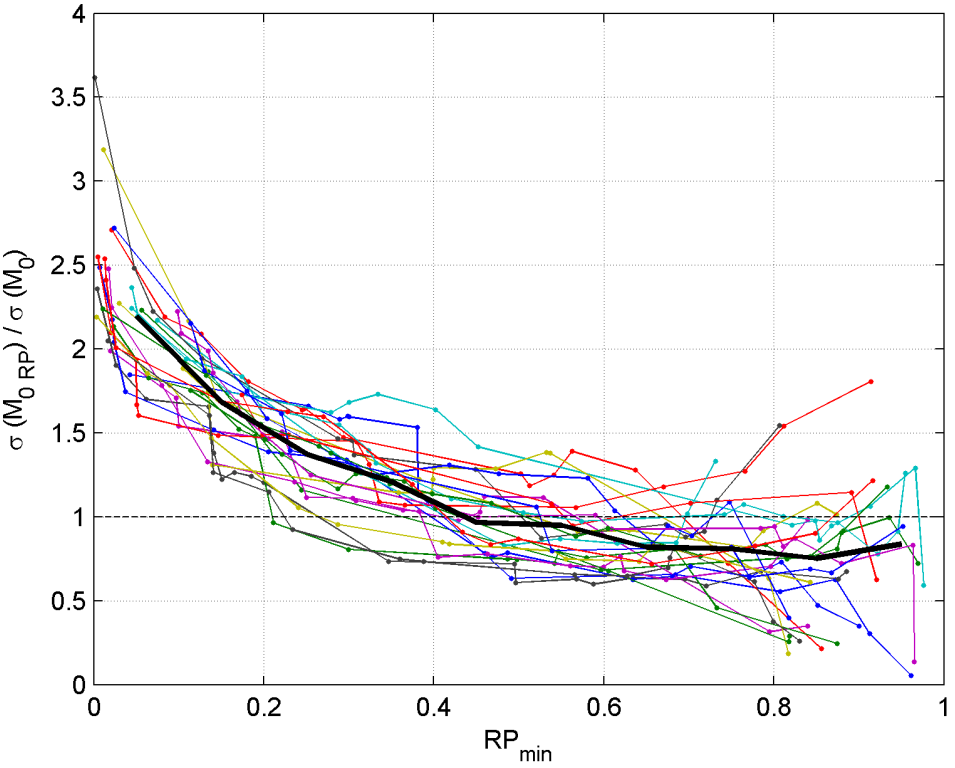

Figure 3.8: Effect of RP correction on seismic moment M_0 evaluated for individual events. Each colored line stands for one event. Each following point on the curve is calculated for stations with omition of the previous lower RP correction coefficient. The thick black line is an average value of the standard deviation ratio calculated in bins wide 0.1 of RP correction coefficient and plotted in the middle of each bin.

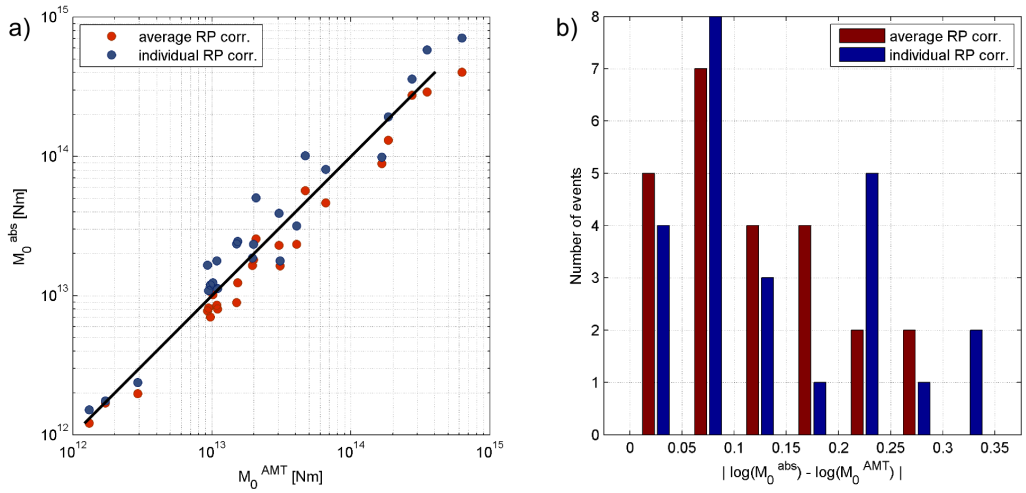

Figure 3.9: (a) Comparison of seismic moments from the absolute approach and from the AMT approach. The black line is 1:1 scale. (b) Histogram of differences in log scale between the absolute and AMT approach.

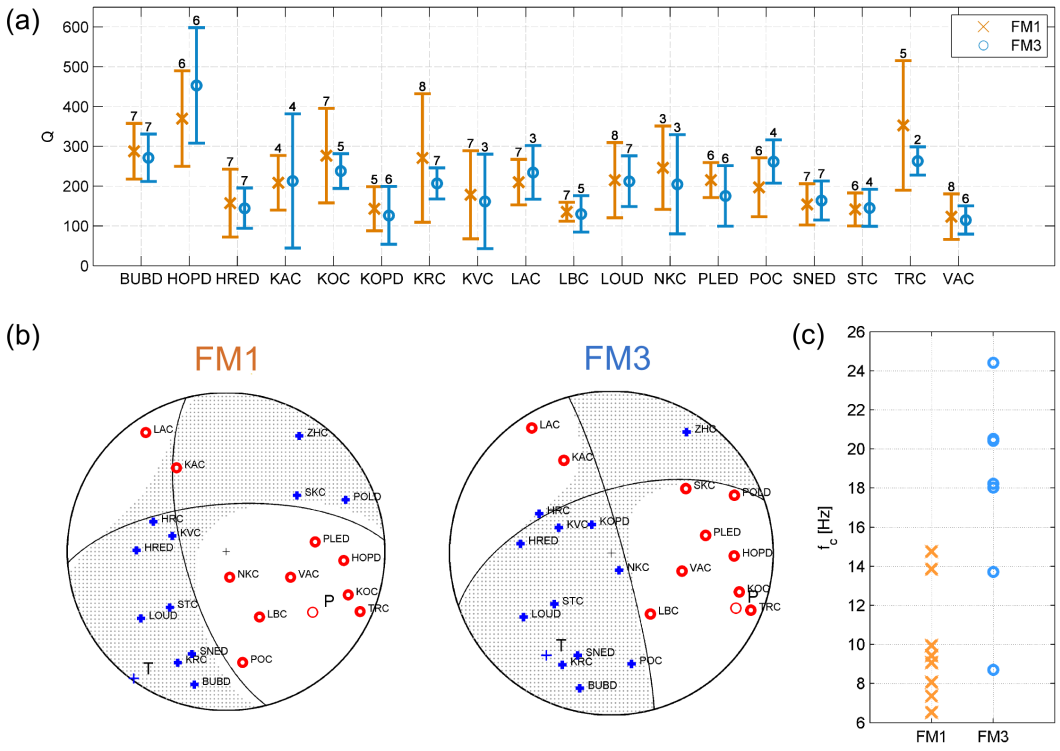

Figure 3.10: (a) Mean values and standard deviations of quality factors Q obtained for (b) two groups of focal mechanisms FM1 and FM3 (notation as in Vavryčuk et al., 2013), representative focal mechanisms are plotted for each group. The number above the upper standard deviation limit in (a) is number of events from which the mean is calculated. (c) Corner frequencies of events in each FM group.

Corner frequency and source dimension

As a solution of the inversion I obtained for each event the corner frequency f_c and N values of Q (having the set of N stations for each event). Applying (2.7) to the corner frequency f_c I got an approximate source radius. By application of the same relation to the error bounds of f_c I obtained also some rough estimate of the error of the rupture radius r. Overview of scaling of the rupture radius r with seismic moment M_0 is in Fig. 3.11. The resulting dependence of r on M_0 is approximated by

$$r = 0.167\, M_0^{0.202} \tag{3.4}$$

with the correlation coefficient 0.78. The rupture radii range from 2 to 170 m and the static stress drops between about 1 MPa and 130 MPa. The error bars in Fig. 3.11 are for the rupture radii and are calculated from the uncertainty $err\, f_c$ (in Tab. 3.2). These error estimates are most probably underestimated but at least provide the same relative measure of uncertainty for all events. A rather weak scaling of the source radius with seismic moment in the form $M_0^{0.20}$ is obtained, which points to the deviation from the constant stress-drop model that would correspond to the scaling in the form $M_0^{1/3}$. This is also expressed by the increase of stress drop with seismic moment (Fig. 3.12). The stress drop was evaluated using (2.17), firstly by substituting f_c^{inv} from inversion and secondly by substituting $f_c$obtained from J using (2.22). The regressions in Fig. 3.12 have form

$$\Delta\sigma(f_c^{inv}) = 4.63 M_0^{0.495} \tag{3.5}$$

$$\Delta\sigma(J) = 1.51 M_0^{0.543} \tag{3.6}$$

where the cross-correlation coefficients are 0.70 and 0.74, respectively. The aim of equations (3.5) and (3.6) is not to find the relation between $\Delta\sigma$ and M_0 but to show the similar trends for $\Delta\sigma(f_c^{inv})$ and $\Delta\sigma(J)$. The approximate relation in the form $\Delta\sigma \propto M_0^{0.50}$ indicates that events differing by two orders of seismic moment differ by one order in their stress drop. As shown in Fig. 3.13 the distribution of stress drops along the fault plane shows the highest stress drops in the central part of the fault patch which could be related to asperities.

Assuming the constant stress-drop model, the slip $\bar{D}$ along the fault plane should scale to the source radius as $M_0^{1/3}$, which is found by comparing equation (2.17) and the definition of the seismic moment (2.9). The weak increase of the source radius r with M_0 found in the data should be thus compensated by a stronger scaling of slip $\bar{D}$ with M_0. This is documented in Fig. 3.14 where the slip $\bar{D}$ is calculated from the seismic moment and the source radius. Linear regression in the logarithmic scale gives (assuming a constant rigidity $\mu = \rho\beta^2 = 33.1$ GPa) relation

$$\log \bar{D} = 0.596 \log M_0 - 9.462 \tag{3.7}$$

which shows scaling $\bar{D} \propto M_0^{0.596}$ with much higher exponent than 0.33 expected for a

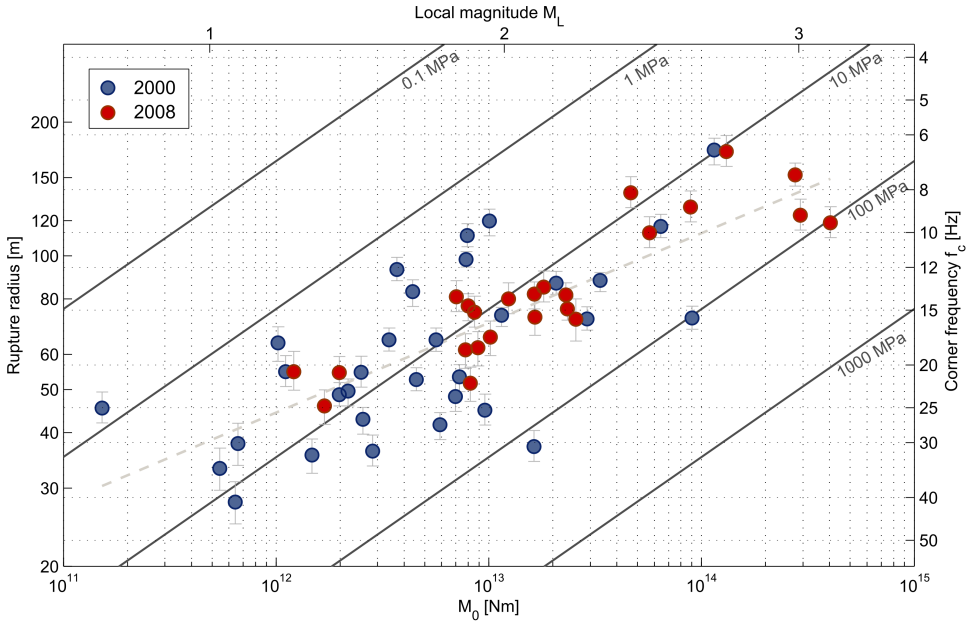

Figure 3.11: Dependence of the corner frequencies (right axis) and the rupture radii (left axis) on seismic moment obtained by spectra inversion method. The error bars are for rupture radii and are derived from the 5 % uncertainty of the f_c (flatness of the residual function). Blue circles are events from the 2000 swarm and red circles events from the 2008 swarm. The gray dashed line is regression between r and M_0 for all the events together. The upper magnitude axis is scaled according to relation found from regression of M_L and M_0 (Eq. (4.1)).

constant stress drop model. The resulting seismic slip ranges from 1 mm to 30 cm for seismic moments between 1.5e11 and 4e14 Nm.

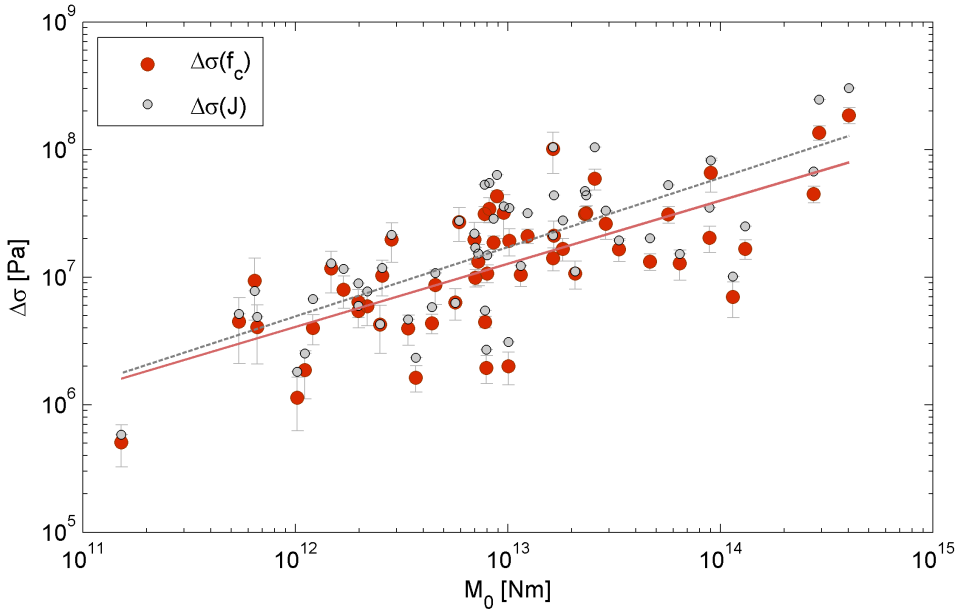

Figure 3.12: The dependence of the stress drop on the seismic moment.

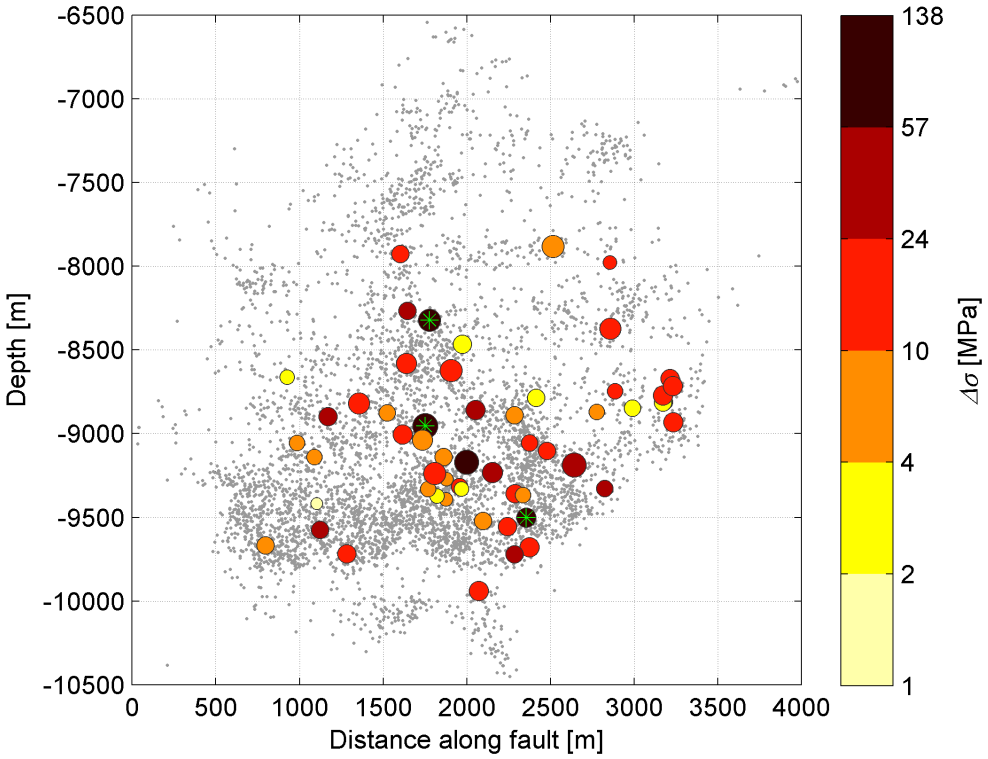

Figure 3.13: Distribution of stress drop along the fault plane. Events with stress drop higher than 100 MPa are highlighted by green star. Size of the circles corresponds to seismic moment (similar to Fig. 3.2).

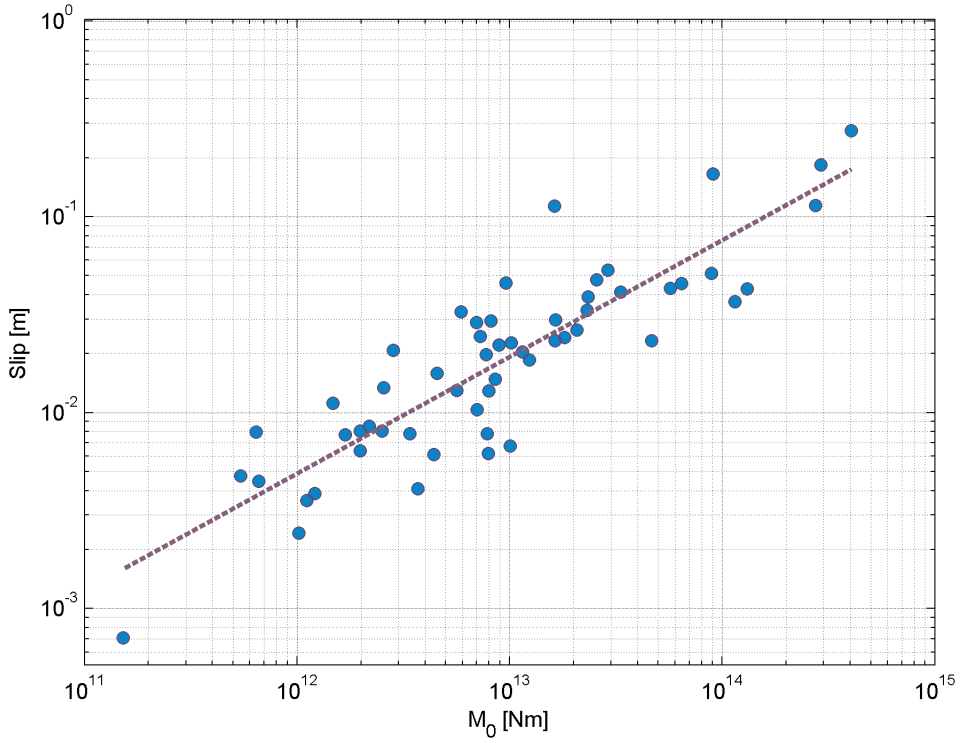

Figure 3.14: Slip $\bar{D}$ as a function of seismic moment assuming μ= 33.1 GPa.

Table 3.2: Source parameters obtained from absolute analysis of P waves. The seismic moment M_0 is calculated using the average RP correction.

Event ID	Date	Time	Lat	Lon	Depth [m]	M_L	M_0[Nm]	f_c [Hz]	*err* f_c	r [m]	$\Delta\sigma$ [MPa]	*err* $\Delta\sigma$	$\bar{D}$[mm]
X1466A	2008-10-10	03:22:05.110	50.20819	12.45497	8953	3.3	4.04e14	9.4	0.8	119	105.4	27.4	275
X1590D	2008-10-09	22:20:37.760	50.21028	12.45352	9169	3.3	2.92e14	9.1	0.7	124	67.7	17.6	184
X2411A	2008-10-10	11:18:41.466	50.21600	12.45200	9186	3.0	2.75e14	7.4	0.4	152	34.2	6.5	114
P5559A	2000-11-06	23:31:32.660	50.20863	12.45691	8321	2.7	9.03e13	15.5	0.9	72	103.8	19.8	165
X2002A	2008-10-10	04:22:16.491	50.21014	12.46009	8623	2.6	8.89e13	8.7	0.7	129	18.2	4.7	52
P3282A	2000-09-17	15:14:32.939	50.21812	12.45346	8371	2.5	6.44e13	9.6	0.6	117	17.8	3.4	46
P3887A	2000-10-15	19:11:20.533	50.20758	12.45900	8580	2.5	3.34e13	12.7	0.6	88	21.3	3.4	41
P5342A	2000-11-05	01:05:04.577	50.20752	12.45778	8265	2.5	6.97e12	23.2	1.9	48	27.3	7.1	29
X2144A	2008-10-10	06:34:48.785	50.20475	12.45650	8820	2.5	5.70e13	9.9	0.8	113	17.4	4.5	43
P1197A	2000-09-03	17:11:03.056	50.21352	12.45320	9501	2.4	1.63e13	30.1	2.4	37	138.4	35.9	113
P5164A	2000-10-29	05:10:46.834	50.21521	12.45555	7881	2.4	1.15e14	6.5	0.5	173	9.7	2.2	37
X1590C	2008-10-09	22:20:33.917	50.20862	12.45419	9238	2.4	1.31e14	6.5	0.5	172	11.3	2.9	43
P2179A	2000-09-08	09:14:00.927	50.21171	12.45370	9232	2.3	2.90e13	15.5	0.9	72	33.7	6.4	54
X1893A	2008-10-10	03:18:36.206	50.20695	12.45487	9005	2.2	2.31e13	13.7	1.0	82	18.5	4.2	33
X2136A	2008-10-10	06:27:20.585	50.20804	12.45489	9039	2.2	4.66e13	8.1	0.6	139	7.6	2.0	23
X2678A	2008-10-10	16:20:35.324	50.21110	12.45492	9941	2.2	2.34e13	14.7	0.9	76	23.4	4.5	39
X3730A	2008-10-12	06:39:48.481	50.21088	12.45447	8858	2.1	2.56e13	15.6	1.7	72	30.1	11.1	48
P1237A	2000-09-03	18:23:50.733	50.21286	12.45286	9357	2.0	1.15e13	15.2	0.8	74	12.6	2.0	20
P1442A	2000-09-03	23:38:12.296	50.22071	12.45097	8813	1.9	7.83e12	11.4	0.5	98	3.6	0.5	8
P1900A	2000-09-04	16:18:12.444	50.21409	12.45360	8784	1.9	7.93e12	10.1	0.6	111	2.5	0.5	6

Event ID	Date	Time	Lat	Lon	Depth [m]	M_L	M_0[Nm]	f_c [Hz]	*err* f_c	r [m]	$\Delta\sigma$ [MPa]	*err* $\Delta\sigma$	$\bar{D}$[mm]
P2278A	2000-09-08	12:00:15.233	50.21367	12.45305	9678	1.9	2.07e13	12.9	0.8	87	13.9	2.6	26
X6694A	2008-10-21	03:02:43.457	50.22127	12.45114	8715	1.9	1.64e13	15.4	1.5	73	18.6	6.2	30
X874A	2008-10-08	00:14:40.792	50.20391	12.45478	9719	1.9	1.24e13	14.0	1.1	80	10.6	2.7	19
P1427A	2000-09-03	23:18:37.490	50.22088	12.45164	8809	1.8	4.39e12	13.5	0.9	83	3.4	0.8	6
P3730A	2000-10-15	16:38:47.753	50.20651	12.45871	8876	1.8	3.40e12	17.3	1.0	65	5.5	1.0	8
X1266A	2008-10-08	16:55:00.774	50.20904	12.45368	9138	1.8	7.04e12	13.8	1.1	81	5.8	1.5	10
X1732A	2008-10-10	00:28:08.477	50.21286	12.45312	8889	1.8	8.57e12	15.0	1.2	75	9.0	2.3	15
X2263A	2008-10-10	08:30:22.758	50.21484	12.45511	9102	1.8	7.77e12	18.2	1.6	61	14.7	4.3	20
X3143A	2008-10-11	05:07:10.254	50.22131	12.45131	8930	1.8	1.63e13	13.6	1.0	82	12.9	2.9	23
X3148A	2008-10-11	05:13:27.098	50.22112	12.45121	8669	1.8	1.02e13	17.1	1.5	66	15.7	4.6	23
X840A	2008-10-07	23:49:32.974	50.20265	12.45676	9574	1.8	8.17e12	21.7	1.9	52	25.9	7.6	29
P5475A	2000-11-06	22:11:37.679	50.21028	12.45566	8465	1.7	1.01e13	9.4	0.7	120	2.6	0.6	7
P5516A	2000-11-06	22:51:59.989	50.20728	12.45931	7925	1.7	7.27e12	21.0	1.5	53	20.8	4.7	24
P940A	2000-09-01	08:37:52.979	50.21285	12.45308	9720	1.7	5.90e12	26.9	1.9	42	35.7	8.0	33
X1992A	2008-10-10	04:13:25.704	50.21247	12.45312	9554	1.7	8.90e12	18.0	1.6	62	16.2	4.8	22
X3169A	2008-10-11	05:55:01.819	50.22074	12.45102	8772	1.7	1.81e13	13.2	1.1	85	12.9	3.3	24
X402A	2008-10-06	03:47:54.129	50.19978	12.45766	9667	1.7	7.99e12	14.5	1.0	77	7.6	1.7	13
P1210A	2000-09-03	17:27:29.689	50.21121	12.45379	9522	1.6	5.65e12	17.3	1.0	65	9.2	1.7	13
P3752A	2000-10-15	16:56:54.116	50.20332	12.45910	8898	1.6	9.59e12	24.9	2.0	45	46.4	12.0	46
P6415A	2000-11-09	04:02:52.333	50.20930	12.45449	9270	1.5	5.44e11	33.7	3.7	33	6.5	2.4	5
P1479A	2000-09-04	00:16:13.569	50.21910	12.45148	8846	1.4	3.69e12	12.0	0.7	93	2.0	0.4	4
P3781A	2000-10-15	17:18:44.156	50.21004	12.45488	9316	1.4	4.56e12	21.3	1.3	53	13.7	2.6	16
P3833B	2000-10-15	18:15:01.676	50.20102	12.45829	8661	1.4	1.02e12	17.6	1.6	64	1.7	0.5	2
P5517A	2000-11-06	22:53:44.166	50.20248	12.45804	9140	1.4	2.51e12	20.5	1.6	55	6.7	1.7	8

Event ID	Date	Time	Lat	Lon	Depth [m]	M_L	M_0[Nm]	f_c [Hz]	*err* f_c	r [m]	$\Delta\sigma$ [MPa]	*err* $\Delta\sigma$	$\bar{D}$[mm]
P1070A	2000-09-03	12:47:05.706	50.21368	12.45318	9056	1.3	2.56e12	26.2	1.8	43	14.3	3.2	13
P1237B	2000-09-03	18:23:49.674	50.21322	12.45230	9367	1.3	2.18e12	22.6	1.6	50	7.8	1.8	9
P1311A	2000-09-03	20:38:54.595	50.21730	12.45265	8869	1.3	1.98e12	23.0	1.4	49	7.5	1.4	8
X1153A	2008-10-08	06:20:50.839	50.20826	12.45419	9330	1.3	1.98e12	20.5	1.8	55	5.3	1.6	6
P5247A	2000-10-29	09:35:20.188	50.21813	12.45385	7977	1.2	6.43e11	40.1	4.4	28	12.9	4.8	8
P5627A	2000-11-07	00:38:12.095	50.20880	12.45470	9371	1.2	1.11e12	20.4	1.6	55	2.9	0.8	4
P1373A	2000-09-03	22:14:29.709	50.21822	12.45191	8747	1.1	1.47e12	31.5	2.8	36	14.3	4.2	11
X1240A	2008-10-08	14:11:49.501	50.20148	12.45759	9055	1.1	1.69e12	24.4	2.2	46	7.6	2.3	8
X1462A	2008-10-09	12:48:36.360	50.21006	12.45396	9331	1.0	1.21e12	20.4	2.0	55	3.2	1.1	4
P3533A	2000-09-19	10:30:42.102	50.21760	12.45158	9328	0.9	2.84e12	30.9	2.5	36	26.0	6.8	21
P6304A	2000-11-08	04:51:11.492	50.20253	12.45741	9417	0.9	1.52e11	24.7	2.0	45	0.7	0.2	1
P3997A	2000-10-16	01:38:42.663	50.20923	12.45422	9391	0.8	6.61e11	29.7	3.3	38	5.4	2.0	4

The uncertainty of f_c was estimated as an interval where the residual function increases by 5 % (gray circles in Fig. 3.4). For most events the error does not exceed 1 Hz for the low corner frequencies and 3 Hz for the high corner frequencies (Tab. 3.2). The $err\ f_c$ values in Tab. 3.2 are calculated as the half from the difference of the upper and lower uncertainty limits of f_c. The $err\ \Delta\sigma$ is calculated from (2.7) and (2.17) using the $f_c + err\ f_c$ as the corner frequency input. [1]

Finally I compared corner frequencies obtained by spectra inversion with those determined by the method of Snoke (1987); Eq. (2.22). Figure 3.15 shows the corner frequencies using two approaches: first the attenuation is neglected (black crosses) and second the attenuation is corrected for (red circles) by using the Q-factor obtained from inversion. Snoke's corner frequency $f_c(J)$ is calculated as a mean value for each event over all available stations. In the ideal case the relation between $f_c(inv)$ and $f_c(J)$ should be 1:1. The linear regression has form

$$f_c(J) = 0.967\, f_c(inv) + 2.317 \tag{3.8}$$

with correlation coefficient 0.986. The 95 % confidence interval is shaded by light red. There is a systematic shift (+ 2.317) of $f_c(J)$ which can be caused by overestimating the high frequency correction term while evaluating the J integral after the attenuation correction. If the correction for attenuation is not applied the Snoke's method fails. It is found that if the spectra are corrected for attenuation the Snoke's method gives very similar corner frequencies as the spectra inversion method. Therefore if we know the correct Q factors the corner frequency could be calculated directly from the corrected data without the inversion process. In the following analysis I used the corner frequencies determined by the spectra inversion.

Joint inversion

Stability of the joint inversion was tested by omitting the individual stations. Jackknife test is shown in Fig. 3.16b, where the relative change of the minimum of the residual function (3.3) is compared to the minimum of SR_{joint} for all stations. Increased value means that the specific station is somehow important for the stability (BUBD, NKC, POLD, STC, TRC).

I also tested stability of the solution by changing the initial values. As long as I was selecting the initial values from the appropriate intervals ($f_c \in \langle 5; 30\rangle$; $Q \in \langle 100; 300\rangle$) the final solutions converge to similar values within the range of approx. 15 % difference. The difference between the solutions is probably due to relatively flat SR_{joint} function which can be slightly oscillating around its minimum. This inversion is an overdetermined problem whose solution may not be unique.

Results of Q in Fig. 3.16a are plotted for two approaches. First as results of the joint inversion over all stations (blue crosses) and second as the mean values (red error bars) while omitting the single stations (individual solutions by gray dots). The value

[1] The $err\ f_c$ column in Michálek & Fischer (2013) is calculated by different approach and the errors are underestimated.

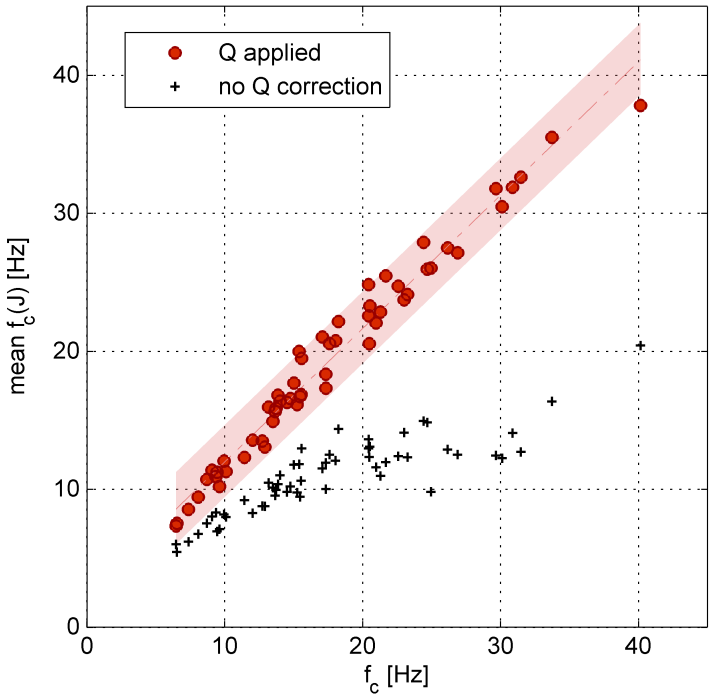

Figure 3.15: Comparison of two approaches for obtaining f_c– the inversion method and the Snoke's method (vertical axis). The linear regression is shown by red line and the 95 per cent confidence interval is shaded in light red.

of the particular Q where the station is omitted is replaced by solution of Q obtained for all the stations. Therefore the means $\bar{Q}^{joint}_{Jack}$ and and their standard deviations σQ^{joint}_{Jack} should be the taken as the representative values of Q (Tab. 3.3) because in these values the station-dependent uncertainties are averaged..

Corner frequencies obtained from the joint inversion are in Fig. 3.17, including the Jackknife test. For half of the events the solution is stable, i.e. the corner frequency from inversion of all stations $f^P_c(all)$ does not differ very much from the mean corner frequency obtained from the Jackknife test $\bar{f^P_c}(Jack)$ and with small standard deviation $\sigma f^P_c(Jack)$ (e.g. X1153A, X1590D, X2002A). In the second half of events we can see two groups. The first group has small $\sigma f^P_c(Jack)$ but the solution of $f^P_c(all)$ differ significantly from $\bar{f^P_c}(Jack)$; e.g. events X1462A or X1732A. This was probably caused by inclusion of some stations whose Q-factor was unstable (e.g. POLD or ZHC). Omitting of these stations leads to stable solution. The second group has high $\sigma f^P_c(Jack)$ and solution for these events is probably badly conditioned generally but the number of stations does not correlate with unambiguity of the solution. Comparison of corner frequencies obtained by different absolute methods is given in Tab. 3.7. Whereas for Q-factor the joint inversion led to stabilization, for corner frequencies it had an opposite effect. Corner frequencies from the joint inversion show higher scatter than corner frequencies $f^P_c$from inversion of the individual events. Interesting result is, that f^P_c from individual inversion and $\bar{f^P_c}(Jack)$ have almost the same values where $\sigma f^P_c(Jack) < 4$ Hz. The only exception is event X1590C, whose f^P_c is unrealistic low.

Station	$\bar{Q}^{indiv}$	$err\,Q^{indiv}$	NumEv	$\bar{Q}^{joint}_{Jack}$	σQ^{joint}_{Jack}	Q^{joint}
BUBD	288	68	23	237	17	212
HOPD	380	119	19	221	19	211
HRED	167	74	22	136	14	129
KAC	224	119	15	145	21	120
KOC	295	97	51	214	21	191
KOPD	144	75	18	117	51	87
KRC	230	109	57	162	12	150
KVC	168	101	16	144	88	92
LAC	254	76	26	206	13	210
LBC	305	463	46	120	12	105
LOUD	210	79	24	153	12	147
NKC	254	140	14	212	125	137
PLED	242	206	20	184	66	131
POC	227	76	15	162	10	156
POLD	569	169	4	401	131	355
SNED	155	53	22	185	169	117
STC	208	102	38	129	14	112
TRC	408	220	16	247	19	233
VAC	173	77	48	123	117	97
ZHC	398	17	3	348	104	425

Table 3.3: The quality factor Q for individual stations obtained by different absolute approaches applied to P waves. First two columns are related to the inversion of individual events (upper index *indiv*) calculated as a mean value for all available events and the standard deviation, respectively. In the third column is number of events analyzed at each particular station. The last three columns are results from the absolute joint inversion (upper index *joint*). Results with lower index *Jack* are obtained by jackknifing individual stations.

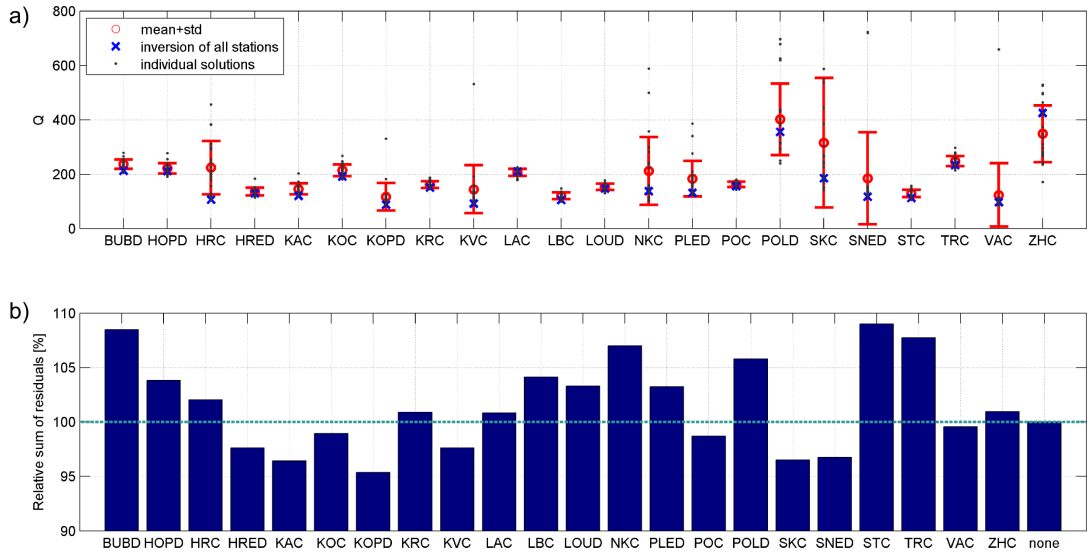

Figure 3.16: Results of Q from the absolute joint inversion and its deviations obtained by Jackknife test (a) and distribution of relative SR for omissions of individual stations.

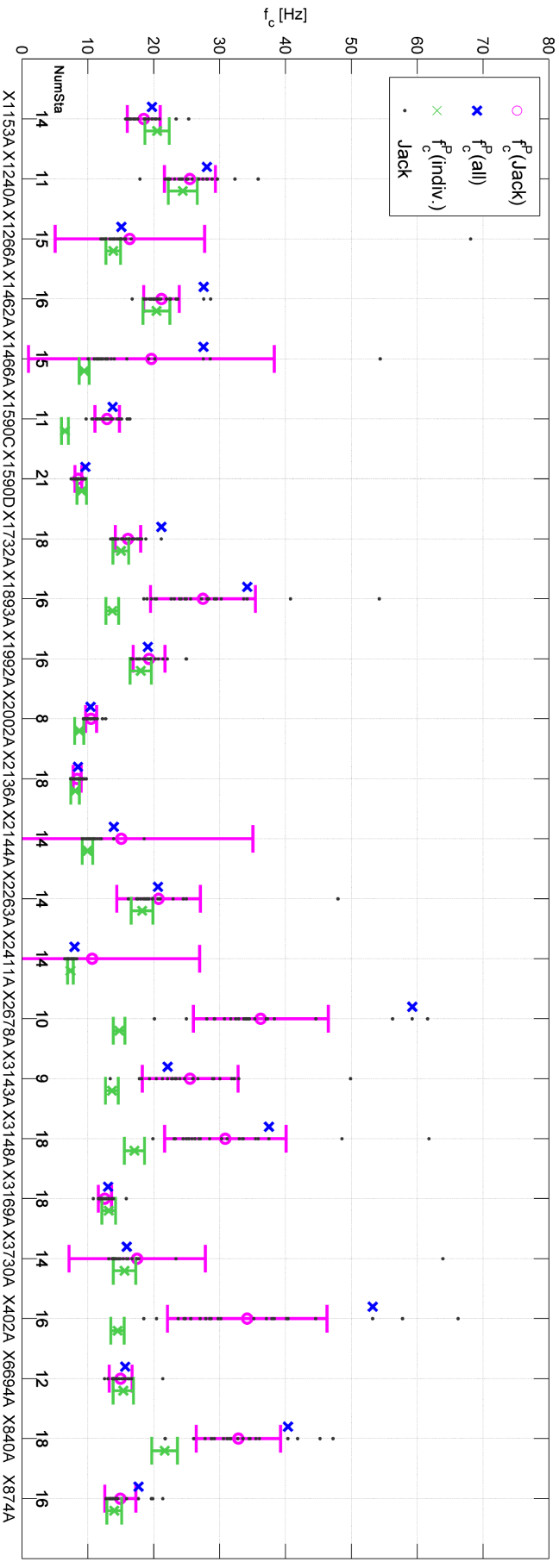

Figure 3.17: Results of corner frequencies from the absolute joint inversion ($f_c^P(all)$; blue crosses) including the Jackknife test ($\bar{f_c^P}(Jack) \pm \sigma f_c^P(Jack)$; magenta error bars) and absolute individual inversion (f_c^P; green error bars).

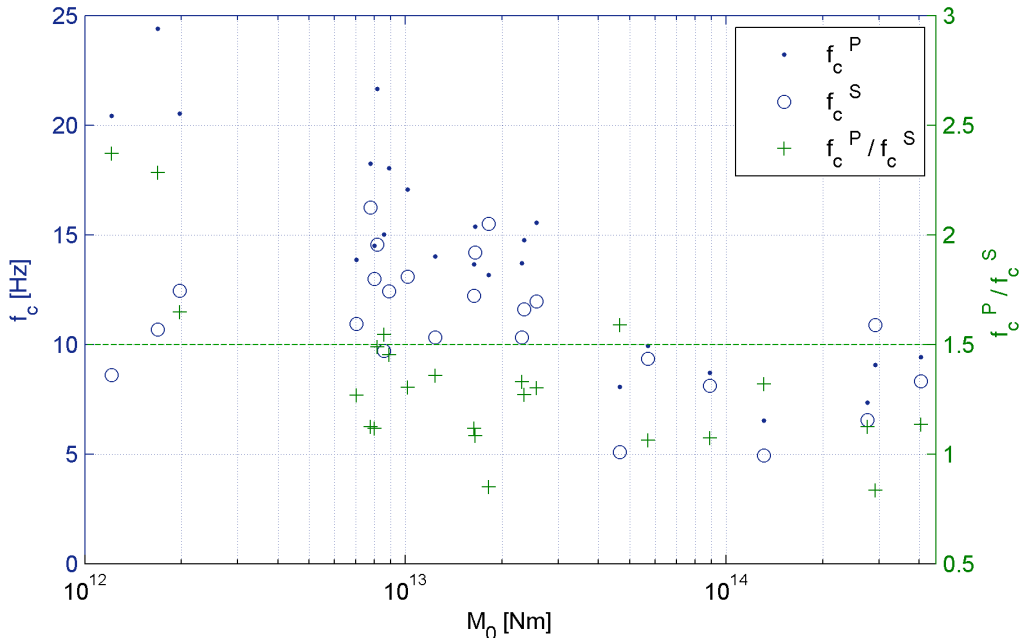

Figure 3.18: Comparison of corner frequencies obtained from analysis of P waves and S waves and their ratio.

3.4 Application of the absolute methods to S waves

Most of the studies analyzing the source parameters of earthquakes are using primarily S waves because their radiation pattern has less nodal directions and are more energetic than P waves[2] and therefore have sufficient signal-to-noise ratio even at more and distant stations. In my case when analyzing data of local earthquakes from the West Bohemia region I was able to apply the analysis also to P waves because the network is close to the hypocenters and coverage of the focal sphere is good (Fig. 3.7). To test reliability of results obtained from P waves I applied the same analysis to S waves. The time window was broadened from 0.5 sec (used for P waves) to 1.5 sec to cover the most of the S-wave energy. Onset of the S wave was aligned to the first third of the time window, i.e. 0.5 sec.

Because of the near-vertical incidence angles of the rays at stations the conversion coefficient F_{SH}^{surf} is always 2.0 and for F_{SV}^{surf} is $\sim$ 2.0 (Cerveny, 2005; Fig. 5.11), which is similar to the P-wave conversion coefficient of $\sim$ 2.0. Therefore I used the mean spectrum of S waves from both horizontal components instead of rotation of the components into the SH and SV. All other parameters and initial conditions for the inversion were the same as for the P-wave analysis.

3.4.1 Results

Source parameters of 24 events using the S waves from the 2008 swarm were analyzed; results are shown in Fig. 3.18.

[2]For Poisson solid is $E_S/E_P \sim 20$

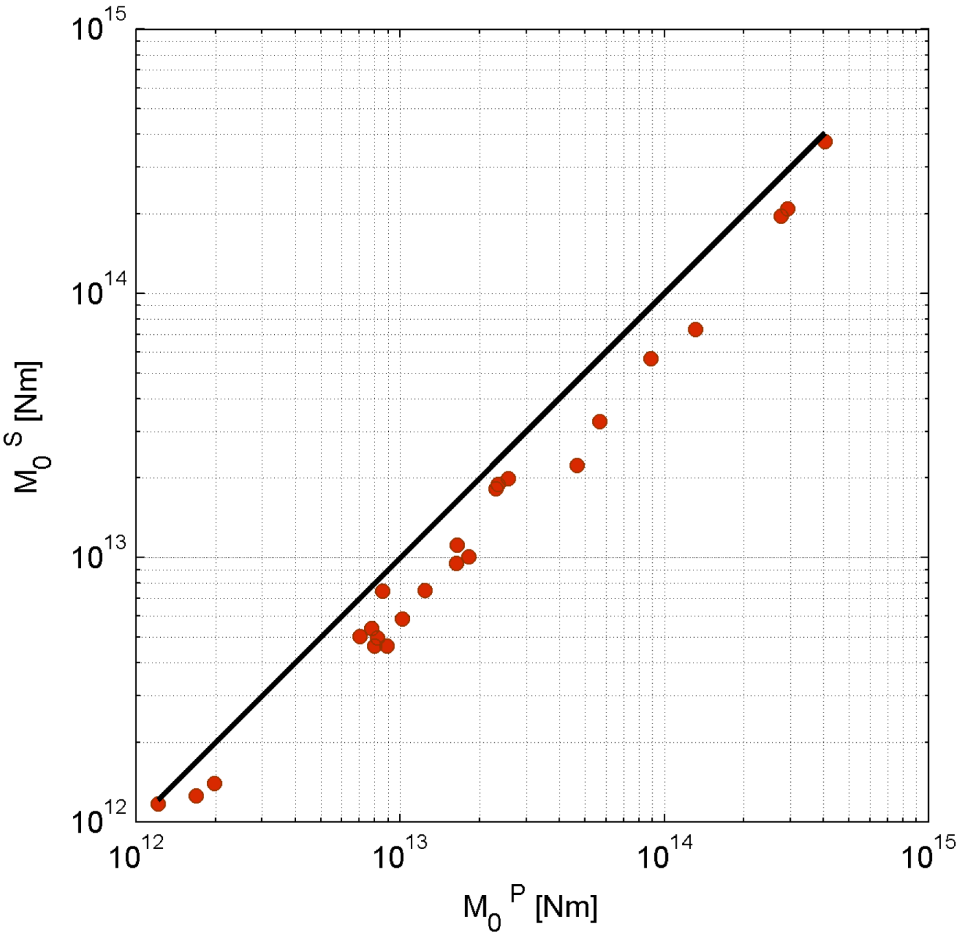

Figure 3.19: Comparison of seismic moments M_0^P and M_0^S

According to the theoretical study of earthquake source by Madariaga (1976) the ratio of corner frequencies f_c^α/f_c^β should be around 1.5 for the instantaneous circular crack (for directions at angles greater than 30° measured from the fault plane). The narrower P pulse is related to more high-frequency content than in the S pulse. This could be explained by the fact that, in the case of finite source, the P pulse arrivals from the closest and farthest points on the rupture edges will be less separated in time due to the higher velocity of P waves (Madariaga, 1976). In this study I found that f_c^α/f_c^β is most often between 1.0 and 1.5. For two small events the ratio is greater than 2 which is due to low values of f_c^β. The high-ratio values for the small events could be also an effect of the higher uncertainty of f_c.

The majority of the observational studies support generally that $f_c^\alpha > f_c^\beta$ (Aki & Richards, 2002). According to Furuya (1969) the difference for microearthquakes can be explained by different attenuation of P and S waves, i.e. $Q_P > Q_S$. He also pointed out that the simple propagating fault model cannot explain such observations.

As Q is a secondary output parameter of the inversion it is worthwhile to compare results of Q from both wave types. The comparison was made at each station separately and shown in Fig. 3.21. While Q_P is quite stable over all stations, Q_S at some stations (namely BUBD, HOPD, KOPD, LOUD, POLD and SNED) shows very high and un-

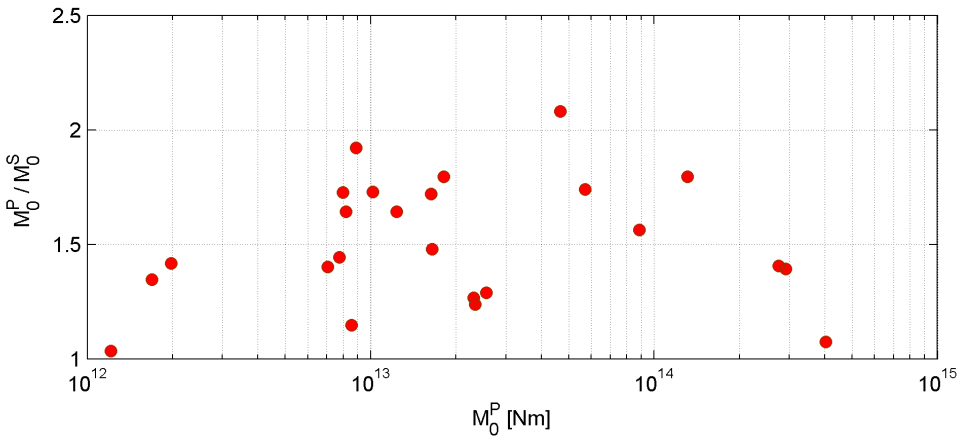

Figure 3.20: Ratio of seismic moments M_0^P and M_0^S

stable values. On the other hand for most of the stations the Q_S is stable and median of Q_S/Q_P ratios is 1.32. It is commonly assumed that this ratio of quality factors is well approximated by $Q_S/Q_P = 4/3(\beta/\alpha)^2 = (4/9) = 0.4$ (Burdick, 1978), for $\alpha/\beta = \sqrt{3}$. Results similar to ours were obtained by Kwiatek et al. (2011) from analysis of very weak events in the deep mines in South Africa ($Q_S/Q_P = 1.4$) and also by Bennington et al. (2008) around the SAFOD site. Bethmann et al. (2012) observed $Q_S \sim Q_P$ while analyzing attenuation underneath the city Basel in Switzerland. Hauksson & Shearer (2006) suggest that $Q_S/Q_P > 1$ (in the southern California crust) can be caused by partially fluid-saturated rocks (based on laboratory study of Toksöz et al., 1979). I am aware that our Q-factors are results of the average attenuation along the whole ray path and can not be interpreted with the direct connection to the rock properties in hypocentral depths even though the role of fluids as triggering and driving forces is a frequently discussed topic in the WB region. On the other hand from comparison of results of corner frequencies from P and S waves one would expect opposite ratio of quality factors, i.e. $Q_S/Q_P < 1$.

Comparison of seismic moments obtained from P wave and S wave analysis (Fig. 3.19 and Fig. 3.20) gives an interesting finding that M_0^P is in average 1.51±0.27 times greater than M_0^S. This could be explained by a) higher attenuation of S waves, b) increased ratio of velocities in the source region compared to $\alpha/\beta = 1.73$, which is used in this study. The former possibility a) is not consistent with results of the inversion where I observed opposite ratio of Q_S/Q_P. One should keep in mind that Q in this study is determined as a secondary parameter and is mainly affected by the pulse width, not by the decay of amplitudes which are related to M_0. Therefore Q can not affect values of M_0 in my case. The possibility b) would imply increased α/β ratio in the source volume; in particular the ratio $M_0^P/M_0^S = 1.51$ would need $\alpha/\beta = 1.9$ which is unrealistically high.

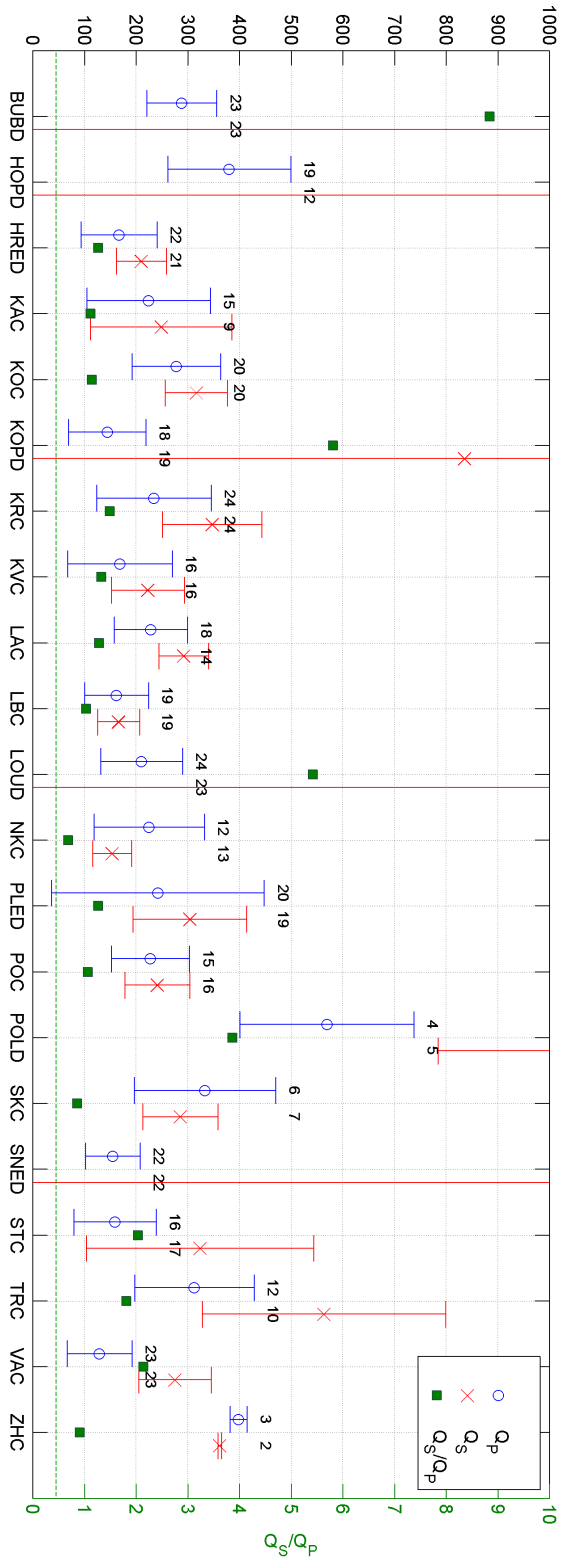

Figure 3.21: Comparison of quality factors Q_P and Q_S for 24 selected events at individual stations and their ratios. Mean value at each station is plotted with an error bar which correspond to the standard deviation of the available values. The number above the upper error bar is number of events from which the mean and standard deviation is calculated. Ratios of the means is plotted by green squares.

		Individual inversion				Joint inversion			
Event ID	M_L	f_c^P	$err\, f_c^P$	f_c^S	$err\, f_c^S$	$\bar{f_c^P}(Jack)$	$\sigma f_c^P(Jack)$	$f_c^P(all)$	NumSta
X1466A	3.3	9.4	0.8	8.3	0.7	19.6	18.7	27.5	15
X1590D	3.3	9.1	0.7	10.9	1.1	8.5	0.5	9.6	21
X2411A	3.0	7.4	0.4	6.5	0.5	10.7	16.3	8.0	14
X2002A	2.6	8.7	0.7	8.1	0.6	10.5	0.8	10.4	8
X2144A	2.5	9.9	0.8	9.4	0.7	15.1	20.0	13.9	14
X1590C	2.4	6.5	0.5	4.9	0.3	12.9	1.9	13.8	11
X1893A	2.2	13.7	1.0	10.3	1.0	27.5	8.0	34.2	16
X2136A	2.2	8.1	0.6	5.1	0.3	8.4	0.6	8.5	18
X2678A	2.2	14.7	0.9	11.6	0.9	36.3	10.2	59.3	10
X3730A	2.1	15.6	1.7	12.0	1.0	17.5	10.4	15.9	14
X6694A	1.9	15.4	1.5	14.2	1.1	15.0	1.7	15.7	12
X874A	1.9	14.0	1.1	10.3	0.8	14.9	2.4	17.7	16
X1266A	1.8	13.8	1.1	10.9	0.9	16.4	11.4	15.1	15
X1732A	1.8	15.0	1.2	9.7	0.9	16.1	1.9	21.2	18
X2263A	1.8	18.2	1.6	16.2	1.3	20.7	6.3	20.6	14
X3143A	1.8	13.6	1.0	12.2	0.9	25.5	7.3	22.1	9
X3148A	1.8	17.1	1.5	13.1	1.2	30.9	9.2	37.5	18
X840A	1.8	21.7	1.9	14.6	1.6	32.9	6.4	40.4	18
X1992A	1.7	18.0	1.6	12.4	0.9	19.3	2.4	19.1	16
X3169A	1.7	13.2	1.1	15.5	1.2	12.6	1.0	13.1	18
X402A	1.7	14.5	1.0	13.0	1.2	34.2	12.1	53.3	16
X1153A	1.3	20.5	1.8	12.4	1.0	18.5	2.5	19.7	14
X1240A	1.1	24.4	2.2	10.7	0.6	25.5	3.9	28.1	11
X1462A	1.0	20.4	2.0	8.6	0.8	21.2	2.7	27.6	16

Table 3.4: Comparison of corner frequencies from the absolute methods – inversion of individual events and joint inversion of all events together. The columns $\bar{f_c^P}(Jack)$ and $\sigma f_c^P(Jack)$ were determined as a mean and standard deviation respectively, while jackknifing individual stations. Column $f_c^P(all)$ is result obtained from inversion of all stations together.

3.5 Application of the relative methods to P waves

The swarm-like activity in the WB region is an ideal case for study, because the activity is highly concentrated in small area with groups of typical focal mechanisms (Horalek et al., 2002; Fischer & Horálek, 2003; Fischer & Michálek, 2008). The selection of events for application of the relative method was created by intersection of the event groups in clusters found by cross-correlation analysis (Fischer & Michálek, 2008) and here analyzed 2008-swarm events. The selection of 6 events is in Tab. 3.5. The requirement of the same set of stations for each event resulted in 9 stations (station LAC was found not suitable for its low signal-to-noise ratio). All events have similar focal mechanisms (the mean values and standard deviation are respectively: strike = 154.8°±7.2°; dip = 63.0°±2.1°; rake = -19.5°±2.5°.

3.5.1 Inversion process

To avoid numerical instabilities due to possible high-frequency oscillations of the spectra and consequently due to division by inappropriate values in the EGF method, the spectra were resampled to 12 points per decade to be evenly spaced in the log scale of frequency. The original sampling of frequency was [1:1:125] Hz. Values of the spectra at each frequency point were geometrically averaged in the appropriate frequency bins that were broadening with increasing frequency. Nevertheless, it was found that thanks to the smooth MTT spectral estimate the averaging in frequency bins does not influence the inversion results notably but decrease the minimum of the residual function and also makes the residual function narrower around its minimum.

Another instability could arise from division by a low value. But here I would like to note that even though the spectral amplitudes are low in the absolute sense they have comparable values which differ usually by one order but mostly about two orders. Therefore such numerical instability should not occur in this case.

The ratio of the low frequency plateau Ω_{0r} in (2.32) is generally used as a free parameter in the inversion but because the low frequency parts of spectra are nearly flat I fixed Ω_{0r} to ratio of the mean spectral amplitudes from the 1-3 Hz frequency range during the inversion which decreased the number of fitted parameters.

3.5.2 Individual pairs of events

I applied both approaches mentioned in section 2.5.1, always using the strongest event as a mainshock and all weaker events as the EGF. Normalized displacement seismograms of 6 events at 10 stations are shown in Fig. 3.22.

First, I investigated each pair of events individually using the approach (a), i.e. inverting one f_{c1} and one f_{c2}. Results are given in Tab. 3.5. Two events X3730A and X874A deconvolved from the mainshock give reasonable values of f_{c1} and also event X840A has an acceptable value of f_{c1}. Corner frequencies f_{c2} for these events are also comparable to the corresponding f_c^{abs} values and f_{c1} is comparable to f_c^{abs} of the X1590D event obtained from the absolute approach. Example for the most stable solution of

Event ID	M_L	f_{c1}^{single}	$err\, f_{c1}^{single}$	f_{c2}^{single}	$err\, f_{c2}^{single}$	SR_{EGF}^{single}	f_c^{abs}
X1590D	3.3	–	–	–	–	–	9.1
X3730A	2.1	10.9	8.3-14.2	19.1	13-27	131	15.6
X874A	1.9	8.4	3-21	11.2	1-	1609	14.0
X1266A	1.8	38.6	22-90	92.1	50-	3000	13.8
X1732A	1.8	27.5	21-37	82.4	50-	879	15.0
X840A	1.8	15.1	11.5-19.5	28.4	20-42	1545	21.7

Table 3.5: Results of the EGF inversion using the single event pairs. There are results from the absolute approach for comparison in the last column.

Event ID	i	M_L	$f_{ci}^{jointEGF}$	$err\, f_{ci}^{jointEGF}$	f_{ci}^{abs}	$f_c^{abs}/f_{ci}^{jointEGF}$
X1590D	1	3.3	13.4	9.5-19.5	9.1	0.68
X3730A	2	2.1	24.8	16-40	15.6	0.63
X874A	2	1.9	18.7	13-28	14.0	0.75
X840A	2	1.8	24.3	15.8-40	21.7	0.88

Table 3.6: Results of joint inversion of corner frequencies of three EGF events and their relation to results of corner frequencies from the absolute approach ($SR_{EGF} = 1120$).

event pair X1590D/X3730A is shown in Fig. 3.23. For the other two events X1266A and X1732A the both corner frequencies f_{c1} and f_{c2} are out of the acceptable limits. Such unrealistic solution probably comes from the unstable spectra of the weaker event (mainly at the high frequencies) which was transferred to the spectral ratio (compare to Fig. 3.24). Therefore using the smallest event as the EGF does not always lead to the best solution. Uncertainty of the corner frequency f_{c1} was determined by similar approach as in the absolute method, i.e. the f_{c1} is fixed and varied in discrete steps around the optimal solution and increase of the normalized residual function by 5 % is taken as the reliable interval (see e.g. Fig. 3.23). The lower and upper limits of the interval shows also the corresponding values for f_{c2}.

3.5.3 Joint inversion of more event pairs

The second approach I applied was the spectral ratio method for combination of data from more events simultaneously and searching for one f_{c1} and N values of f_{c2}. This approach should lead to more stable solution of f_{c1} of the mainshock X1590D. I selected only events whose individual EGF inversion results were stable, i.e. events X3730A, X874A and X840A. Results of the joint inversion are given in Tab. 3.6 and shown in Fig. 3.25. As the results of the joint EGF method should be better constrained then the single event pairs EGF inversion I will discuss only the results of the joint inversion hereafter. Comparison with the results of the absolute approach the f_c obtained by EGF inversion show higher values by about 12 – 37 %.

3.5.4 Average EGF

The average EGF spectrum was created from events X3730A, X840A and X874A, whose magnitude differences are within the 0.3 bin level. Results of inversion for the X1590D event as a main event and comparison of corner frequencies of this event obtained by the

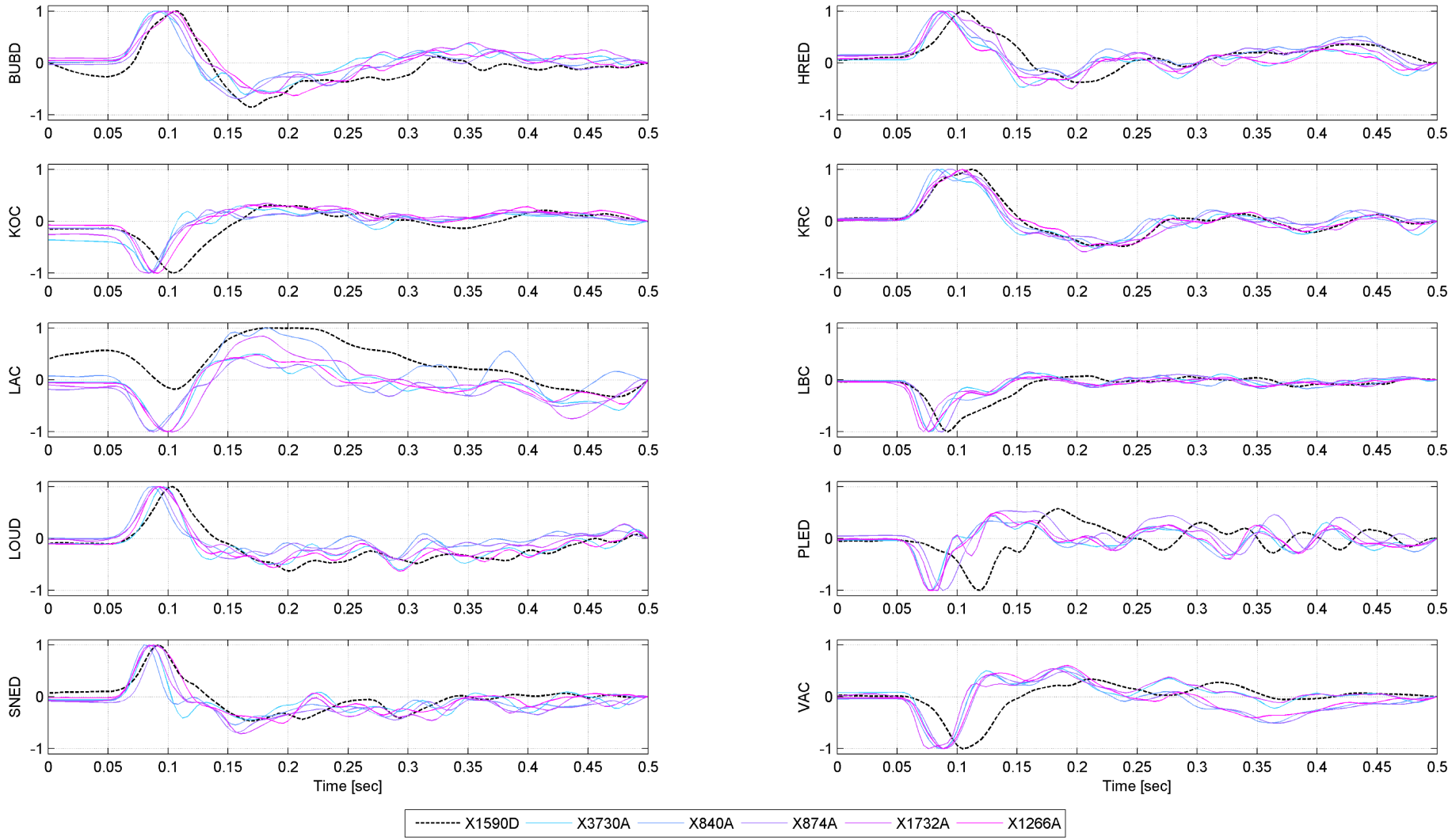

Figure 3.22: Normalized displacement seismograms of P waves on Z component of 6 events at 10 stations. The mainshock event X1590D is plotted by dashed black line.

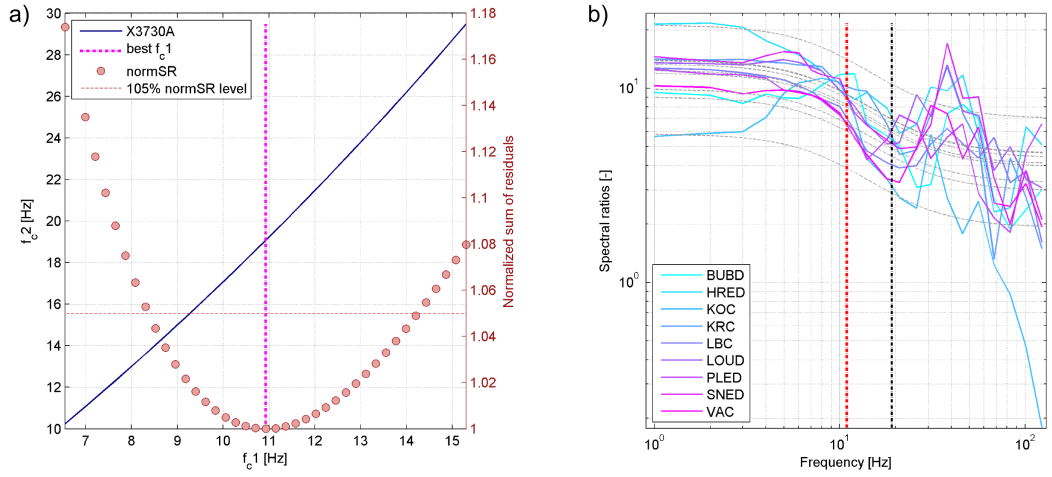

Figure 3.23: EGF inversion of 1590D/X3730A event pair. (a) Uncertainty of the corner frequency while ranging f_{c1} around its optimum value (vertical magenta line) is determined as intersection of the residual function with 1.05 SR level. Behavior of f_{c2} during individual inversions with fixed f_{c1} is plotted by solid dark curve. Spectral ratios (b) at all stations resampled to log scale in frequency are by solid lines. The best fitted source model at each station is plotted by dashed gray curve. The vertical dashed lines are corner frequencies (f_{c1} red; f_{c2} black) of the models.

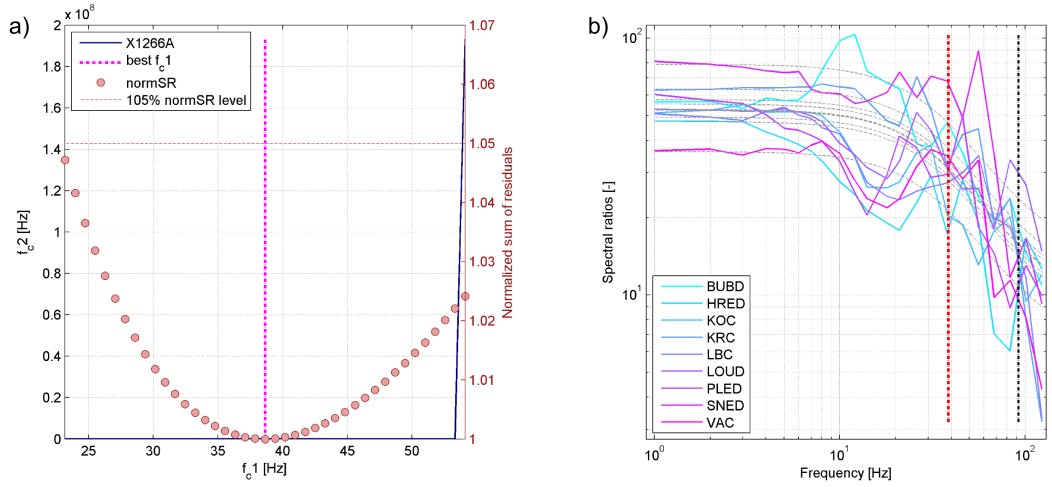

Figure 3.24: EGF inversion of 1590D/X1266A event pair. For description of plots see caption in Fig. 3.23.

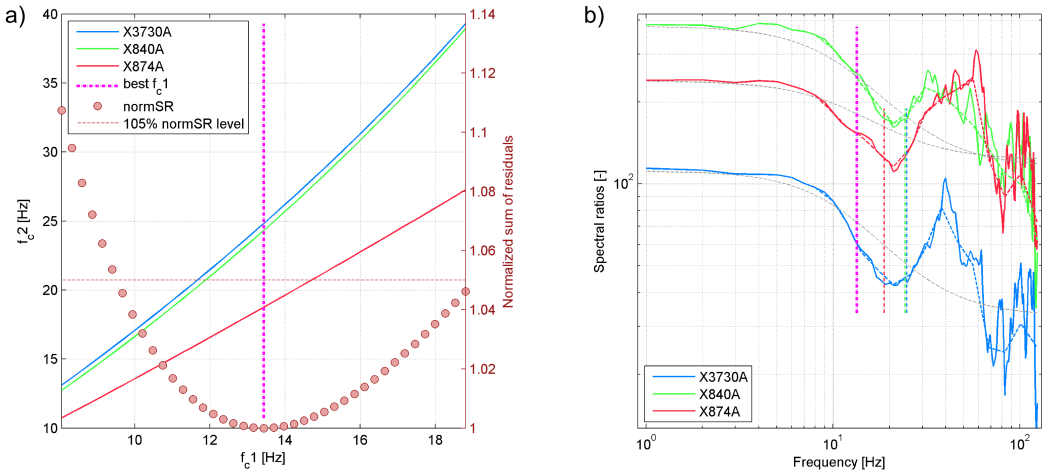

Figure 3.25: Results of joint inversion of corner frequency of event X1590D using three events as EGFs. (a) Uncertainty of corner frequencies while ranging f_{c1} around its optimum value (vertical magenta line) and values of f_{c2} of the corresponding events. Average spectral ratios (b) of all event pairs are calculated as a mean from all stations. Solid line is full ratio curve, the dashed line of the same color is the fitted curve by the model and is resampled to log scale in frequency. The best fitted source models are plotted by dashed gray curves. The vertical dashed lines are appropriate corner frequencies of the models.

Approach	Absolute				Relative (EGF)		
Inversion method	Individual		Joint (jack)	Joint	Pairs - individ.	Pairs - joint	Average
Phase analyzed	P	S	P	P	P (X3730A)	P	P
f_c	9.1	10.9	8.5	9.6	10.9	13.4	12.6
$err\ f_c$	0.7	1.1	0.5	–	3.0	5.0	3.5

Table 3.7: Comparison of f_c and its uncertainty of the average EGF approach (last column; SR=131) and the other approaches for the X1590D event.

other methods are in Tab. 3.7 and shown in Fig. 3.26. One can see that errors of the relative methods have generally higher uncertainties even though the relative methods should provide more precise results than the absolute methods. This discrepancy comes not from the physics but from the character of the fitted data because the spectral ratios are less stable, especially in the high frequencies, than the spectra itself in the absolute sense.

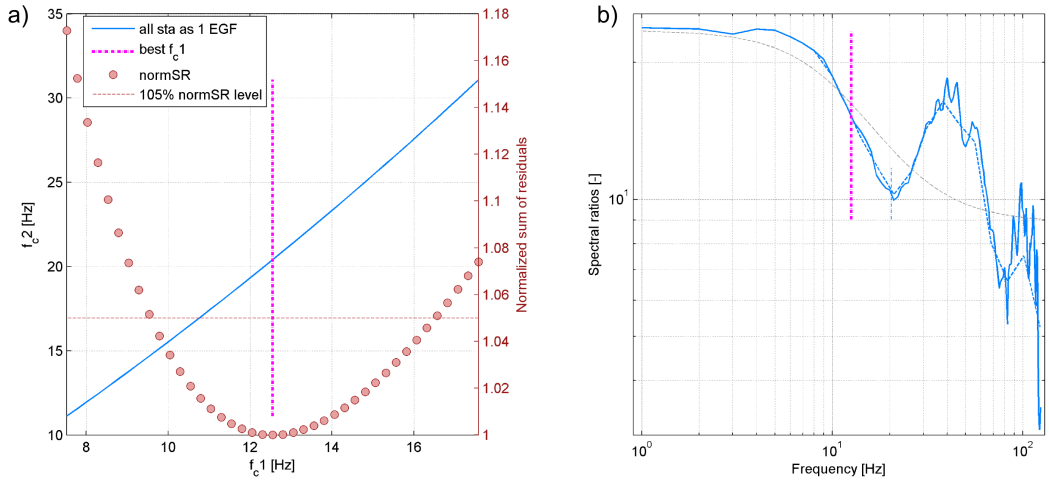

Figure 3.26: Results of the average EGF approach. (a) Uncertainty of corner frequencies while ranging f_{c1} around its optimum value (vertical magenta line) and values of f_{c2} of the average EGF event (blue line). (b) Spectral ratio of X1590D and the average EGF event. The dashed line was fitted by the model. The vertical lines correspond to f_{c1} and f_{c2}.

Chapter 4

Discussion

4.1 Seismic moment

Seismic moment should be one of the best conditioned source parameters. This is true in the ideal case having homogeneously covered focal sphere by stations. As analyzed in section 3.3.5, inclusion of even relatively well known and precise RP corrections can distort the results heavily especially if only few stations are available and, in the worst case, close to the nodal lines. The RP corrections applied at individual stations can increase the uncertainty of the seismic moment, due to division by small RP value for stations close to the nodal lines. In case of badly covered network it is therefore better to apply the average RP correction coefficient $\langle \Re_c \rangle$.

In case of well covered focal sphere it is possible to use the advanced AMT method (Vavryčuk, 2011b) which is implemented in the SEISMON processing package, as well as the absolute inversion method. The AMT allows to include the maximum of available corrections rising from the velocity model. But as is shown in section 3.5 all the estimates of the seismic moment are still within the typical 0.3 error of magnitude M_L. If the event is poorly covered by stations (e.g. weak event) and the AMT method is not suitable, the seismic moment is well determined even by the standard absolute method applied to the P waves because the signal-to-noise ratio is naturally higher at stations projected outside the nodal lines and therefore usually only these stations possible to process.

4.2 Corner frequency

To obtain the correct f_c for the selected model of the source the true quality factor Q must be known. As I inverted for f_c and Q simultaneously there was a trade off between these two parameters. The absolute joint inversion over more events is better constrained than a single event inversion and the trade off is reduced. If the standard deviation of the joint inversion solution is low than also the absolute inversion gives very similar results and this can be assumed as an indicator of the stable solution (see Tab. 3.4).

If I consider the EGF results more realistic because of the effective elimination of the path and attenuation effects, it is surprising for me that $f_c^{jointEGF}$ are in average

lower than the f_c^{abs} by a factor of 0.7 (Tab. 3.6), which leads me to a surmise that the quality factors Q from the absolute approach are still probably underestimated and should be even higher to get the same corner frequencies f_c^{abs}. But the EGF method suffer from a much higher uncertainty due to numerical instability and also due to a more flat residual function near its minimum. Therefore the EGF results do not need to be more reliable.

It is of interest to note that the EGF results are more stable for events similar in magnitudes even though the weaker event can not be approximated by the effective $\delta(t)$ function (according to results in Tab. 3.5, event pair X1590D/X3730A has the lowest SR value while having the lowest difference in magnitudes). The higher values of SR are caused very likely by unstable spectra of the weak events, especially for the mid- and high-frequency range. Therefore the spectral ratio method can fail for very weak EGF events. Another possible correction of the oscillating spectra could be achieved by stacking of spectra of the weak events as proposed by Shearer et al. (2006). But even this method does not provide significantly lower $err\ f_c$ (Tab. 3.7).

4.3 Scaling relations - stress drop

The dependence of the source radius on seismic moment (Fig. 3.11) shows a smaller increase than would be expected for the constant stress-drop model. With respect to the scatter of the resolved f_c and M_0 events differing by one order of seismic moment show the same source size. Another measure of similarity of the physical processes governing earthquakes of different size is the apparent stress $\Delta\sigma_a$; eq. (2.18). The radiated energy E_α; eq. (2.19) is calculated at each station separately and for the analysis I use the mean of E_α in the logarithmic scale (i.e. geometric mean). The apparent stress gives the fraction of the total energy radiated by seismic waves and typical values range from 0.01 MPa to 10 MPa (e.g. Kwiatek et al., 2011). In Fig. 4.1 is shown the apparent stress of my dataset ranging over 3 orders from 0.3 kPa to 0.4 MPa. As the apparent stress increases with the seismic moment I could deduce that the small earthquakes are less efficient in radiating the energy than the bigger ones, what supports the non-self-similarity (e.g. Aki, 1967; Kanamori & Anderson, 1975; Mayeda et al., 2005). Provided that the seismic moment is well determined the values of the apparent stress could be underestimated due to the possible underestimation of the radiated energy E_α via J; eq. (2.21). Although I applied the correction terms for bandwidth limitation of the records the corrections might be still insufficient because one should integrate up to the 10^{th} multiple of the corner frequency to incorporate 90 % of the seismic energy (Ide & Beroza, 2001). The upper limit in our seismograms (either f_{max} or the instrument limitations) is around 80-100 Hz, which indicates that for smaller events ($f_c > 10$ Hz; $\sim M_0 <$ 1e13 Nm) the radiated seismic energy is proportionally underestimated. On the other hand the corner frequencies obtained from J are similar to those obtained by spectra inversion, which points to insignificant error in determining J. The relation of seismic moment to local magnitude (Fig. 4.2)

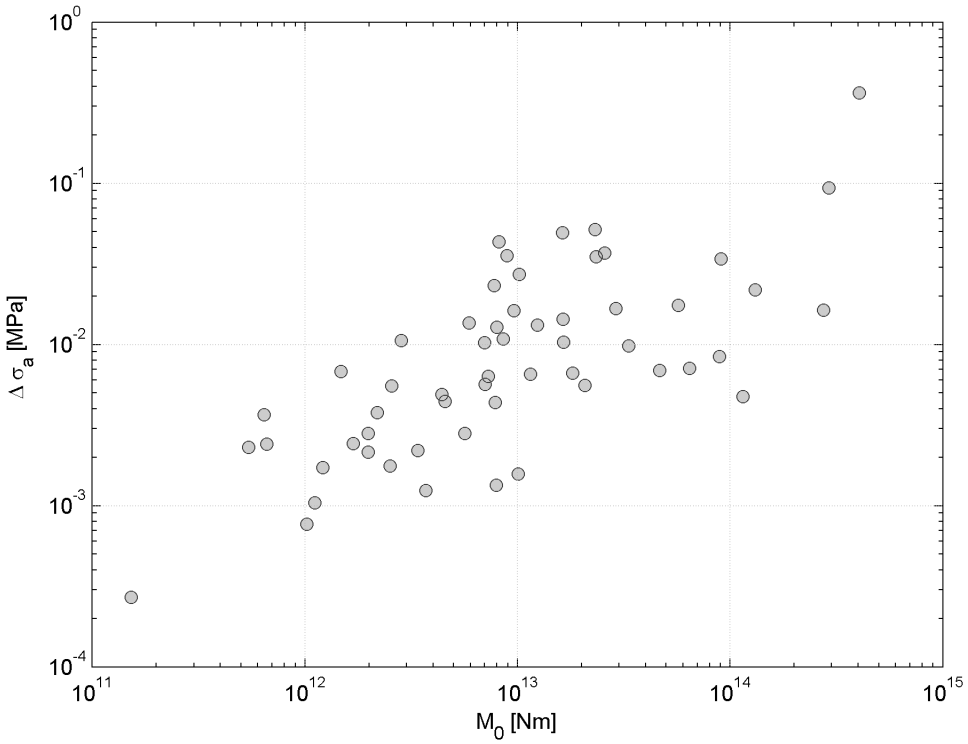

Figure 4.1: The dependence of the apparent stress $\Delta\sigma_a$ on the seismic moment M_0 (for P waves).

$$\log M_0 = 1.37\,\mathrm{M_L} + 10.4 \tag{4.1}$$

was obtained from the regression of the seismic moment M_0 in log scale and the local magnitude $\mathrm{M_L}$ (the correlation coefficient was 0.92). The obtained scaling factor of 1.37 is significantly smaller than 1.5 present in definition of the moment magnitude M_w that was derived for a constant stress drop (Kanamori, 1977), which gives an independent indication of the non-self-similarity of the analyzed swarm earthquakes. In Fig. 4.2 an empirical relation $\log M_0 = 1.05\,\mathrm{M_L} - 11.3$ obtained by Hainzl & Fischer (2002) from analysis of catalogue of the 2000 swarm in WB is also shown. The scaling factor 1.05 is even lower than received in this study but is similar to relation of Grosser et al. (1986); eq. (4.3).

With respect to ambiguous results from the relative and absolute approach it is highly disputable if it make sense to speak about estimates of the source parameters derived from the corner frequency, namely the stress drop $\Delta\sigma$ whose dependence on f_c is with third power (increase of f_c by 20 % leads to a doubling of the stress drop). In addition, the stress drop does not depend on f_c and M_0 only, but also on other parameters like the rupture velocity, which is assumed constant in this study. Therefore the stress drop values should be assumed valid in terms of orders only. However, the values of $\Delta\sigma$ are still high.

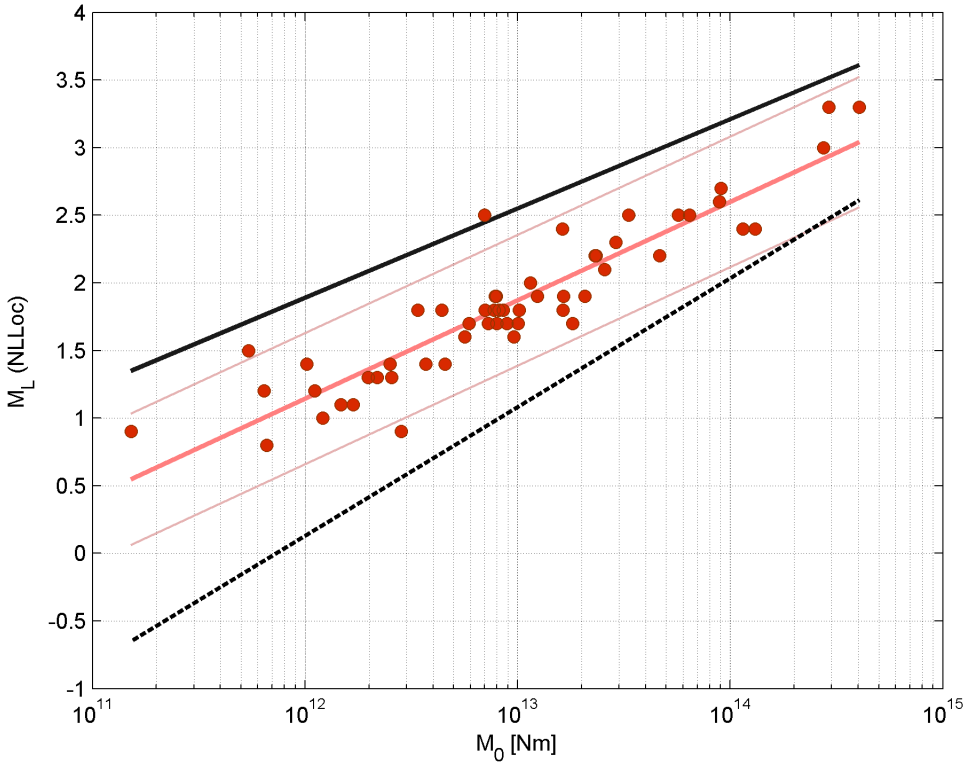

Figure 4.2: Linear regression between the local magnitude M_L and the seismic moment M_0 in log scale. The 95 % confidence interval is bounded by solid red lines. The relation for moment magnitude $M_w = 2/3 \log M_0 - 6.03$ (Hanks & Kanamori, 1979) is plotted by solid black line. Similar empirical relation for the local magnitude obtained by (Hainzl & Fischer, 2002) is plotted by the dashed black line.

4.4 Attenuation

The anelastic attenuation has significant effect to widening the pulses and decreasing the corner frequencies. This is corrected by the frequency dependent exponential term in equation (2.14) for which the knowledge of the Q-factor is essential. Because there is no independent estimate of the quality factor for the area of interest an event- and station-dependent Q was determined as a part of the inversion for f_c. The correction for the Q-factor accounts also for the near-surface attenuation that is expressed by a sharp decrease of the spectral amplitudes above f_{max} (Hanks, 1982). I did observe this type of decay in the spectra at some stations at frequencies above 60 Hz, which however does not overlap with the resulting corner frequencies ranging from 6 to 40 Hz. I thus infer that by limiting the analysis to the $M_L > 0.8$ events the near-surface attenuation does not affect the resolved corner frequencies. This is also manifested in Fig. 3.11 by the same scaling of f_c with M_0 for small and large events with no trend to leveling-off of f_c at small seismic moments.

Analyses of attenuation from other regions like Basel (Bethmann et al., 2012), Cajon Pass or Parkfield (Abercrombie, 1998) suggest very low Q-factors in the upper parts and at surface. Typical reported Q-values in these studies (either for P or S waves) are between 30 and 50 in the first hundreds of meters and are increasing with depth ($Q \sim 1000$ in Cajon Pass at 2.5 km; $Q \sim 85$ in Basel at 1.2 km and lower). Abercrombie (1998) suggests that the primary cause of severe near-surface attenuation is the opening of fractures with decreasing lithostatic pressure and that neglecting this attenuation can be one of the reasons for the proposed break- down in earthquake scaling at small magnitudes. Bethmann et al. (2012) also observed that Q increases with depth, but with values around 30 – 50 between 500 and 2700 m, which is low even for the consolidated Permian and Mesozoic sediments. Although the values of Q presented in this study are relatively high (with respect to usage of surface observations), one should keep in mind that our stations are hard-rock-based compared to the sedimentary-based stations in studies mentioned previously.

High values of Q were observed by Frankel (1982) in northeastern Caribbean where the average $Q_P = 380$ was obtained from 3 stations at epicentral distances 40-200 km. Godano et al. (2013) used even higher $Q = 800$ when they analyzed seismic source parameters of the swarm earthquakes in the Sampeyre region (Western Alps, Italy).

4.5 Comparison with results in other studies

4.5.1 West Bohemia/Vogtland region

The very first source parameters from the West Bohemia/Vogtland region were presented during the workshop in Mariánské Lázně (Czech Republic) just one year after the prominent 1985/86 earthquake swarm. There were presented three contributions regarding the source parameters estimation by Antonini (1986), Plešinger et al. (1986) and Grosser et al. (1986). The results are summarized in Tab. (4.1). Plešinger et al.

Authors	*Source radius* [m]	M_0 [Nm]	$\Delta\sigma$ [MPa]	M_L	*Num Sta*	*Num Ev*
Antonini (1986)	100 – 700	2e11 – 4e14	0.02 – 3	2.0 – 4.8	3	∼10
Plešinger et al. (1986)	130 – 650	–	–	0.7 – 4.2	3	∼ 42
Grosser et al. (1986)	80 – 600	5e11 – 3e14	0.1 – 1	1.4 – 4.1	1	24

Table 4.1: Source parameters of the 1985/86 earthquake swarm

(1986) observed almost identical P and S wave corner frequencies: 2 – 3 Hz (M_L3.9), 4 – 5 Hz, (M_L2.7), about 10 Hz (M_L1.9) and 20 – 30 Hz ($M_L <$ 1). Similarly Grosser et al. (1986) observed $f_c^P/f_c^S < 1.5$, which is lower than expected theoretical value (Madariaga, 1976). Grosser et al. (1986) observed $M_0^P/M_0^S \sim 1.5$, which is similar to results of this study. The relations between M_0 and M_L obtained either by Antonini (1986)

$$\log M_0 = 1.21\,M_L + 16.6 \tag{4.2}$$

or by Grosser et al. (1986)

$$\log M_0 = 1.01\,M_L + 10.42 \tag{4.3}$$

show even lower scaling than in this study and therefore further away from the constant stress drop assumption. The systematically lower corner frequencies obtained by Plešinger et al. (1986) could be caused by omission of the attenuation correction.

4.5.2 Worldwide

Comparison of relations between the corner frequency f_c and the seismic moment M_0, obtained by the absolute approach from P waves is given in Fig. 4.3. Here I would like to mention that M_0 and f_c are almost independent on the selected model of the source (only f_c is conditioned by the selected high-frequency fall off). Using the axis scaling as used in Fig. 4.3 the stress drop from this study seems to be almost constant over the whole dataset, just having higher values. It is worth noting that even though some of the results show decrease of the stress drop with the decreasing seismic moment (e.g. Urbancic & Young, 1993; Ide et al., 2003) the overall trend across all studies points to self-similarity of the earthquakes. It is still question whether the leveling-off of f_c with decreasing M_0 has a physical reason or it is just an artifact of the limited data or approach (limited bandwidth, attenuation, simplified model of the source). Keeping in mind the uncertainties of f_c and of $\Delta\sigma$ consequently only the trends are worthy of comparison.

The second, and probably the main, criterion for the earthquake self-similarity assessment is the effectivity of the radiated energy – the apparent stress $\Delta\sigma_a$. Figure 4.4 shows comparison of the apparent stress with results in other studies. The obvious decrease of $\Delta\sigma_a$ with decreasing M_0 is observed almost in all studies. It is interesting that this trend occurs almost in each separate study but as a whole $\Delta\sigma_a$ seems to be within a band of "constant" values. Again, it is a question whether the weaker events really radiate less energy or if it is a consequence of a hidden artifact.

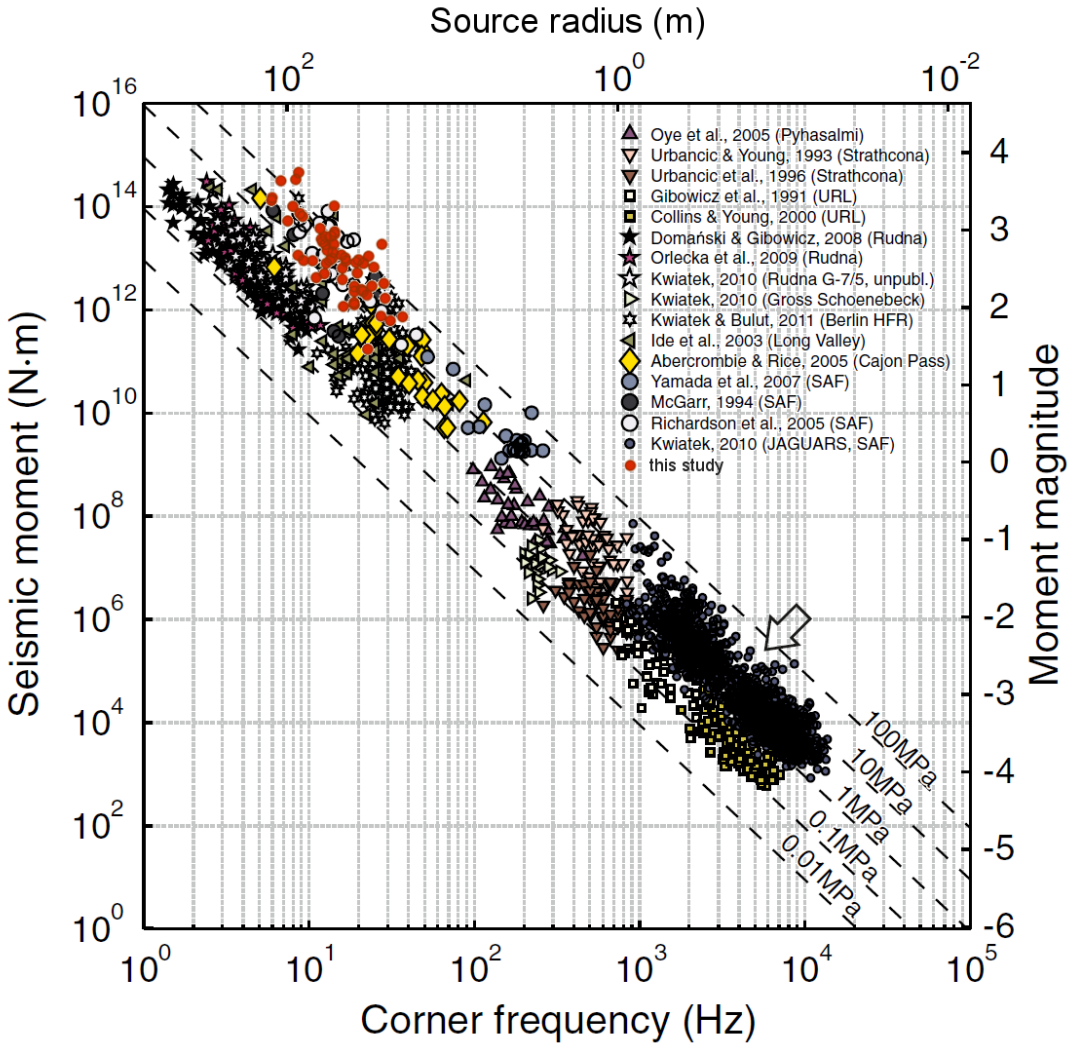

Figure 4.3: Comparison of f_c and M_0 obtained from analysis of P waves (red circles) with other results (adopted from Kwiatek et al., 2011).

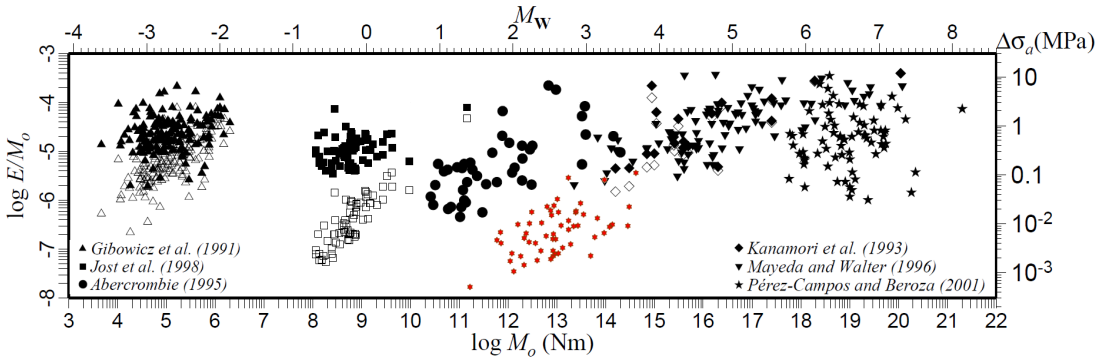

Figure 4.4: Comparison of scaled energy with other studies (adopted from Ide & Beroza, 2001).

Chapter 5

Conclusions

I studied source parameters of the West Bohemia/Vogtland earthquake swarms 2000 and 2008 in the frequency domain and analyzed 56 events in the magnitude range M_L from 0.8 to 3.3 that were evenly distributed along the fault plane. Direct P waves and S waves from 3 to 21 stations at epicentral distances from 0 to 30 km were used. I applied the absolute and relative approach to invert for source parameters. The absolute approach allowed to retrieve the seismic moment M_0 and corner frequency f_c and was applied to P waves (inversion of individual events and the joint inversion of all events together) and to S waves (inversion of individual events only). The relative approach was applied with aim to obtain more precise corner frequency by separation of the source from the material-dependent attenuation. The inversion of S waves, the joint inversion and the relative approach was applied to a subset of 24 events only from the 2008 earthquake swarm because of much better focal sphere coverage by stations than in 2000. From the absolute approach I obtained the quality factor Q as a byproduct. In all approaches the same Brune's circular model of the source with ω^{-2} high-frequency falloff was used with assumptions of a quasidynamic behavior after Madariaga (1976). The main conclusions can be summarized as follows:

- The corner frequencies of the M_L 0.8–3.3 events range from 6 to 40 Hz, which corresponds to the rupture radii in the range 28 to 150 m for seismic moments from 1.5e11 to 4e14 Nm.

- To verify the precision of M_0 obtained from the absolute approach and to test the influence of the radiation pattern correction I evaluated M_0 by the AMT method. The radiation pattern correction influences mainly estimates at stations close to the nodal lines of the focal mechanisms. However, even if only the mean radiation pattern correction is applied the absolute and AMT methods give similar results; differences of 0.3 in the log scale which correspond to usual uncertainties of M_L.

- An alternative method of Snoke was applied to P waves to determine the radiated energy $E(J)$ and the corner frequency $f_c(J)$ from the integral of the velocity squared spectra J. This method gave very similar f_c as obtained from the absolute inversion if the correction for attenuation is applied. This good fit qualifies the

more simple Snoke's method to be applicable for routine determination of the static source parameters of small earthquakes in case that the quality factor Q is known and applied.

- The absolute joint inversion for f_c and Q over 24 events and all available stations simultaneously for P waves resulted in Q-factor between 117 and 400 at different stations.The Q from the joint inversion is more stable than from inversion of individual events.

- Comparison of methods for inversion of f_c is in favor of the absolute methods compared to the relative ones. Even though the relative methods should separate the source term effectively the uncertainty of this methods is higher. Especially the joint absolute inversion allows to estimate the uncertainties of f_c more reliably.

- Comparison of results of the absolute methods applied to P and S waves gives: f_c^{α}/f_c^{β} is most often between 1.0 and 1.5; median of Q_S/Q_P ratios is 1.32 instead of expected 0.4; the ratio $M_0^P/M_0^S = 1.51$ would need $\alpha/\beta = 1.9$ which is unrealistically high. Explanation is not provided but results are similar to other studies.

- Scaling of f_c with M_0 shows an exponent of -0.202, which in the absolute sense is smaller than -0.33 that is expected for the constant stress drop model. The stress drops $\Delta\sigma$ range between 0.7 to 138 MPa with tendency to a higher stress drops for the larger events. But taking into account the high uncertainty of $\Delta\sigma$ (which is still very likely underestimated) these values should not be used for any further interpretations.

- Apparent stress $\Delta\sigma_a$ ranges over three orders from 0.3 kPa to 0.4 MPa, which supports finding that the West–Bohemia swarm earthquakes are not self-similar.

The simple model of the source can never adopt all the aspects of the real source and the values represent a very rough estimates in terms of orders only. Comparison between similar individual studies even using the same source model can differ in the absolute sense because of the different numerical implementation and the specific signal operations. Application of either absolute or relative spectral methods for estimation of the source parameters of microearthquakes or weak earthquakes generally must be done with knowledge of the possible uncertainties. Interpretation of the results must be always done with respect to the used model of the source.

Chapter 6

Included papers

P1: Fischer, T. and Michálek, J. (2008). Post 2000-swarm microearthquake activity in the principal focal zone of West Bohemia/Vogtland: Space-time distribution and waveform similarity analysis. *Stud. Geophys. Geod.* 52, 493–511. DOI: 10.1007/s11200-008-0034-y

P2: Michálek, J. and Fischer, T. (2013). Source parameters of the swarm earthquakes in West Bohemia/Vogtland. *Geophys. J. Int.* 195, 1196–1210. DOI: 10.1093/gji/ggt286

Appendix A

Implementation of evaluation of the source parameters into SEISMON

SEISMON is a GUI MATLAB software initially developed by Stefan Mertl, TU in Vienna (Mertl & Hausmann, 2009). I joined the SEISMON project development in 2010 and since then the code is developed and modified (Michálek et al., 2011; Doubravová et al., 2012; Doubravová & Horálek, 2013) by team of people at Seismological Department of Institute of Geophysics AS CR for processing of data mainly from the WEBNET seismic network. The code is sheared via the Apache Subversion system (SVN) which allows simultaneous implementation of the code changes. Due to the specific needs of routine processing the functionality was extended and new automated tools were added. As a result of changes a new branch SEISMON_WB (WEBNET version) was created.

SEISMON uses a MySQL database for storage of all information regarding the network geometry, sensor configuration, parameters of digitizers, metadata from waveforms and of course all important results of the analysis performed. The organization of data is project based and each project can be shared by more users via network, i.e. results are stored in one place for all users.

In the frame of my grant project *Source parameters of microearthquakes in West Bohemia and South Iceland* (grant No. 171310; 2010-2012) supported by the Charles University Grant Agency a new tool was developed for estimation of the source parameters in the frequency domain. Aim of the project was to develop and test a tool for estimation of seismic source parameters and apply the procedure to earthquakes from West Bohemia and South Iceland. The tool should be simple and robust to be applied routinely.

A.1 Parts of SEISMON

A.1.1 Trace Display

The main window is called Trace Display A.1 and serves for basic processing of the data – viewing, signal modification, transformations, picking of wave arrivals, running location algorithms, etc. In this window some tools for special analysis are available

and one of them is for the source parameter estimation. To run the source parameter analysis some previous operations must be done, i.e. location and amplitude moment tensor inversion (AMT; Vavryčuk et al., 2013) which computes the ray tracing in 1D velocity model (Málek et al., 2000) for more precise calculation of attenuation due to geometrical spreading. Results of these steps are stored in the database.

A.1.2 Tool for source parameter estimation

The new tool allows to apply the absolute inversion of source parameters to individual events. The analysis can be performed for P or S waves. The difference is only in window time-length and the input data. For P waves 1.0 sec window from Z component is used whereas for S waves the 1.5 sec window from N and E components is applied. In both cases the first 0.5 sec of signal is used for calculating the noise spectra. For analysis of S waves the spectra from horizontal components are averaged (this can be done for the near-vertical incidence angles only). Figure A.2 shows an example of the P-wave analysis at four stations individually.

Setting of the inversion parameters

The specific parameters of the fitted source model can be selected/changed via the GUI dialog window (Fig. A.3; keyboard shortcut *Ctrl+E*). The first box *Model Type* allows to quickly select the predefined set of parameters for two typical source models - *Brune* and *Boatwright*. Third option *custom* allows to change all the values independently. There is a box *Equation* with the source model equation which helps to orient user in the edited quantities. The box *Attenuation* allows to set up the initial values of attenuation and also allows to specify the time which will be used in inversion or to set up fixed propagation time (e.g. for analysis at one station). The box *Parameters to fit* serves for specification of what parameters will be fitted during the inversion and what parameters will be fixed to predefined value. The parameter Ω_0 is never fitted, corner frequency f_c is fitted always. The last box *Optimization* allows to select what norm of the residual function will be minimized (*Norm*) and if the *Sum of residuals* will be evaluated in *linear* or *log* scale. After confirmation of the dialog window by pressing *OK* the inversion is started. The inversion is performed at each station individually (as in Fig. A.2) and also simultaneously as a joint inversion for one common f_c at all stations with independent value of Q at each station. Results of the individual inversions are shown in the figure with spectra (Fig. A.2), including the best fitted source model curve and are also shown in table in an extra window (if selected in options before). Results of the joint inversion are showed in the MATLAB command window. If *Plot evolution of fitted parameters* was checked, also the trade-offs between the fitted parameters are plotted in individual special windows.

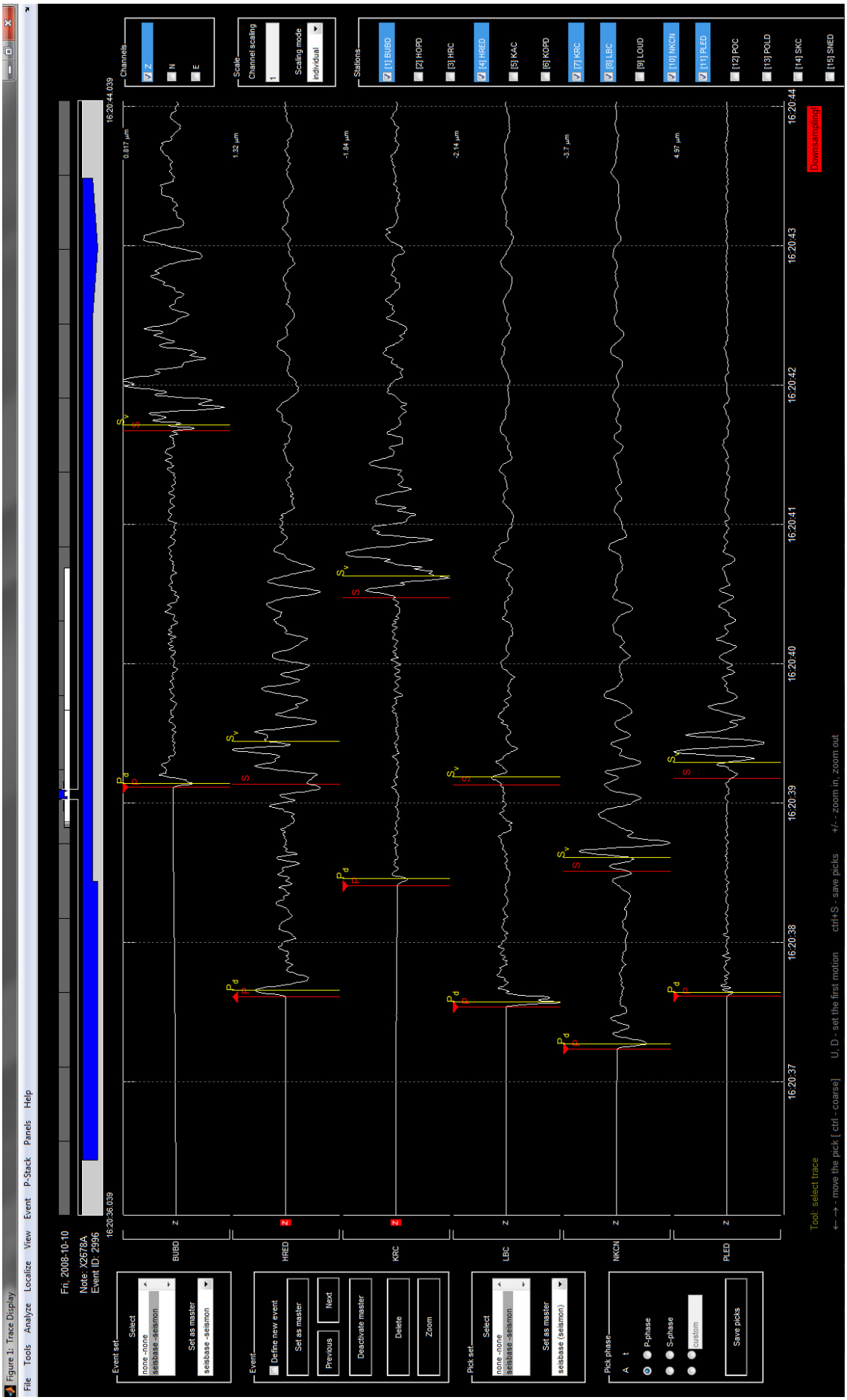

Figure A.1: Seismon Trace Display window. Example of event X2678A, Z components of displacement at selected stations. Arrival times of P and S phases are marked by red vertical lines.

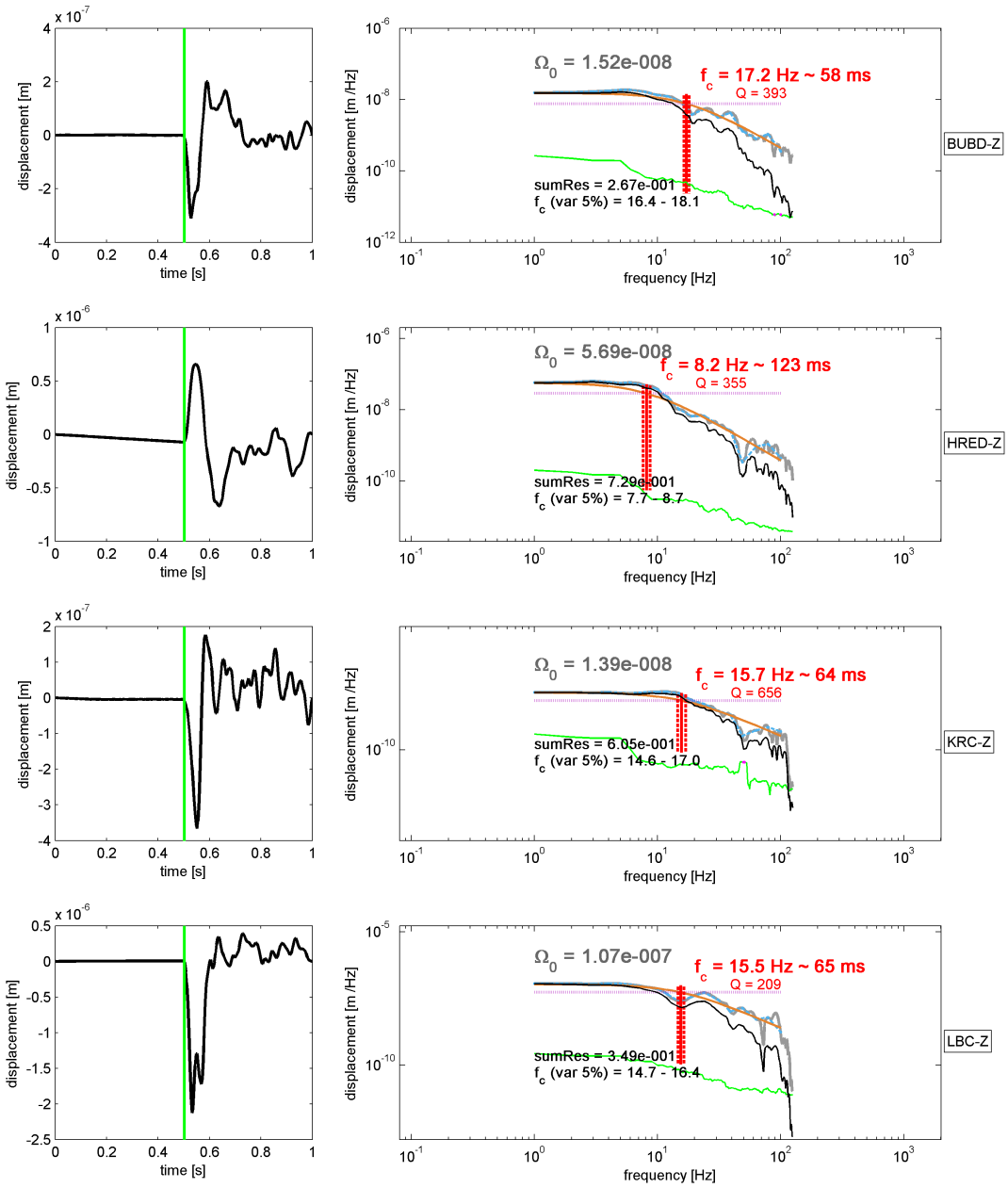

Figure A.2: Spectral analysis. Example of absolute source parameter inversion from P-wave displacement (left) at four stations. Results of inversion at individual stations are written in spectra (right) in red color.

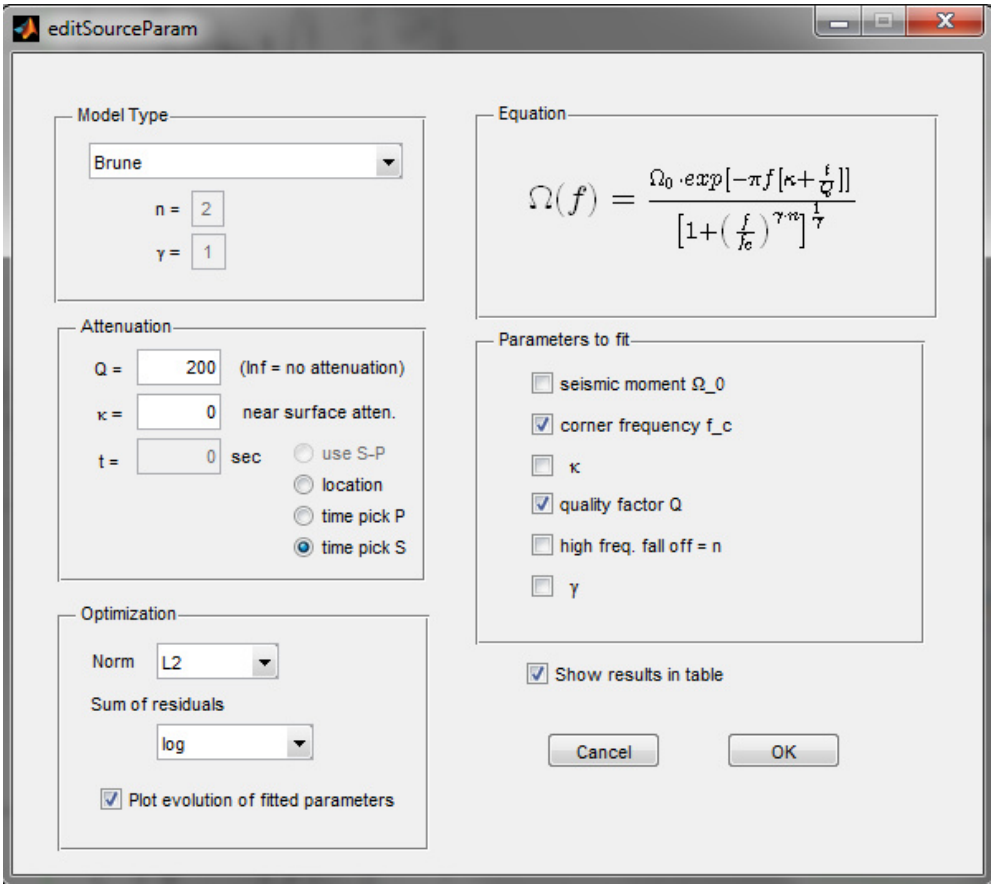

Figure A.3: GUI window for setting of inversion parameters (description in text).

References

Abercrombie, R. E., 1995. Earthquake source scaling relationships from -1 to 5 ML using seismograms recorded at 2.5-km depth, *J. Geophys. Res.*, **100**(B12), 24015–24036.

Abercrombie, R. E., 1998. A Summary of Attenuation Measurements from Borehole Recordings of Earthquakes: The 10 Hz Transition Problem, *Pure Appl. Geophys.*, **153**(4), 475.

Abercrombie, R. E. & Rice, J. R., 2005. Can observations of earthquake scaling constrain slip weakening?, *Geophys. J. Int.*, **162**(2), 406–424.

Aki, K., 1967. Scaling law of seismic spectrum, *J. Geophys. Res.*, **72**(4), 1217–1231.

Aki, K. & Richards, P. G., 2002. *Quantitative Seismology*, vol. II, University Science Books.

Allmann, B. P. & Shearer, P. M., 2007. Spatial and temporal stress drop variations in small earthquakes near Parkfield, California, *J. Geophys. Res.*, **112**(B4), 1–17.

Ammon, C. J., Velasco, A. A., & Lay, T., 1993. Rapid estimation of rupture directivity: Application to the 1992 Landers (Ms = 7.4) and Cape Mendocino (Ms = 7.2), California earthquakes, *Geophys. Res. Lett.*, **20**(2), 97–100.

Andrews, D. J., 1986. Objective determination of source parameters and similarity of earthquakes of different size, *Geophys. Monogr. Ser.*, **37**, 259–267.

Antonini, M., 1986. Statistics and source parameters of the swarm from digital recordings, in *Earthq. Swarm 1985/86 West. Bohemia*, pp. 205–217, Institute of Geophysics, ASCR, Mariánské Lázně, Czech republic.

Babuška, V. & Plomerová, J., 2008. Control of paths of Quaternary volcanic products in western Bohemian Massif by rejuvenated Variscan triple junction of ancient microplates, *Stud. Geophys. Geod.*, **52**, 607–630.

Baltay, A. S., Prieto, G., & Beroza, G. C., 2010. Radiated seismic energy from coda measurements and no scaling in apparent stress with seismic moment, *J. Geophys. Res.*, **115**(B8), 1–12.

Baltay, A. S., Ide, S., Prieto, G., & Beroza, G., 2011. Variability in earthquake stress drop and apparent stress, *Geophys. Res. Lett.*, **38**.

Bankwitz, P., Schneider, G., Kämpf, H., & Bankwitz, E., 2003. Structural characteristics of epicentral areas in Central Europe: study case Cheb Basin (Czech Republic), *J. Geodyn.*, **35**, 5–32.

Bennington, N., Thurber, C., & Roecker, S., 2008. Three-Dimensional Seismic Attenuation Structure around the SAFOD Site, Parkfield, California, *Bull. Seismol. Soc. Am.*, **98**(6), 2934–2947.

Bethmann, F., Deichmann, N., & Mai, P. M., 2012. Seismic wave attenuation from borehole and surface records in the top 2.5 km beneath the city of Basel, Switzerland, *Geophys. J. Int.*, **190**(2), 1257–1270.

Boatwright, J., 1980. A spectral theory for circular seismic sources; simple estimates of source dimension, dynamic stress drop, and radiated seismic energy, *Bull. Seismol. Soc. Am.*, **70**(1), 1–27.

Boatwright, J., 1984. Seismic estimates of stress release, *J. Geophys. Res.*, **89**(B8), 6961.

Boore, D. M. & Boatwright, J., 1984. Average body-wave radiation coefficients, *Bull. Seismol. Soc. Am.*, **74**(5), 1615–1621.

Bräuer, K., Kämpf, H., Koch, U., & Strauch, G., 2011. Monitoring of gas and isotope compositions in the free gas phase at degassing locations close to the Nový Kostel focal zone in the western Eger Rift Czech Republic, *Chem. Geol.*, **290**(3-4), 163–176.

Brune, J., 1970. Tectonic stress and the spectra of seismic shear waves from earthquakes, *J. Geophys. Res.*, **75**(26), 4997–5009.

Burdick, L. J., 1978. t* for S waves with a continental ray path, *Bull. Seismol. Soc. Am.*, **68**(4), 1013–1030.

Cerveny, V., 2005. *Seismic ray theory*, Cambridge University Press.

Dahm, T., Fischer, T., & Hainzl, S., 2008. Mechanical intrusion models and their implications for the possibility of magma-driven swarms in NW Bohemia Region, *Stud. Geophys. Geod.*, **52**(4), 529–548.

Dobrynina, A. A., 2009. Source parameters of the earthquakes of the Baikal rift system, *Izv. Phys. Solid Earth*, **45**(12), 1093–1109.

Doubravová, J. & Horálek, J., 2013. New interactive software for seismic data processing, in *Tech. Comput. Prague 2013*, p. 393, HUMUSOFT.

Doubravová, J., Michálek, J., & Horálek, J., 2012. Seismon_WB - an interactive software for routine processing of local seismic data, in *33rd Eur. Seismol. Comm. Gen. Assem.*, ESC, Moscow.

Edwards, B. & Rietbrock, A., 2009. A Comparative Study on Attenuation and Source-Scaling Relations in the Kanto, Tokai, and Chubu Regions of Japan, Using Data from Hi-Net and KiK-Net, *Bull. Seism. Soc. Am.*, **99**(4), 2435–2460.

Eshelby, J., 1957. The determination of the elastic field of an ellipsoidal inclusion, and related problems, in *Proc. R. Soc. London*, pp. 376–396.

Fischer, T., 2005. Modelling of multiple events using empirical Green's functions: method, application to swarm earthquakes and implications for their rupture propagation, *Geophys. J. Int.*, **163**(3), 991–1005.

Fischer, T. & Horálek, J., 2003. Space-time distribution of earthquake swarms in the principal focal zone of the NW Bohemia/Vogtland seismoactive region: period 1985-2001, *J. Geodyn.*, **35**(1-2), 125–144.

Fischer, T. & Horálek, J., 2005. Slip-generated patterns of swarm microearthquakes from West Bohemia/Vogtland (central Europe): Evidence of their triggering mechanism?, *J. Geophys. Res.*, **110**(B5), 1–14.

Fischer, T. & Michálek, J., 2008. Post 2000-swarm microearthquake activity in the principal focal zone of West Bohemia/Vogtland: Space-time distribution and waveform similarity analysis, *Stud. Geophys. Geod.*, **52**(4), 493–512.

Fischer, T., Horálek, J., Michálek, J., & Boušková, A., 2010. The 2008 West Bohemia earthquake swarm in the light of the WEBNET network, *J. Seismol.*, **14**(4), 665–682.

Frankel, A., 1982. The effects of attenuation and site response on the spectra of microearthquakes in the northeastern Caribbean, *Bull. Seismol. Soc. Am.*, **72**(4).

Furuya, I., 1969. Predominant Period and Magnitude, *J. Phys. Earth*, **17**(2), 119–126.

Futterman, W., 1962. Dispersive body waves, *J. Geophys. Res.*, **67**(13), 5279–5291.

García-García, J. M., Vidal, E., Romacho, M. D., Martín-Marfil, J. M., Posadas, A., & Luzón, F., 1996. Seismic source parameters for microearthquakes of the Granada basin (southern Spain), *Tectonophysics*, **261**, 51–66.

Gibowicz, S. & Kijko, A., 1994. *An introduction to mining seismology*, Academic Press, Inc., San Diego.

Godano, M., Larroque, C., Bertrand, E., Courboulex, F., Deschamps, A., Salichon, J., Blaud-Guerry, C., Fourteau, L., Charléty, J., & Deshayes, P., 2013. The October-November 2010 earthquake swarm near Sampeyre (Piedmont region, Italy): A complex multicluster sequence, *Tectonophysics*, **608**, 97–111.

Grosser, H. P., Burghardt, P. J., & Köhler, W. P., 1986. Spectral calculations and focal parameter studies of selected events of the West Bohemia earthquake swarm 1985/1986, in *Earthq. Swarm 1985/86 West. Bohemia*, pp. 282–292, Institute of Geophysics, ASCR, Mariánské Lázně, Czech republic.

Hainzl, S. & Fischer, T., 2002. Indications for a successively triggered rupture growth underlying the 2000 earthquake swarm in Vogtland/NW Bohemia, *J. Geophys. Res.*, **107**(B12), 1–9.

Hainzl, S. & Ogata, Y., 2005. Detecting fluid signals in seismicity data through statistical earthquake modeling, *J. Geophys. Res. Solid Earth*, **110**(B5).

Hainzl, S., Fischer, T., & Dahm, T., 2012. Seismicity-based estimation of the driving fluid pressure in the case of swarm activity in Western Bohemia, *Geophys. J. Int.*, **191**(1), 271–281.

Hanks, T., 1982. fmax, *Bull. Seismol. Soc. Am.*, **72**(6), 1867–1879.

Hanks, T. C. & Kanamori, H., 1979. A moment magnitude scale, *J. Geophys. Res.*, **84**(9), 2348–2350.

Hanks, T. C. & Thatcher, W., 1972. A graphical representation of seismic source parameters, *J. Geophys. Res.*, **77**, 4393–4405.

Harrington, R. M. & Brodsky, E. E., 2009. Source Duration Scales with Magnitude Differently for Earthquakes on the San Andreas Fault and on Secondary Faults in Parkfield, California, *Bull. Seismol. Soc. Am.*, **99**(4), 2323–2334.

Hartzell, S. H., 1978. Earthquake aftershocks as Green's functions, *Geophys. Res. Lett.*, **5**(1), 1–4.

Haskell, N., 1964. Total energy and energy spectral density of elastic wave radiation from propagating faults, *Bull. Seismol. Soc. Am.*, **54**(6), 1811–1841.

Hauksson, E. & Shearer, P. M., 2006. Attenuation models (Q P and Q S) in three dimensions of the southern California crust: Inferred fluid saturation at seismogenic depths, *J. Geophys. Res.*, **111**(B5), 1–21.

Horálek, J. & Fischer, T., 2008. Role of crustal fluids in triggering the West Bohemia/Vogtland earthquake swarms: just what we know (a review), *Stud. Geophys. Geod.*, **52**, 455–478.

Horálek, J. & Fischer, T., 2010. Intraplate earthquake swarms in West Bohemia/Vogtland (Central Europe), *Jökull*, (60), 67–87.

Horálek, J. & Šílený, J., 2013. Source mechanisms of the 2000 earthquake swarm in the West Bohemia/Vogtland region (Central Europe), *Geophys. J. Int.*, **194**(2), 979–999.

Horalek, J., Sileny, J., & Fischer, T., 2002. Moment tensors of the January 1997 earthquake swarm in NW Bohemia (Czech Republic): double-couple vs. non-double-couple events, *Tectonophysics*, **356**, 65–85.

Ide, S. & Beroza, G., 2001. Does apparent stress vary with earthquake size?, *Geophys. Res. Lett.*, **28**(17), 3349–3352.

Ide, S., Beroza, G., Prejean, S., & Ellsworth, W., 2003. Apparent break in earthquake scaling due to path and site effects on deep borehole recordings, *J. Geophys. Res.*, **108**(B5), 2271.

Imanishi, K., Takeo, M., Ellsworth, W. L., Ito, H., Matsuzawa, T., Kuwahara, Y., Iio, Y., Horiuchi, S., & Ohmi, S., 2004. Source parameters and rupture velocities of microearthquakes in Western Nagano, Japan, determined using stopping phases, *Bull. Seismol. Soc. Am.*, **94**(5), 1762–1780.

Jost, M. & Herrmann, R. B., 1989. A student's guide to and review of moment tensors, *Seismol. Res. Lett.*, **60**(2), 37–57.

Kanamori, H., 1977. The Energy Release in Great Earthquakes, *J. Geophys. Res.*, **82**(20), 2981–2987.

Kanamori, H. & Anderson, D., 1975. Theoretical basis of some empirical relations in seismology, *Bull. Seismol. Soc. Am.*, **65**(5), 1073–1095.

Kane, D. L., Prieto, G. a., Vernon, F. L., & Shearer, P. M., 2011. Quantifying Seismic Source Parameter Uncertainties, *Bull. Seismol. Soc. Am.*, **101**(2), 535–543.

Kolar, P. & Ruzek, B., 2012. Finite seismic source parameters inferred from stopping phases for selected events of West Bohemia 2000 swarm, *Acta Geodyn. Geomater.*, **9**(4), 435–447.

Kostrov, B. & Das, S., 1988. *Principles of earthquake source mechanics*, Cambridge University Press.

Kwiatek, G., Plenkers, K., Dresen, G., & JAGUARS Research Group, 2011. Source Parameters of Picoseismicity Recorded at Mponeng Deep Gold Mine, South Africa: Implications for Scaling Relations, *Bull. Seismol. Soc. Am.*, **101**(6), 2592–2608.

Lay, T. & Wallace, T. C., 1995. *Modern Global Seismology*, Academic Press, Inc.

Lindley, G. & Archuleta, R., 1992. Earthquake source parameters and the frequency dependence of attenuation at Coalinga, Mammoth Lakes, and the Santa Cruz Mountains, California, *J. Geophys. Res.*, **97**(B10), 14137–14154.

Madariaga, R., 1976. Dynamics of an expanding circular fault, *Bull. Seismol. Soc. Am.*, **66**(3), 639–666.

Madariaga, R., 1983. Earthquake source theory: a review, in *Earthquakes Obs. Theory Interpret.*, pp. 1–44, eds Kanamori, H. & Boschi, E., North Holland Publishing Company, Amsterdam.

Madariaga, R., 2011. Earthquakes, Source Theory, in *Encycl. Solid Earth Geophys.*, Encyclopedia of Earth Sciences Series, pp. 248–252, ed. Gupta, H. K., Springer Netherlands, Dordrecht.

Málek, J., Janský, J., & Horálek, J., 2000. Layered velocity models of the western Bohemia region, *Stud. Geophys. Geod.*, **44**, 475–490.

Mayeda, K., Gök, R., Walter, W. R., & Hofstetter, A., 2005. Evidence for non-constant energy/moment scaling from coda-derived source spectra, *Geophys. Res. Lett.*, **32**(L10306).

Mertl, S. & Hausmann, H., 2009. Seismon - a flexible seismic processing software, *Geophys. Res. Abstr.*, **11**, 4266.

Michálek, J. & Fischer, T., 2013. Source parameters of the swarm earthquakes in West Bohemia/Vogtland, *Geophys. J. Int.*, **195**(2), 1196–1210.

Michálek, J., Doubravová, J., & Mertl, S., 2011. Usage of SEISMON within the WEBNET seismic network, in *Geophys. Res. Abstr.*, vol. 13, p. 6264.

Molnar, P., Tucker, B., & Brune, J., 1973. Corner frequencies of P and S waves and models of earthquake sources, *Bull. Seismol. Soc. Am.*, **63**, 2091–2104.

Mori, J. & Frankel, A., 1990. Source parameters for small events associated with the 1986 North Palm Springs, California, earthquake determined using empirical Green functions, *Bull. Seismol. Soc. Am.*, **80**(2), 278–295.

Moyer, P., Boettcher, M., Mcguire, J., & Collins, J., 2012. Radiated energy of $3.0 < M < 5.0$ earthquakes in rupture patches and rupture barriers on Gofar Transform Fault, East Pacific Rise, in *ECGS 2012*, ECGS Workshop 2012: Earthquake source physics on various scales, Luxembourg.

Mrlina, J., Kämpf, H., Kroner, C., Mingram, J., Stebich, M., Brauer, A., Geissler, W., Kallmeyer, J., Matthes, H., & Seidl, M., 2009. Discovery of the first Quaternary maar in the Bohemian Massif, Central Europe, based on combined geophysical and geological surveys, *J. Volcanol. Geotherm. Res.*, **182**(1-2), 97–112.

Mueller, C. S., 1985. Source pulse enhancement by deconvolution of an empirical Green's function, *Geophys. Res. Lett.*, **12**(1), 33–36.

Müller, G., 1983. Rheological properties and velocity dispersion of a medium with power-law dependence of Q on frequency, *J. Geophys*, **54**, 20–29.

Oth, A., Bindi, D., Parolai, S., & Di Giacomo, D., 2010. Earthquake scaling characteristics and the scale-(in)dependence of seismic energy-to-moment ratio: Insights from KiK-net data in Japan, *Geophys. Res. Lett.*, **37**(19), 1–5.

Oth, A., Bindi, D., Parolai, S., & Di Giacomo, D., 2011. Spectral Analysis of K-NET and KiK-net Data in Japan, Part II: On Attenuation Characteristics, Source Spectra, and Site Response of Borehole and Surface Stations, *Bull. Seismol. Soc. Am.*, **101**(2), 667–687.

Oye, V., Bungum, H., & Roth, M., 2005. Source parameters and scaling relations for mining-related seismicity within the Pyhäsalmi ore mine, Finland, *Bull. Seismol. Soc. Am.*, **95**(3), 1011–1026.

Plešinger, A., Horálek, J., Vavryčuk, V., Pšenčík, I., & Zedník, J., 1986. Complex Analysis of Local Digital observations of the 1985/86 West-Bohemian earthquake swarm: preliminary results, in *Earthq. Swarm 1985/86 West. Bohemia*, pp. 343–356, Institute of Geophysics, ASCR, Mariánské Lázně, Czech republic.

Plicka, V., Sokos, E., Tselentis, G., & Zahradník, J., 1998. The Patras earthquake (14 July 1993): relative roles of source, path and site effects, *J. Seismol.*, **2**(4), 337–349.

Prieto, G. A., Shearer, P. M., Vernon, F. L., & Kilb, D., 2004. Earthquake source scaling and self-similarity estimation from stacking P and S spectra, *J. Geophys. Res.*, **109**(B8), 1–13.

Sato, T. & Hirasawa, T., 1973. Body wave spectra from propagating shear cracks, *J. Phys. Earth*, **21**(4), 415–431.

Savage, J. C., 1966. Radiation from a realistic model of faulting, *Bull. Seismol. Soc. Am.*, **56**(2), 577–592.

Savage, J. C., 1972. Relation of corner frequency to fault dimensions, *J. Geophys. Res.*, **77**(20), 3788–3795.

Shearer, P. M., 2009. *Introduction to Seismology*, no. 5, Cambridge University Press.

Shearer, P. M., Prieto, G. A., & Hauksson, E., 2006. Comprehensive analysis of earthquake source spectra in southern California, *J. Geophys. Res.*, **111**(B6), 1–21.

Shi, J., Kim, W., & Richards, P., 1998. The corner frequencies and stress drops of intraplate earthquakes in the northeastern United States, *Bull. Seismol. Soc. Am.*, **88**(2), 531–542.

Silver, P. G. & Jordan, T. H., 1982. Optimal estimation of scalar seismic moment, *Geophys. J. R. Astron. Soc.*, **70**(3), 755–787.

Sipkin, S. & Jordan, T., 1979. Frequency dependence of QScS, *Bull. Seismol. Soc. Am.*, **69**(4), 1055–1079.

Snoke, J., 1987. Stable determination of (Brune) stress drops, *Bull. Seismol. Soc. Am.*, **77**(2), 530–538.

Stein, S. & Wysession, M., 2003. *An Introduction to Seismology, Earthquakes, and Earth Structure*, vol. 56, Blackwell Publishing.

Toksöz, M. N., Johnston, D. H., & Timur, A., 1979. Attenuation of seismic waves in dry and saturated rocks: I. Laboratory measurements, *Geophysics*, **44**(4), 681–690.

Urbancic, T. & Young, R., 1993. Space-time variations in source parameters of mining-induced seismic events with M<0, *Bull. Seismol. Soc. Am.*, **83**(2), 378–397.

USGS, 2002. Shuttle radar topography mission (SRTM) finished grade data 3-ARC.

Vavryčuk, V., 2002. Non-double-couple earthquakes of 1997 January in West Bohemia, Czech Republic: evidence of tensile faulting, *Geophys. J. Int.*, **149**(2), 364–373.

Vavryčuk, V., 2011a. Principal earthquakes: Theory and observations from the 2008 West Bohemia swarm, *Earth Planet. Sci. Lett.*, **305**(3-4), 290–296.

Vavryčuk, V., 2011b. Tensile earthquakes: Theory, modeling, and inversion, *J. Geophys. Res.*, **116**(B12), B12320.

Vavryčuk, V., Bouchaala, F., & Fischer, T., 2013. High-resolution fault image from accurate locations and focal mechanisms of the 2008 swarm earthquakes in West Bohemia, Czech Republic, *Tectonophysics*, **590**, 189–195.

Viegas, G., Abercrombie, R. E., & Kim, W.-Y., 2010. The 2002 M5 Au Sable Forks, NY, earthquake sequence: Source scaling relationships and energy budget, *J. Geophys. Res.*, **115**(B7), 1–20.

Špičák, A. & Horálek, J., 2001. Possible role of fluids in the process of earthquake swarm generation in the West Bohemia/Vogtland seismoactive region, *Tectonophysics*, **336**(1-4), 151–161.

Waldhauser, F. & Ellsworth, W., 2000. A double-difference earthquake location algorithm: method and application to the northern Hayward fault, California, *Bull. Seismol. Soc. Am.*, **90**(6), 1353–1368.

Wegener, A., 1966. *The Origin of Continents and Oceans*, Dover Publications.

Wen, Y.-Y., 2014. Rupture behaviors of the 2011 Tohoku earthquake and its strongest foreshock through an empirical Green's function deconvolution analysis, *J. Asian Earth Sci.*, **81**, 123–128.

Yamada, T., Mori, J. J., Ide, S., Abercrombie, R. E., Kawakata, H., Nakatani, M., Iio, Y., & Ogasawara, H., 2007. Stress drops and radiated seismic energies of microearthquakes in a South African gold mine, *J. Geophys. Res.*, **112**(B3), 1–12.

List of Tables

List of abbreviations

AMT	amplitude moment tensor
EGF	empiric Green's function
FFT	fast Fourier transform
MTT	multitaper spectral estimate
PCM	Lennartz PCM 5800 recording system
RP	radiation pattern
SAFOD	San Andreas Fault Observatory at Depth
SEISMON	software for SEISmic MONitoring and analysis
STF	source time function
WB	West Bohemia
WEBNET	West Bohemia seismic network

POST 2000-SWARM MICROEARTHQUAKE ACTIVITY IN THE PRINCIPAL FOCAL ZONE OF WEST BOHEMIA/VOGTLAND: SPACE-TIME DISTRIBUTION AND WAVEFORM SIMILARITY ANALYSIS

T. FISCHER[1,2] AND J. MICHÁLEK[1]

1 Institute of Geophysics, Acad. Sci. Czech Republic, Boční II/1401, 141 31 Praha 4, Czech Republic (tomfis@ig.cas.cz)

2 Institute of Hydrogeology, Engineering Geology and Applied Geophysics, Faculty of Science, Charles University in Prague, Albertov 6, 128 43 Praha 2, Czech Republic

Received: January 25, 2008; Revised: June 6, 2008; Accepted: September 1, 2008

ABSTRACT

We present the pattern of seismic activity in the period between 2001 and 2007 for the Nový Kostel focal zone, which is recently the most active zone of the West-Bohemia/Vogtland earthquake swarm region. While the year 2001 was characterized by dying out of the 2000-swarm activity in the form of a few microswarms, almost no seismicity occurred in the period between 2002 and 2003. Since 2004 an elevated seismic activity occurs in the form of repeating microearthquake swarms. We used a relative location method to relate the hypocenter positions of the post-swarm activity to the geometry of the 2000-swarm cluster. We found that the activity has concentrated in several clusters, which have been repeatedly activated. Some clusters coincide with the position of the previous activity; the others have activated so far inactive deep segments at the southern edge of the Nový Kostel fault. Besides the shift of the hypocenters to the edges of the previously active area we observe a southward migration of the activity and an increase of maximum depths of earthquakes from 10 to 13 km. The waveform similarity analysis disclosed that some fault patches consist of only a single, repeatedly activated fault plane, while the others consist of multiple, differently oriented fault planes activated almost simultaneously. Most of the focal mechanisms are consistent with the geometry of hypocenters showing NNW-SSE trending steep fault planes with left-lateral strike-slip mechanisms and varying dip-slip component.

Key words: earthquake swarms, relative location, waveform similarity, seismic activity, West Bohemia/Vogtland

1. INTRODUCTION

A geodynamic activity in the region of West Bohemia (Czech Republic) and Vogtland (Germany) is demonstrated mainly by the re-occurrence of intraplate earthquake swarms of mostly $M_L < 3.5$ earthquakes. The strongest documented earthquakes occurred during the swarms in 1872 and 1908 and reached the magnitude of about 5.0. The so far largest instrumentally recorded swarm was that of 1985/86, which showed maximum magnitudes

of 4.6, see *Neunhöfer et al. (2004)* for review. High gas-flow manifested by moffets, CO_2-rich mineral springs and gas vents (*Weinlich et al., 1998*; *Heinicke and Koch, 2000*; *Bräuer et al., 2003*) with anomalous content of mantle-derived ^3He (*Bräuer et al., 2007*) are the other striking features. However, a precise geodetic monitoring of vertical motions of the surface in the seismically active area has not revealed significant systematic trends yet (*Mrlina and Seidl, 2008*). Quaternary volcanism was active there until the Holocene (*Wagner et al., unpublished results*); two extinct volcanoes, Komorní Hůrka and Železná Hůrka, are located only 15 and 25 km apart from the main epicentral zone. Recent study of *Mrlina et al. (2007)* points to the existence of a Quaternary maar volcano close to Železná Hůrka.

The region belongs to the western part of the Bohemian Massif (Fig. 1) where three principal tectonic units - the Saxothuringian, the Moldanubian, and the Teplá-Barrandian touch (*Babuška and Plomerová, 2008*). Its eastern part is intersected by an ENE-WSW striking neotectonic structure, the Eger Graben, which is terminated at the Mariánské

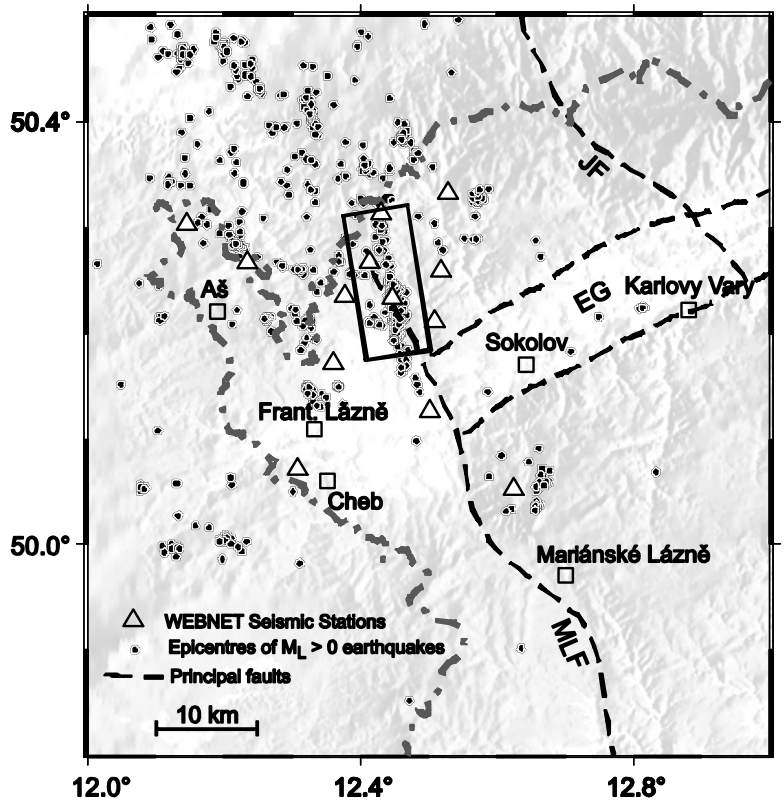

Fig. 1. The earthquake swarm area of West Bohemia/Vogtland with the earthquake epicenters, seismic stations of the WEBNET network and principal faults (MLF - Mariánské Lázně Fault, EG - Eger Graben, JF - Jáchymov Fault). The rectangle indicates the most active Nový Kostel area.

Lázně fault striking NNW-SSE. Most of the seismicity is associated with the Mariánské Lázně fault, which probably terminates at the northern edge of the Cheb basin (Fig. 1). The existence of another active fault system trending N-S, the Počátky-Plesná zone, has been recently discussed (*Bankwitz et al., 2003*).

The Nový Kostel (NK) focal zone dominates the recent seismicity of the whole region: since 1991 almost 90% of total seismic energy was released in this zone. Besides the larger swarms of 1985/86 ($M_L = 4.6$), January 1997 ($M_L = 3.0$) and 2000 ($M_L = 3.2$), *Fischer and Horálek (2003)* have identified further 27 microswarms (swarms including only microearthquakes) and solitary microearthquakes ($M_L < 2$ events) in the period between 1991 and 2001. Relative location revealed a pronounced planar character of the NK focal zone: most of the events were located at the main focal plane striking 169° north and dipping 80° west at depths between 6 and 11 km. The position and geometry of the main fault plane match quite well with the supposed Počátky-Plesná tectonic line. The focal mechanisms of the extensive 2000 swarm agreed quite well with the geometry of the focal zone, which proves that the swarm events correspond to progressive rupturing of one fault plane (*Hainzl and Fischer, 2002*; *Fischer and Horálek, 2005*). The January 1997 swarm showed anomalous character because its spatial pattern did not match the main focal plane. *Horálek et al. (2000b)* used visual-type analysis to subdivide the swarm events to families for which a typical moment tensor was determined. *Fischer and Horálek (2003)* have also found that in the depth view the microswarm hypocenters lined up along two parallel seismogenic lines whose plunge of 32° to the south was equal to the prevailing rake angle of focal mechanisms. The overall fault area occupied by the hypocenters in the time span of 1991–2001 was 12 × 4 km, however several segments of the fault were liable to reactivation.

In this paper we show how the seismicity pattern in the NK zone changed after the 2000 swarm. We employ a master-event location method to obtain a focused picture of seismicity and compare the seismicity distribution in the period between 2001 and 2007 with that of the period between 1991 and 2000. We use cross-correlation analysis to identify multiplets, i.e. events with similar waveforms and focal mechanisms. We examine if individual clusters, i.e. groups of closely located events, correspond to a single multiplet or if they include different multiplets indicating that different fault planes were activated within each cluster. For selected multiplets we determine focal mechanisms and compare them with the geometry of the cluster. We also examine reactivation of individual patches of the fault plane and show in detail the pattern of the fast microswarm of February 2007.

2. LOCATION OF EVENTS

We used three-component seismograms from the WEBNET seismic network (*Horálek et al., 2000a*) consisting of 12 short-period stations sampled at 250 Hz. The direct P- and S-wave onset times were measured manually, with the aim to achieve the accuracy of ±1 sample for P-waves and of ±2 samples for S-waves. This was possible due to the impulsive character of most of the P and S waveforms and the usage of hodograms in uncertain cases. Similarly to our previous studies (*Fischer and Horálek, 2000, 2003, 2005*) we used a slightly modified master event procedure after *Zollo et al.*

(1995) with the use of a 1-D gradient velocity model of *Málek et al. (2000)*. Using a grid search method, we found the minimum of the variance $V = (1/N)\sum_i \left(\Delta T_0^i - \overline{\Delta T_0}\right)^2$ of the difference ΔT_0 between the origin times of the master event and located events. Here T_0^i is the origin time calculated from the arrival time and travel time of the phase i, $\overline{\Delta T_0}$ is the mean arrival time difference and N is the number of phases. Similar to other relative location methods, it is required that the distance of the located events to the master event is much smaller than the hypocentral distance, i.e. the rays are almost identical.

To extend the applicability of the method to a larger area we use multiple master events. The influence of the variance V_j corresponding to the j-th master event is weighted by its distance r_j to the located event in the form of $w_j = \left(\overline{r}/r_j\right)^2$, where $\overline{r}$ is the mean distance. Then the minimized misfit function is

$$V(x, y, z, T_0) = \sum w_j V_j \ ,$$

where the location errors of the relative hypocentre coordinates were estimated as the distance from the hypocentre at which the misfit function reaches the level $V_{min} + dV$, where dV was derived by the error propagation (*Fischer and Horálek, 2003*) from the expected values of arrival time errors (4 ms for P waves, 8 ms for S waves). As master events we selected seven events, which were well-recorded at all available stations (Table 1). Their locations, obtained by an absolute location procedure using a grid search algorithm, were equally distributed along the activated part of the main fault plane (see Fig. 2).

In total 2183 events from the period between 2001 and 2007 in the magnitude range from −1 to 2.5 were successfully located with the mean location errors of 100 m, 140 m and 180 m for the X, Y and Z coordinates. The use of seven master events resulted, compared to a usage of one master event, in the reduction of the mean location residual from 19.3 ms to 15.2 ms. To get a comprehensive image of the spatio-temporal evolution of the activity we supplemented this dataset with the locations of seismicity from the period between 1991 and 2000 (*Fischer and Horálek, 2003*) and limited our study only to the $M_L > 0$ events. This resulted in 989, 5941 and 880 events for the periods 1991–1999, 2000 and 2001–2007, respectively.

Table 1. Coordinates of master events.

Date	Time	Event ID	Latitude [°N]	Longitude [°E]	Depth [m]
00-09-18	18:29	P3500A	50.2254	12.4474	8660
97-01-17	22:57	M418A	50.2358	12.4462	9050
00-08-31	12:15	P828A	50.2143	12.4500	9980
00-10-23	08:40	P4739A	50.2120	12.4570	7800
00-11-07	20:15	P6008A	50.2069	12.4534	9660
00-12-23	15:27	P6710A	50.2397	12.4505	7330
04-02-22	09:31	T51A	50.2117	12.4303	12860

3. SPACE-TIME DISTRIBUTION OF SEISMICITY

Seismicity pattern in the NK area (Fig. 2) points to a few striking features. Two distinct clusters could be distinguished in the map view. The first one represents the eastern belt of hypocenters of about 13 km length, which includes the vast majority of events. The second one is a small cluster in the NW part of the map view containing several dozens of deep events (below 11 km) indicated by ellipses in panels (a) and (c).

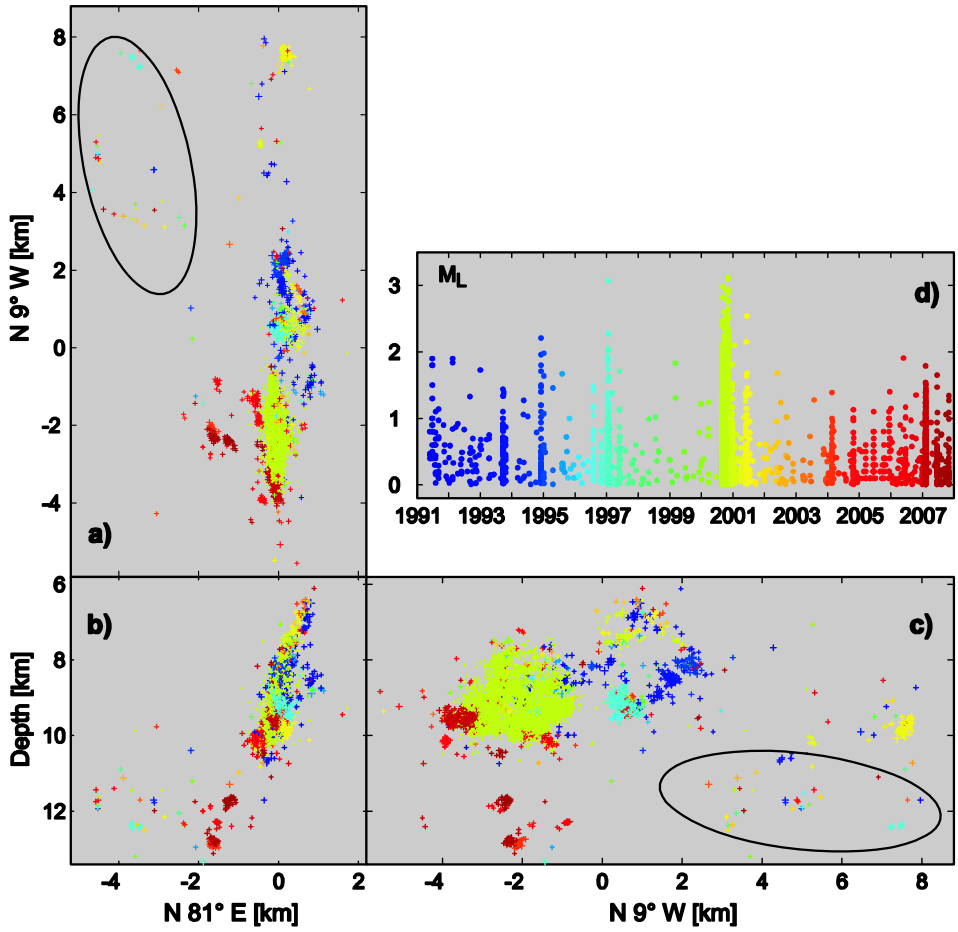

Fig 2. Space-time distribution of hypocenters in the Nový Kostel focal zone in the period between 1991 and 2007. The different panels show the map view **(a)**, the depth view from the south to the north **(b)** and from the east to the west **(c)** and a magnitude-time plot **(d)**. The horizontal coordinates are rotated to the strike of the fault of 351°. Ellipse denotes the NW deep cluster, colour coding from blue to red is proportional to time. The frame of the map view is indicated by rectangle in Fig. 1.

While the seldom seismicity in the deep NW cluster persisted during the whole studied period, the main eastern cluster including all the swarms and microswarms showed only shallow activity above 10.5 km during the first part of the studied period (1991–2001). An increase of the maximum depth from 10.5 to 13 km has occurred after 2004.

According to the temporal evolution of seismicity, the period after the 2000 swarm (Fig. 3) could be subdivided into three time intervals. The first one (year 2001) was characteristic by dying away of the 2000 swarm activity, namely during the $M_L = 2.0$

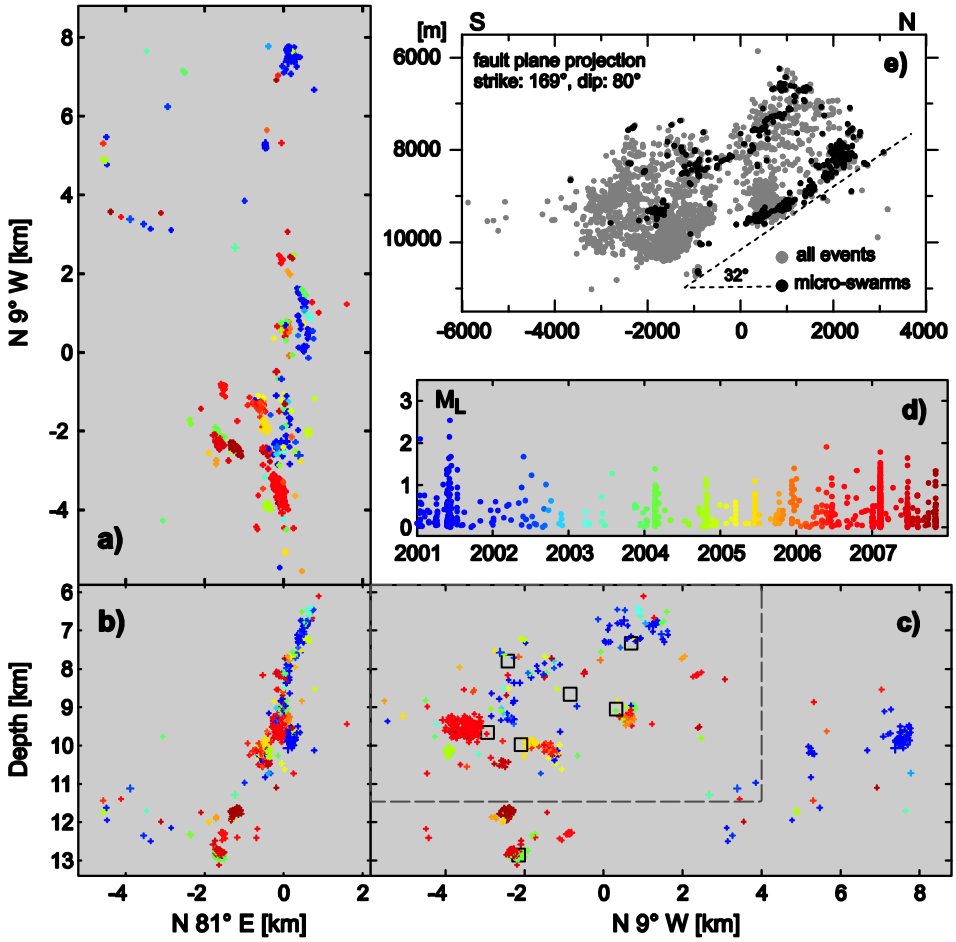

Fig. 3. Space-time distribution of the hypocenters in the Nový Kostel focal zone in the period between 2002 and 2007 (a–d). In (e) the distribution of microswarms in the period between 1991 and 2001 from *Fischer and Horálek (2003)* is shown for comparison. In contrast to the period between 1991 and 2001 when the microswarms were clustered in two parallel seismogenic lines plunging with an angle of 32° to the south, no similar behaviour has occured since 2002. In (c) the small rectangles show the position of seven master events and the dashed rectangle indicates the fault area displayed in (e).

swarm of June 2001 at the northern edge of the NK area (blue cluster). The next two years (2002–2003) were almost quiet with small background seismicity including only rare $M_L > 1$ events. The activity awaked in February 2004 with a microswarm close to 13 km depth (green cluster). Since then a repeated occurrence of microswarms takes place with systematically increasing maximum magnitudes. In this respect, the recent four years (2004–2007) resemble the period of increased microswarm activity from late 1993 to 1997, which was also preceded by a period of relative quiescence between 1992 and 1993.

The depth of this new activity (2004–2007) exceeds in most cases 9 km (see Fig. 2), which is a significant change compared to the previous activity that was limited to the depth range from 6 to 10.5 km. Another interesting observation is the shift of activity to the south as most of the post-2000 swarm events (red symbols) occur in the southern part of the focal zone in contrast to the pre-2000 swarm activity (blue symbols), which occurred in the central and northern parts. It could be accordingly hypothesized that after the 2000 swarm we observe a migration of the activity to the south and to greater depths. As regards the characteristic linear geometry of microswarms occurrence in the period between 1991 and 2001 (*Fischer and Horálek, 2003*), no similar behaviour has been observed since 2002 (compare Fig. 3c and e). Only a diffuse seismicity occurred along the upper seismogenic line during 2002 and 2003, probably due to stress readjustments after the 2000 swarm (Fig. 3c). Instead, the recent microswarms occur in concentrated clusters in the deeper parts of the fault plane. It appears (see Fig. 3b) that the seismicity propagates downwards from 8 to 13 km, approximately along the prolongation of the plunge of the main fault plane. Thus one could speculate that if the microswarm activity before the 2000 swarm had a causal relationship to a generation of the 2000 swarm, the recent microswarms could be viewed as a precursor to a future swarm in larger depths in the southern part of the focal zone.

The space distribution of seismicity indicates that some patches of the fault zone show large density of events. To quantify the distribution of fracturing along the fault zone we estimated the fracture area of each event using the circular source model of *Brune (1970)*, the stress drop of 10 MPa and an empirical relation between magnitude M_L and seismic moment M_0 for the area of interest $\log M_0 = 1.05 M_L + 11.3$ (*Hainzl and Fischer, 2002*). We accounted for the limited location accuracy by subdividing the fault zone volume into a number of cells whose spacing corresponds to the mean location error in the x, y and z directions and calculated the sum of the ruptured area in each cell. Accordingly, we get the ratio between the total area of fault planes occurring in the cell and the cross section of the cell in the direction of the fault (YZ plane). This number represents the number of overlapping ruptures being activated during the investigated period and could be interpreted as the number of reactivations of the cell. Fig. 4 shows colour coded number of reactivations for the NK focal zone for the investigated period between 1991 and 2007. It turns out that the reactivation rate is strongly unequal. The largest values above 15 correlate with the distribution of large events in the 1997 and 2000 swarms (compare Fig. 8 in *Fischer and Horálek, 2003*). It is also of interest that the patches activated after the 2000 swarm (indicated by ellipses) lie at the edges of the previous activity and accordingly show no reactivation (except the two shallowest clusters). Similar spreading of activity to the margins of previously ruptured area was predicted by the viscoelastic block model of *Hainzl (2003)*.

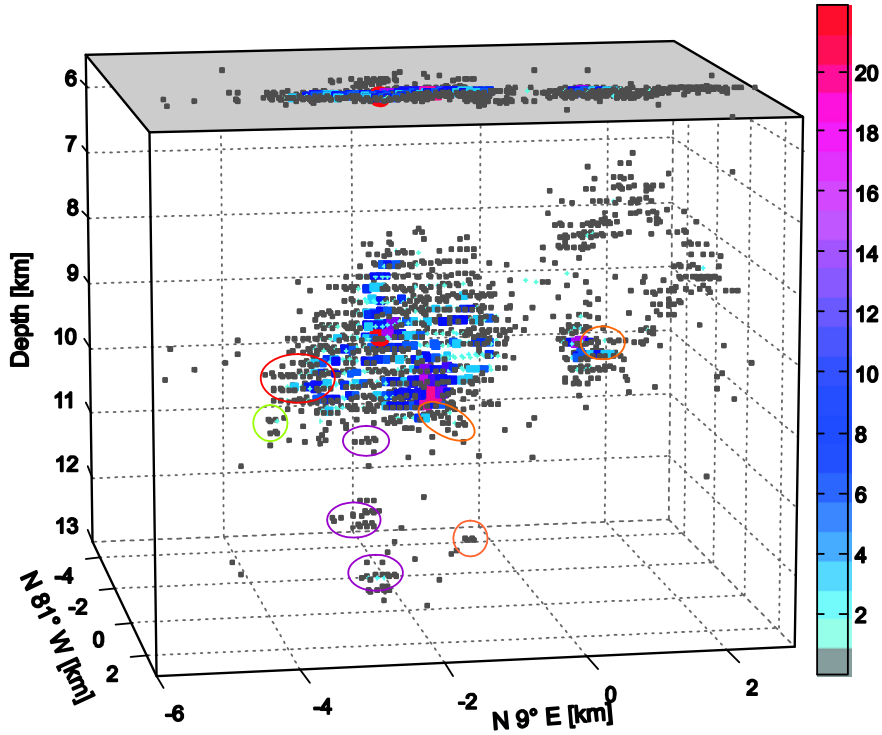

Fig. 4. Number of reactivatons of fault plane patches with spacing equal to the location error. The colour and size of symbols is proportional to the number of reactivations, which is defined as the ratio of the total ruptured area in the corresponding patch and its cross section in the fault direction. The coordinate system is the same as in Figs. 2 and 3. The ellipses indicate new activity using the same colours as in Fig. 3.

It should be noted that the utilized seismic data were not fully homogeneous during the whole observation period; the number of stations increased with time and few stations have been discontinued and moved to a new position. However, we are not aware of any influence of these small changes to the observed patterns. To suppress the effect of possible variations in detection capability we limited our study only to $M_L > 0$ events. The effect of changing station configuration to the locations was minimized by the adopted relative location scheme (see e.g. *Fischer and Horálek, 2000*).

4. WAVEFORM SIMILARITY ANALYSIS AND FOCAL MECHANISMS

We applied the waveform similarity analysis to the data of the 2001–2007 seismicity to find events with similar waveforms at individual stations. Two events produce similar waveforms at a particular station if their hypocenter locations and focal mechanisms are sufficiently similar. Such events are commonly termed as multiplets (*Got et al., 1994*). Similarity analysis is commonly used for two purposes: first, it helps reduce the large

datasets to a smaller number of multiplets with a common location and focal mechanism (*Schulte-Theis, 1996*; *Eisner and Arrowsmith, 2006*). Second, it enables to precise the arrival time measurement and accordingly the hypocenter location (*Got et al., 1994*; *Waldhauser and Ellsworth, 2000*; *Hemmann et al., 2003*). In this study we use the similarity analysis for classifying the events to the multiplets in order to learn more about the variability of focal mechanisms within each hypocenter cluster.

We extracted the waveform data of events with magnitude $M_L \geq 0.0$ from the period between 2001 and 2007 for all the P and S-wave phases in the time window of 2 s length centered at the manually picked arrival time. To suppress the low and high frequency noise the seismograms were band pass filtered in the range of 1–30 Hz. The cross-correlation was applied to the vertical seismogram component for P waves and to both horizontal components for S waves. At each of the 12 stations we calculated the cross-correlation function for each pair of events. The maximum value of the cross-correlation coefficient (*CC*) was stored in a cross-correlation matrix for each individual station, which resulted altogether in 36 matrices (12 for each component).

The next step was to generate the network cross-correlation matrix, which characterizes the similarity of the events for the whole network. As the most appropriate we found the method of "asymmetrical trimmed mean" of *Maurer and Deichmann (1995)* because it effectively excludes low values of *CC* and it also resolves the problem of missing event records at some stations. For this purpose only the N and E cross-correlation matrices were used, because *CC* of vertical components were significantly smaller than *CC* of horizontal components (see Fig. 5). For each station we constructed the CC_{NE} correlation matrix as the mean value of the corresponding N and E correlation matrices and, using the approach of *Maurer and Deichmann (1995)*, we created the mean network cross-correlation matrix shown in Fig. 5a. The lower and the upper triangular

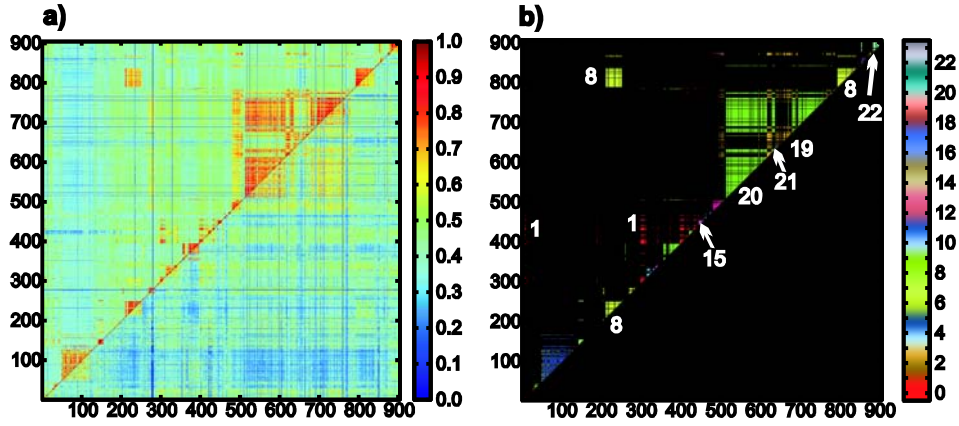

Fig. 5. **a)** The network cross-correlation matrix. The lower triangular matrix shows the cross-correlation coefficients (*CC)* for P-phase recorded on vertical component and the upper triangular matrix shows the *CC* for S-phases recorded on horizontal components, see more details in text. The higher values of *CC* correspond to the more similar events. **b)** Multiplets identified by similarity analysis. Numbers and colours correspond to the multiplets indicated in Figs. 6 and 7.

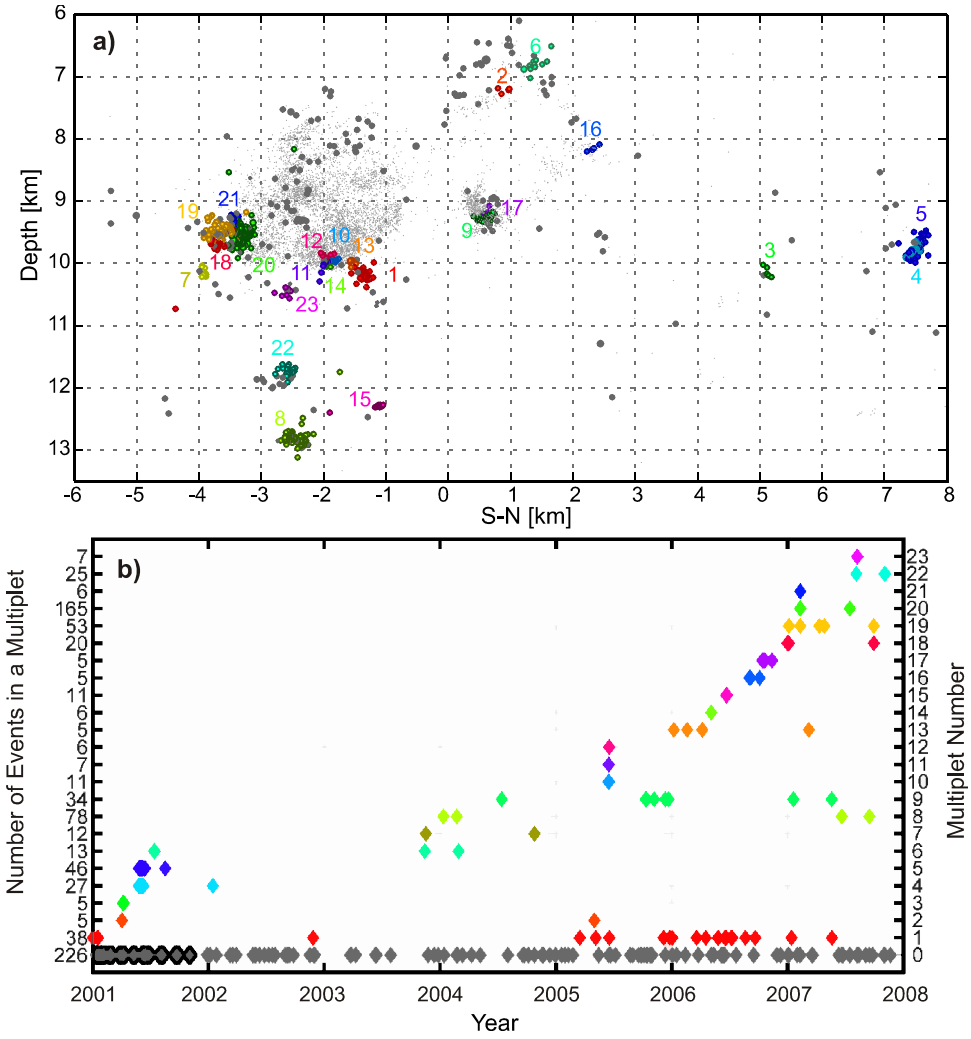

Fig. 6. The multiplets in S-N depth-section below the NKC station **(a)** and their time distribution **(b)**. The multiplets are colour coded and numbered. The events not associated with any multiplet are dark grey; seismic activity prior to 2001 is marked by small grey dots. The size of symbols in (a) indicating events since 2001 is proportional to magnitude.

matrices indicate the *CC* for the P and S waves, respectively; the diagonal represents the autocorrelation coefficients (equal to one). The events are sorted chronologically from left to right and from down to up. The patches of high *CC*, mainly along the diagonal, indicate the identified multiplets.

To create groups of similar events, the network cross-correlation matrix was reduced to a few multiplets. We tested two approaches - the "single linkage clustering" (*Schulte-Theis, 1996*) and the method of *Maurer and Deichmann (1995),* which was found more

suitable for our purpose. It uses four thresholds, however only two of them (*Tx* - cluster separation and the *Ts* (= CC_{NE}) - S-wave similarity thresholds) are critical. Another criterion for clustering was that each multiplet should contain at least 3 events (to limit the number of multiplets) and that more than a half of processed events should belong to multiplets. The thresholds were tested in a range of 0.1–0.9 for *Tx* and 0.40–0.99 for *Ts*. In spite of this relatively wide range of values, the multiplets were quite stable and also their number did not exceed an acceptable count of 27. With increasing *Tx* the multiplets were just subdivided into smaller ones, but their seismograms were found often similar. Accordingly, *Tx* was chosen as low as 0.2. To keep the condition of similarity of seismograms we chose *Ts* as high as 0.80. The identified multiplets for the selected *Tx* an *Ts* thresholds are indicated in Fig. 5b.

Fig. 6 shows the S-N vertical cross section of the NK focal zone with colour coded multiplet locations and their time distribution. Some multiplets were active only in short time intervals but some of them were activated repeatedly, e.g. the multiplets 1, 6, 8 and 9.

To verify the reliability of the classification of the dataset to a limited number of multiplets and to learn more about the faulting type of these events we determined the focal mechanisms of selected events within each multiplet. We used the method of *Maeda (1992)* which is implemented in the Seisbase package (*Fischer and Hampl, 1996*) used for routine processing of WEBNET seismograms. We used at least 10 P-wave polarity and amplitude measurements and found multiple events with stable focal mechanisms for each multiplet. In Fig. 7 composite plots of focal mechanisms for the most interesting multiplets are shown along with composite plots of the N-S component of the S waves recorded at the NKC station. For each multiplet we show the focal mechanisms of events with sufficiently stable solution. The selection according to the number of possible solutions and the quality of the fit gave about 60% of events for each multiplet. The similarity of seismograms in each multiplet (see Fig. 7) proves that the source and propagation effects were the same during each reactivation of the multiplet and is an independent evidence of similar location and focal mechanisms for each multiplet.

5. DETAILED VIEW OF SELECTED MULTIPLETS

In the following we would like to demonstrate the variability of the activity using several earthquake clusters. The first two examples illustrate such cases when multiple reactivations of a single hypocenter cluster lead to a slippage of the same fractures.

The deepest multiplet (No.8 in Figs. 6 and 7) has been activated already four times (in January and February 2004 and in June and September 2007). Despite the three reactivations, the similarity analysis shows only a single type of seismograms (see also Fig. 8a). The normal faulting focal mechanisms are quite stable with a steep NW-SE nodal plane and another NNW-SSE low-angle nodal plane. To find the fault plane we compared the elongation of the multiplet with the location error bodies and the focal mechanisms (Fig. 9). For the error analysis we used one of the largest events from the main episodes in February 2004 (22-Feb-04, 16:46, M_L = 1.0) and June 2007 (20-Jun-07, 19:35, M_L = 1.6). We tested the hypothesis that during each episode only one fracture was activated and the cluster elongation is caused by random location errors. We determined the location of

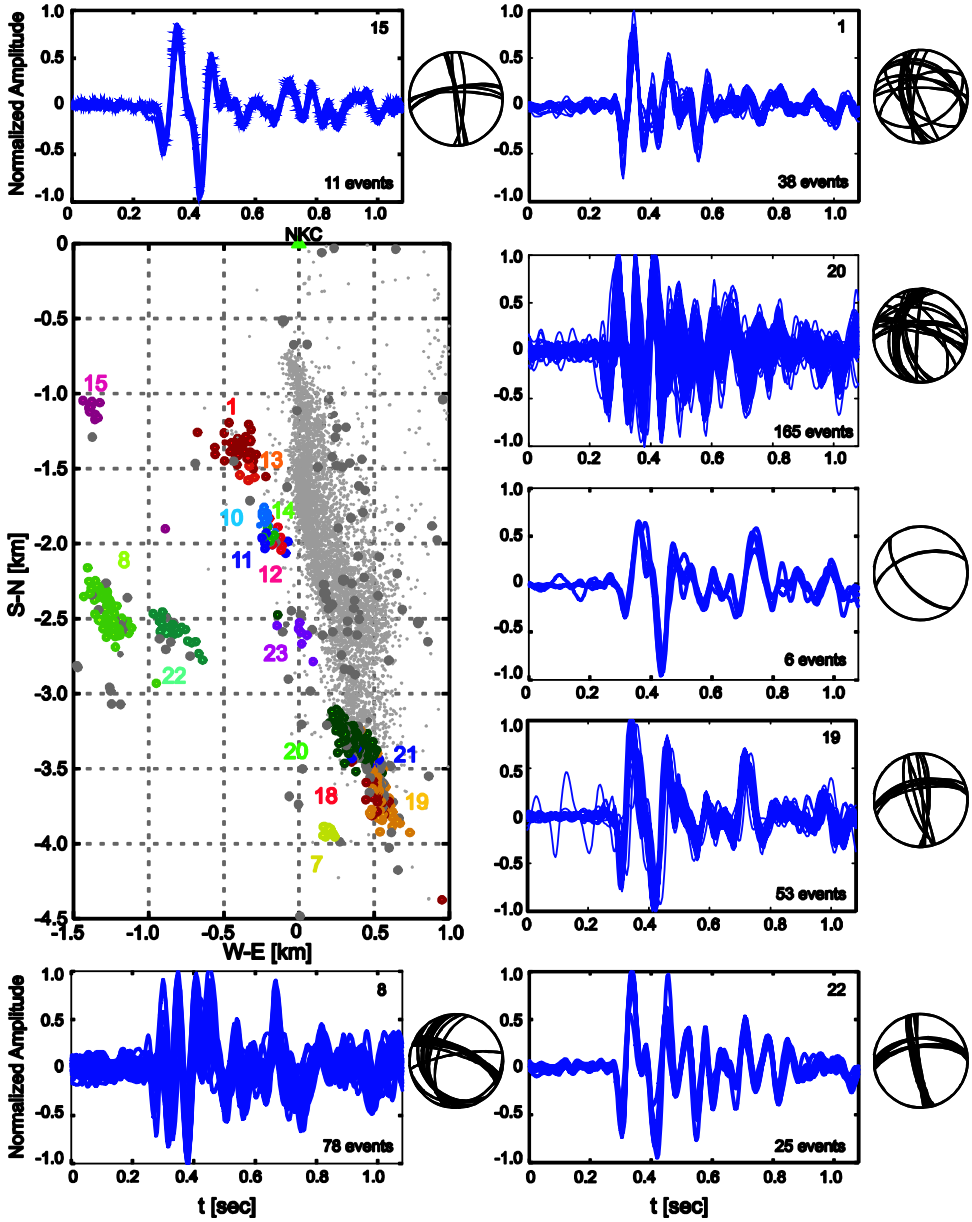

Fig. 7. Position of multiplets in a map view. S-wave seismograms (N-S component at the station NKC, filter 1–30 Hz) and typical focal mechanisms of the selected multiplets 1, 8, 15, 19, 20, 21 and 22. All focal mechanisms are left-lateral. The map view is north-south oriented for comparison with the focal mechanism plots. See Fig. 6 for colour coding, time occurrence of the multiplets and further explanation.

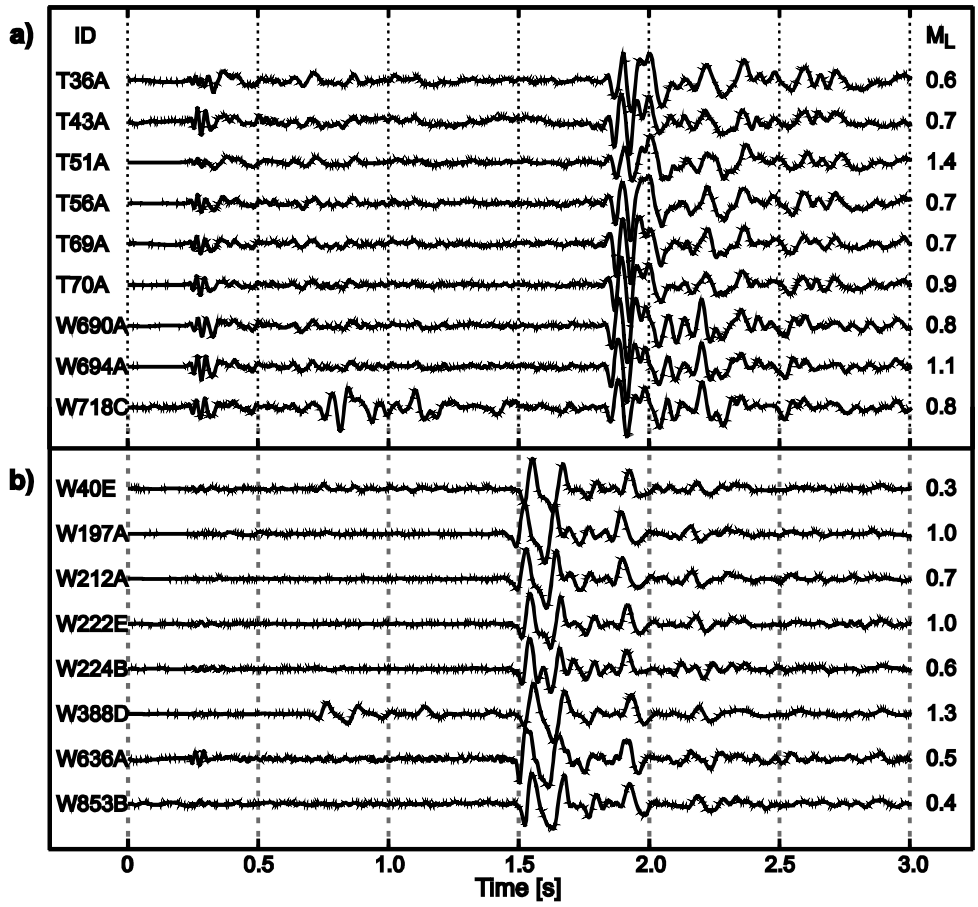

Fig. 8. N-S component waveforms for the events of the multiplets 8 **(a)** and 19 **(b)** for which focal mechanisms are shown in Fig. 7. The seismograms recorded at the NKC station are aligned according to the arrival time of P waves (0.25 s) and band-pass filtered (1–30 Hz) similar as for the cross-correlation analysis. For each waveform its event ID (left) and local magnitude (right) is indicated.

both events using 100 realizations of random arrival time error (Fig. 9b); we used a conservative estimate of 1.5 samples for P and 3 samples for S waves. By comparing Figs. 9a and 9b it turns out that the horizontal elongation of the cluster is well defined, however its vertical elongation lies just above the location error. Thus the two clusters are not distinguishable in the depth section. Hence the comparison with the focal mechanisms gives ambiguous results. The map view suggests the low-angle nodal plane (dashed line) as a probable fault plane, but the depth section identifies clearly the steep nodal plane (full line) as a fault plane. However, with respect to the expressed poor resolution in the depth section we leave the question of the active fault plane in this multiplet open.

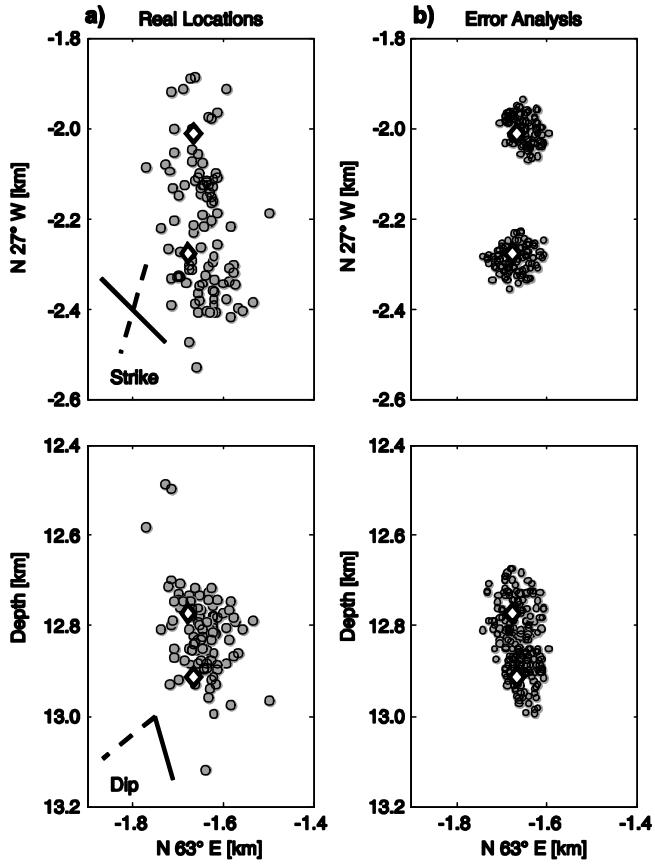

Fig. 9. Map view **(top)** and cross section **(bottom)** of the deep cluster 8; horizontal coordinates are rotated along the cluster extension. The cluster was activated twice; diamonds show the positions of the representative events E1 and E2 of each episode. In **(a)** circles show locations of all events, full and dash lines show the strike and dip of two nodal planes of a typical fault plane solution (strike and dip of the first and second plane are 297°/69° and 178°/38°). In **(b)** circles show the location of events E1 and E2 obtained from randomly perturbed arrival times (the error of ±6 ms and ±12 ms for P and S waves, respectively).

The multiplet No.1 (indicated by red in Figs. 6 and 7) is a similar case, showing numerous repeated activations during the whole period between 2001 and 2007. Its frequent reactivations were already demonstrated in Fig. 4, which has shown the largest reactivation rate precisely in the corresponding fault patch. Note that these events belong to a single multiplet which points, despite of large time span of these events, to the common focal mechanisms of this new activity. It is of interest that the position of this patch is identical with the isolated cluster activated on December 26, at the very end of the 2000 swarm (*Fischer and Horálek, 2003*). In other words, so far quiet patch was activated at the end of the 2000 swarm and has been showing a repeated activity since that time.

A different situation occurs in case of microswarms in June 2005 and February 2007. The former one (June 2005, > 100 located events) lasted three days and acted on a fault patch only 300 m long and consisted of three multiplets 10, 11 and 12 with different focal mechanisms. The latter microswarm (February 2007, > 750 located events) showed three-event multiplets (19, 20 and 21) active during less than 24 hours; their focal mechanisms are shown in Fig. 7. This example indicates that differently oriented fractures within a small volume have been activated almost simultaneously.

The complicated space-time pattern of the February 2007 microswarm, which has activated the southern-most tip of the 2000-swarm patch, is obvious from Fig. 10. The hypocenter distribution indicates that a single, possibly incurvate fault plane was active. The activity started in January at the southern tip of the cluster (grey circles in Fig. 10 and the multiplets 18 and 19 in Figs. 6 and 7). After one month it continued by the microswarm of February 9 and 10 (colour-coded symbols in Fig. 10) showing a pronounced migration from the north to the south and after a period of a few hours back to the north and downwards. This extremely short microswarm was terminated by a "shot" of activity (red symbols) penetrating back to the south along a linear inclined belt. The magnitude-time plot points to four phases of activity, whose hypocenters appear to coincide with the different multiplets. In particular, while the second swarm phase (greenish colours) coincides with the strike slips of the multiplet 19, the remaining phases occurring in the north correspond to the oblique-normal strike slips of the multiplet 20. This microswarm was anomalous because of an unusual rate of seismic activity - its median interevent time was as low as 22 s, which is close to the so far fastest swarm of 2000 with the median interevent time of 19 s. The fast energy release is also illustrated in Fig. 8b, where S waves of two events occur within less than 1 s for the event W388D.

6. DISCUSSION

The space-time pattern of the seismic activity in the Nový Kostel focal zone points to the noticeable migration of hypocenters. The activity after the 2000 swarm follows the same elongated fault zone, however moves clearly to the south and to larger depths. Although the strike of elongation of epicentres seems to differ from that of the previous activity (see map view in Fig. 7), it appears more probable that the different lateral position of the hypocenters accounts for their different depths at an inclined and uneven fault surface. We verified this interpretation by fitting a plane to the hypocenter distribution for the hypocenters from the period between 2002 and 2007. Using the L1 norm we obtained a strike of 166° and dip of 67°. The comparison with the fault plane parameters (169° and 80°) for the period between 1991 and 2001 of *Fischer and Horálek (2003)* indicates that the new activity follows a similar fault plane. Its different dip could be explained either by a vertical curvature of a single fault or by an intersection of two fault planes with different dips (see Figs. 2b and 3b). In such a case the steep fault would

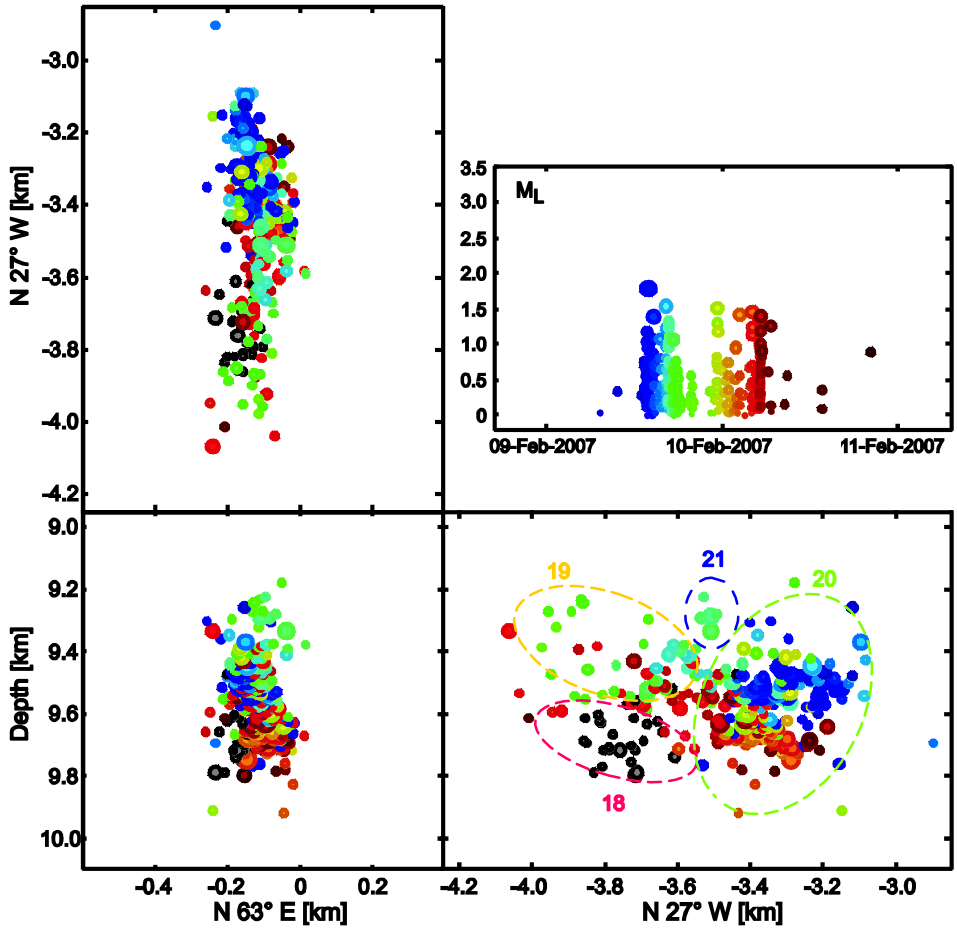

Fig. 10. Space-time distribution of $M_L > 0$ events of the southernmost cluster (the multiplets 18–21), the horizontal coordinates are rotated along the cluster extension. The activity of this cluster started by a weak microswarm (34 events with magnitudes up to 1.0 in the period between January 3 and 5, 2007 - grey circles). The subsequent activity from February 9 to 10 is indicated by colour scale proportional to the event number (281 events).

be active mainly in the depths smaller than 11 km, while the other would show activity between 9 and 13 km. The activated fault plane area seems partially to extend and partially to move to the south and to some larger depths. In contrast to the southward migration, the downward drift is probably limited by the brittle-ductile transition, which, for the NK area (*Babuška et al., 2007*), shows one of the shallowest depths in the whole seismoactive area of West Bohemia/Vogtland.

The repeated activation of several fault patches (see Fig. 4) indicates a repeated increase of criticality. This could be explained e.g. by a persisting inflow of pressurized

fluids at these places, which triggers the activity that is further controlled partially by stress transfer *(*e.g. *Hainzl, 2005*).

The focal mechanisms of the selected multiplets show, except the deepest multiplet 8, the NNW-SSE trending and left-lateral strike slip fault planes with small normal component. The deep multiplet 8 is anomalous because of a prevailing dip-slip character. A possible interpretation involving a change of the stress regime due to the large depth of this multiplet seems unlikely with respect to the multiplet 22, which is located only 500 m shallower and shows pure strike-slip mechanisms.

The waveform similarity analysis proved high efficiency for classifying large datasets according to the similarity of their hypocenter positions and focal mechanisms. Its further use for automatic processing of future activity is accented by its independence on knowledge of hypocenter locations and accordingly of the velocity model. The classification of the events to the multiplets could be used in future to guide the selection of suitable events for detailed study of their moment tensors.

7. CONCLUSIONS

We have analyzed the microseismic activity in the Nový Kostel area, the main focal zone of the West-Bohemia/Vogtland earthquake swarm region during the years between 2001 and 2007, which followed after the intensive swarm of 2000. We found the following characteristic features of the activity:

- After a relative quiescence in the period between 2002 and 2003 a seismic unrest started in 2004 in a form of a sequence of microswarms with magnitudes up to 2.0.
- The new microearthquake activity occurs along the main steeply dipping fault plane, which was the place of most of the previous swarms and background activity. Most of the hypocenter clusters occur at the edges of the previously active fault area. A pronounced migration to the south and downwards, from the depth of 10 to 13 km, occurs after the 2000 swarm.
- In many patches of the fault zone the estimated ruptured area significantly exceeds the surface area of a single fault. This indicates numerous reactivations of a single fault or rupturing of several parallel fault planes.
- The waveform similarity analysis showed the existence of two types of fault patches activated during a single swarm almost simultaneously. These patches contained either a single fault plane (one multiplet), or multiple, differently oriented fault planes (several multiplets). All the focal mechanisms are compatible with the geometry of hypocenters showing NNW-SSE trending, left-lateral strike slip fault planes with varying dip-slip component.
- The multiplet No.1 represents the striking demonstration of the shift of the activity to the edges of the previously active area. It is the most frequently reactivated multiplet and it was first activated on December 26, 2000, at the very end of the 2000 swarm.
- The frequent recurrence of microearthquake swarms emerging since 2004 indicates a new activation of the area after the 2000 swarm. Nevertheless, in spite of a relatively large number of events, the seismic energy of this activity is negligible

compared to the energy released during a large swarm, similar to that of the year 2000.

Acknowledgements: Our study was possible thanks to the precise arrival time measurements by A. Boušková. We thank J. Horálek for inspiring discussions and J. Soukup and P. Jedlička for handling the WEBNET network. The financial support by the Czech Grant Agency (project No.205/06/1780) and by the Grant agency of the Charles University (project No.105707) is greatly acknowledged.

References

Arrowsmith S.J. and Eisner L., 2006. A technique for identifying microseismic multiplets and application to the Valhall field, North Sea. *Geophysics*, **71**, V31–V40.

Babuška V., Plomerová J. and Fischer T., 2007. Intraplate seismicity in the western Bohemian Massif central Europe): A possible correlation with a paleoplate junction. *J. Geodyn.*, **44**, 3–5.

Babuška V. and Plomerová J., 2008. Control of volcanic phenomena in western Bohemian Massif by rejuvenated Variscan triple junction of ancient microcontinents. *Stud. Geophys. Geod*., **52**, 607–628.

Bankwitz P., Schneider G., Kämpf H. and Bankwitz E., 2003. Structural characteristics of epicentral areas in Central Europe: study case Cheb Basin (Czech Republic). *J. Geodyn.*, **35**, 5–32.

Bräuer K., Kämpf H., Strauch G. and Weise S.M., 2003. Isotopic evidence (He-3/He-4, C-13(CO_2)) of fluid-triggered intraplate seismicity. *J. Geophys. Res.*, **108(B2)**, 2070, doi: 10.1029 /2002JB002077.

Bräuer K., Kämpf H., Koch U., Niedermann S. and Strauch G., 2007. Seismically induced changes of the fluid signature detected by a multi-isotope approach (He, CO_2, CH_4, N_2) at the Wettingquelle, Bad Brambach (central Europe). *J. Geophys. Res.*, **112**, B04307, doi: 10.1029/2006JB004404.

Fischer T. and Hampl F., 1997. SeisBase - principles of a program and database for routine analysis of data from local seismic networks. *Acta Montana A*, **11**, 15–34.

Fischer T. and Horálek, J., 2000. Refined locations of the swarm earthquakes in the Nový Kostel focal zone and spatial distribution of the January 1997 swarm in Western Bohemia, Czech Republic. *Stud. Geophys. Geod.*, **44**, 210–226.

Fischer T. and Horálek J., 2003. Space-time distribution of earthquake swarms in the principal focal zone of the NW Bohemia/Vogtland seismoactive region: period 1985–2001. *J. Geodyn.*, **35**, 125–144.

Fischer T. and Horálek J., 2005. Slip-generated patterns of swarm microearthquakes from West Bohemia/ Vogtland (central Europe): Evidence of their triggering mechanism? *J. Geophys. Res.*, **110**, B05S21, doi: 10.1029/2004JB003363.

Got J.L., Fréchet J. and Klein F.W., 1994. Deep fault plane geometry inferred from multiplet relative relocation beneath the south flank of Kilauea. *J. Geophys. Res*., **99(B8)**, 15375–15386.

Hainzl S. and Fischer T., 2002. Indications for a successively triggered rupture growth underlying the 2000 earthquake swarm in Vogtland/NW Bohemia. *J. Geophys. Res.*, **107(B12)**, 2338, doi: 10.1029/2002JB001865.

Hainzl S., 2003. Self-organization of earthquake swarms. *J .Geodynamics*, 35/1-2, 157-172.

Hainzl S., 2005. Seismicity patterns of earthquake swarms due to fluid intrusion and stress triggering. *Geophys. J. Int.*, **159**, 1090–1096.

Heinicke J. and Koch U., 2000. Slug flow - a possible explanation for hydrogeochemical earthquake precursors at Bad Brambach, Germany. *Pure Appl. Geophys.*, **157**, 1621–1641.

Hemmann A., Meier T., Jentzsch G. and Ziegert A., 2003. Similarity of waveforms and relative relocalisation of the earthquake swarm 1997/1998 near Werdau. *J .Geodyn.*, **35**, 191–208.

Horálek J., Fischer T., Boušková A. and Jedlička P., 2000a: Western Bohemia/Vogtland region in the light of the WEBNET network. *Stud. Geophys. Geod.*, **44**, 107–125.

Horálek J., Šílený J., Fischer T., Slancová A. and Boušková A., 2000b. Scenario of the January 1997 West Bohemia Earthquake swarm. *Stud. Geophys. Geod.*, **44**, 491–521.

Maeda N., 1992. A method of determining focal mechanisms and quantifying the uncertainty of the determined focal mechanisms for microearthquakes. *Bull. Seismol. Soc. Amer.*, **82**, 2410–2429.

Málek J., Jánský J. and Horálek J., 2000. Layered velocity models of the western Bohemia region. *Stud. Geophys. Geod.*, **44**, 475–490.

Maurer H. and Deichmann N., 1995. Microearthquake cluster detection based on waveform similarities, with an application to the western Swiss Alps. *Geophys. J. Int.*, **123**, 588–600.

Mrlina J., Kämpf H., Geissler W.H. and Bogaard P., 2007. Assumed Queternary maar structure at the Czech/German border between Mýtina and Neualbenreuth (western Eger Rift, Central Europe): geophysical, petrochemical and geochronological indications. *Z. Geol. Wiss.*, **35**, 213–230.

Mrlina J. and Seidl M., 2008. Relation of surface movements to earthquake swarms in West Bohemia. *Stud. Geophys. Geod.*, **52**, 549–566.

Neunhöfer H. and Meier T., 2004. Seismicity in the Vogtland/Western Bohemia earthquake region between 1962 and 1998. *Stud. Geophys. Geod.*, **48**, 539–562.

Schulte-Theis H., 1996. Cluster analysis of European seismicity. *Cahiers du Centre Européen de Géodynamique et de Séismologie*, **12**, 201–223.

Waldhauser F. and Ellsworth W.L., 2000. A double-difference earthquake location algorithm: method and application to the northern Hayward fault. *Bull. Seismol. Soc. Amer.*, **90**, 1353–1368.

Weinlich F., Tesař J., Weise S.M., Bräuer K. and Kämpf H., 1998. Gas flux distribution in mineral springs and tectonic structure in the western Eger Rift. *J. Czech Geol. Soc.*, **43**, 91–110.

Zollo A., De Matteis R.,Capuano P., Ferulano F. and Innaccone G., 1995. Constraints on the shallow crustal model of the Northern Apennines (Italy) from the analysis of microearthquake seismic records. *Geophys. J. Int.*, **120**, 646–662.

Geophysical Journal International

Geophys. J. Int. (2013) doi: 10.1093/gji/ggt286

Geophysical Journal International Advance Access published August 28, 2013

Source parameters of the swarm earthquakes in West Bohemia/Vogtland

Jan Michálek[1,2] and Tomáš Fischer[1,3]

[1] *Institute of Geophysics, Academy of Sciences, 141 31 Prague, Czech Republic. E-mail: michalek@ig.cas.cz*
[2] *Faculty of Mathematics and Physics, Charles University in Prague, 121 16 Prague, Czech Republic*
[3] *Faculty of Science, Charles University in Prague, 128 43 Prague, Czech Republic*

Accepted 2013 July 15. Received 2013 July 13; in original form 2013 April 22

SUMMARY

The self-similarity of earthquake rupture scaling is a subject of ongoing debates. The output of multiple recent studies agrees on the fact that stress drops of earthquakes varies from 0.1 to 100 MPa over a broad range of seismic moments. We investigated the source parameters of 56 earthquakes in the magnitude range M_L from 0.8 to 3.3 occurred during the 2000 and 2008 swarm in West Bohemia/Vogtland in order to learn if the source scaling of these, most-likely fluid triggered events, differ from the observations in other seismogenic regions around the world. We used two approaches to calculate the corner frequency in the frequency domain: inverting for the corner frequency f_c of the displacement spectra and integrating of spectra by the method of Snoke. A single f_c for all stations was determined with attenuation correction defined by inverting for an event-dependent Q-factor. Similar dependence of the corner frequency on seismic moment was observed in the form $f_c \propto {M_0}^{-0.2}$, which is a much weaker scaling than expected for a constant stress drop model. Accordingly, the stress drops vary from 1 to 130 MPa and appears to grow with seismic moment as $\Delta\sigma \propto {M_0}^{0.43}$. The non-self similarity of the swarm earthquakes is supported by rather wide span of apparent stress ranging between 0.3 kPa and 1.2 MPa.

Key words: Fourier analysis; Earthquake source observations; Seismicity and tectonics; Seismic attenuation; Intra-plate processes; Europe.

1 INTRODUCTION

The earthquake swarms in West Bohemia/Vogtland pertain to the most striking manifestation of the present geodynamic activity of this intracontinental region (e.g. Horálek & Fischer 2010). This area is situated in the western part of the Bohemian Massif at a contact of different Variscan tectonic units—the Saxothuringian, Moldanubian, and Teplá-Barrandian (Babuška & Plomerová 2008). The ENE-WSW trending Eger Rift terminates close to the epicentral area and is intersected by the NNW-SSE striking Mariánské Lázně fault (Bankwitz *et al.* 2003). The geodynamic activity is manifested by emanations of CO_2 of mantle origin (Bräuer *et al.* 2008) and by Quaternary volcanism represented by Komorní Hůrka, Železná Hůrka and newly discovered maar structure of Mýtina (Mrlina *et al.* 2009). The frequently occurring weak earthquake swarms, mostly of magnitudes $M_L < 3.5$, concentrate in multiple focal zones in the depth range from 6 to 25 km (e.g. Horálek & Fischer 2010). Among them, the area near the village Nový Kostel (close to station NKC in Fig. 1) dominates with more than 80 per cent of the released seismic energy. It was the place of all the recent major swarms in the years 1985/86, 1997, 2000, 2008 and 2011 (Fig. 1).

The recorded seismic data were subject to various studies oriented to get insight into the generating mechanism of the earthquake swarms. The relative hypocenter locations in the area of Nový Kostel show a north-south steeply dipping fault plane of 8 km length in the depth range from 6 to 12 km whose orientation matches well with the source mechanisms (Fischer & Horálek 2005). The detailed analysis of spatio-temporal distribution of hypocenters shows that both the elastic stress transfer and high-pressurized fluids are responsible for the driving of the swarm activity (see, e.g. Hainzl & Fischer 2002; Fischer & Horálek 2005; Hainzl & Ogata 2005; Dahm *et al.* 2008; Fischer & Michálek 2008; Hainzl *et al.* 2012; or the review in Horálek & Fischer 2008). The source mechanism studies have shown that pure shear faulting prevails (Horálek & Šílený 2013) compared to tensile faulting that occurs in the case of specific fault plane orientation (Horálek *et al.* 2002; Vavryčuk 2002; Vavryčuk 2011). So far, little attention was devoted to the studies of static source parameters of these earthquakes. The inversion for seismic moment tensors of the year 1997 swarm by Horálek *et al.* (2002) provided the first estimate of scalar moments, which enabled establishing a scaling relation between the local magnitudes and scalar seismic moment (Hainzl & Fischer 2002) in the form $\log M_0 = 1.05\ M_L + 11.3$. Fischer (2005) used the Empirical Green Functions (EGF) method to study the source time functions of the year 2000 swarm events and found that many of them display a complex source time function composed of several pulses. Seismogram

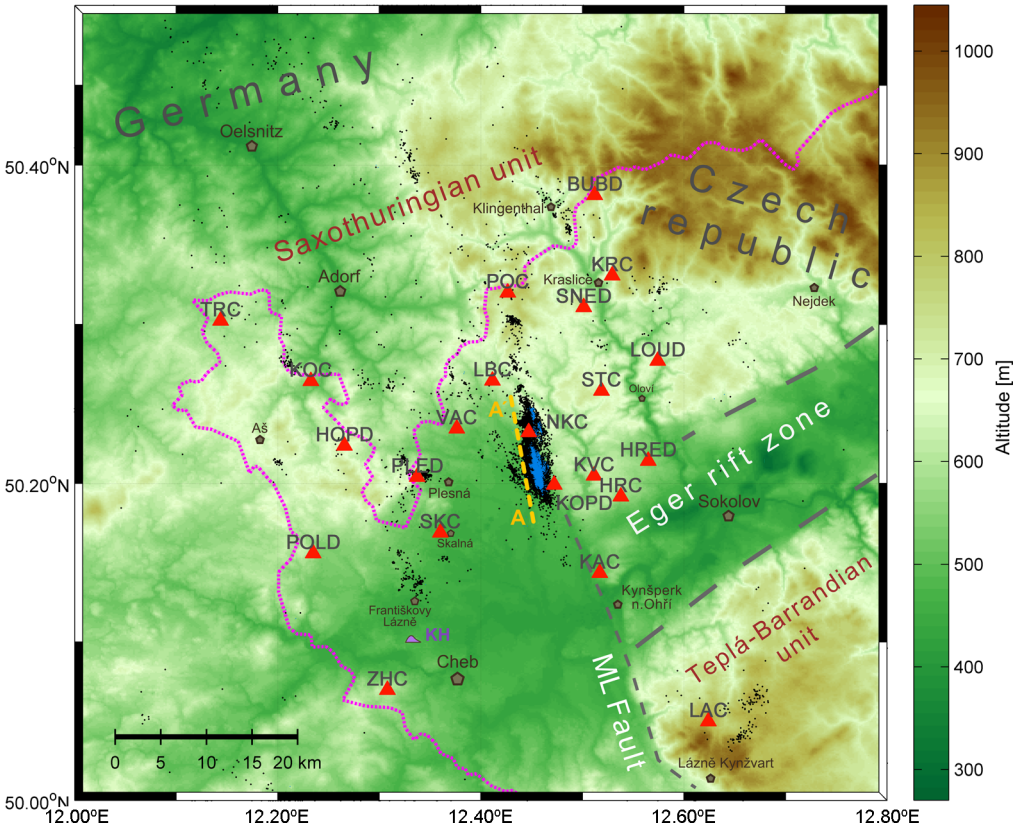

Figure 1. Map of WEBNET network and epicentres from 1991 to 2010 (black dots) in the West Bohemia/Vogtland region. The earthquake swarms 2000 and 2008 are highlighted in blue colour. The red triangles are WEBNET stations. Along the profile A-A′ the depth section is plotted in Fig. 2. The depression to the south from the NKC station is the tertiary Cheb basin; its eastern edge is terminated by the intersection with the Eger rift. KH is the quaternary volcano Komorní hůrka (topography based on SRTM3 from the USGS 2002).

modelling revealed that some of these events correspond to a fast stick-slip rupturing composed of several rupture episodes separated in time and space. Analysis of stopping phases of selected 2000-swarm events by Kolář & Růžek (2012) suggested the constant stress drop scaling of source radius and seismic moment.

The scaling between the seismic moment and size of the source with constant stress drop is commonly accepted as suggested by Aki (1967). Since then there are many studies aiming to find the confirmation of this law in real data, namely for small earthquakes because their more frequent occurrence could help in understanding the behavior of the big ones. The constant stress drop was observed for example by Abercrombie (1995) for earthquakes (M_L −1 to 5.5; $\Delta\sigma$ ∼ 0.1–80 MPa) in Cajon Pass borehole close to San Andreas Fault in southern California, by Prieto *et al.* (2004) who analyzed earthquakes (M_L 0.5 to 3.4) recorded by Anza seismic network in southern California, or by Yamada *et al.* (2007) who studied earthquakes (M_W 0.0 to 1.3; $\Delta\sigma \sim 3.2$–88 MPa) in South African gold mine. Also Viegas *et al.* (2010) reported high constant stress drop ($\Delta\sigma \sim 9.2$–240 MPa; median value 104 MPa) for the M5 intraplate earthquake, in 2002 and its aftershocks in Au Sable Forks, NY and concluded that the apparent breakdown in source dimension scaling is caused by the limited bandwidth of the records. Allmann & Shearer (2007) estimated the source parameters of 42 367 earthquakes from period 1984 to 2005 in Parkfield, central California; their stress drop varied between 0.1 and 100 MPa with median value of 6.75 MPa also stating that the stress drop is nearly constant with seismic moment, implying self-similarity over the $M_L = 0.5$ to 3.0 range. Similar results states a comprehensive analysis of about 60 000 earthquakes ($1.5 < M_L < 3.1$) in southern California (Shearer *et al.* 2006) with static stress drops between 0.2 and 20 MPa. Imanishi *et al.* (2004) used inversion method based on stopping phases to estimate source parameters of 25 microearthquakes ($1.3 < M < 2.7$) from the western Nagano prefecture, Japan. They found that the static stress drop ranged from 0.1 to 2 MPa only, do not vary with seismic moment and that the apparent breakdown in its scaling is an artifact of attenuation in the crust which mostly influenced the surface observations. They deduced that the earthquakes are similar over a wide range of magnitudes. Similar findings were reported by Kwiatek *et al.* (2011) in the study of picoseismicity ($-4.1 < M_W < -0.8$) from Mponeng Deep Gold Mine in South Africa ($\Delta\sigma \sim 0.01$–1.0 MPa). Oth *et al.* (2010) investigated the source characteristics of 1826 events from accelerometric borehole recordings ($M_{JMA} = 2.7$–8) throughout Japan and confirmed the self-similar scaling with median stress drop 1.1 MPa for crustal events.

On the other hand Harrington & Brodsky (2009) observed pulses of constant width for a group of earthquakes on San Andreas fault (M 1.4 to 3.7), which could be explained as a reactivation of the fault patches of similar size with variable stress drop 0.18–68 MPa. Urbancic & Young (1993) analyzed 85 mining-induced events ($-2.2 < M_W < -0.3$) in Strathcona mine (Sudbury, Ontario) at depth 710 m. They obtained also relatively high static stress drops within the range 0.16–83 MPa and pointed out to possible non-similar behaviour of small and large events. Oye *et al.* (2005) analyzed approx. 1500 events ($-1.8 < M_W < 1.2$) from 1400 m deep Pyhäsalmi ore mine in Finland. Their static stress drops range between 0.01 and 30 MPa and they noted that there

are strong factors which contribute to significant deviations from constant stress drop. Mayeda *et al.* (2005) used the coda waves to analyze four earthquake sequences (both natural and induced seismicity) in magnitude range $3.7 < M_W < 7.4$ to evaluate the scaling relations and they results strongly suggest the non-self-similarity. Edwards & Rietbrock (2009) studied attenuation and scaling relations of two magnitude-different datasets ($2.0 < M_{JMA} < 4.0$; $3.0 < M_{JMA} < 7.2$) and concluded that stress drop must increase with M_W, or that increase of the stress drop for smaller earthquakes is an artifact of the site effect.

All the studies report quite wide and similar ranges of static stress drop $\Delta\sigma$, which were by some authors interpreted as constant at specific sites/regions (valid source scaling relations) and as non-constant by others elsewhere (break in source scaling) by others. The comparison of the results of these studies is complicated because of different quality of the processed data sets and the methods used. We do not want to emphasize the differences in absolute values of the stress drop in the studies because these are model dependent. However, the trends in individual studies differ and show the source scaling dependence within the application of one single method. All the above studies emphasize the importance of the attenuation correction and its strong influence to the results, which can lead to under/overestimation of source parameters, primarily the corner frequency (e.g. Imanishi *et al.* 2004) and the other parameters consequently. The specific implementation of the attenuation corrections varies in individual studies and knowing the high trade-off level between the source parameters and attenuation it brings many degrees of freedom to the problem.

In this paper, we aim to examine the scaling between the seismic moment and source size for the earthquake swarm events in the West Bohemia region, in particular the range of the stress drop and possible anomalies in scaling for the small magnitudes events. We present the first estimates of the static source parameters—source dimension, seismic moment and stress drop of the West-Bohemia swarm earthquakes. We use the frequency domain absolute approach similar to that of for example Lindley & Archuleta (1992), Abercrombie (1995), Garcia-Garcia *et al.* (1996), Abercrombie & Rice (2005), Dobrynina (2009), Kwiatek *et al.* (2011). We employ the high-quality seismic data recorded by the WEBNET seismic network (Fischer *et al.* 2010) to bring new insights into understanding of source processes in this unique area of intracontinental seismicity.

2 DATA AND METHODS

2.1 Data and their preprocessing

We processed events ($0.8 \leq M_L \leq 3.3$) from the West Bohemia region (Fig. 1), which occurred during the earthquake swarms from August to December in 2000 and in October 2008. Selected events are located on a steeply dipping fault plane (strike 169°, dip 80°) in the depth range 7.5–10 km (Fig. 2). The number of stations used for spectral analysis differs for individual events. The configuration of stations in 2000 (12 stations) was less favourable than in 2008 (22 stations) in terms of the coverage of the focal sphere. In 2000 7, stations at maximum (usually 3–4 stations) were found suitable for our analysis because of the azimuthal position with respect to the hypocenters (Fig. 1). In 2008, we could use up to 18 stations (usually 12–15). The criteria for selecting events and stations for the inversion were the signal-to-noise ratio > 3 (i.e. ∼10 dB) in the analyzed frequency band of 1–100 Hz. Because of collocation

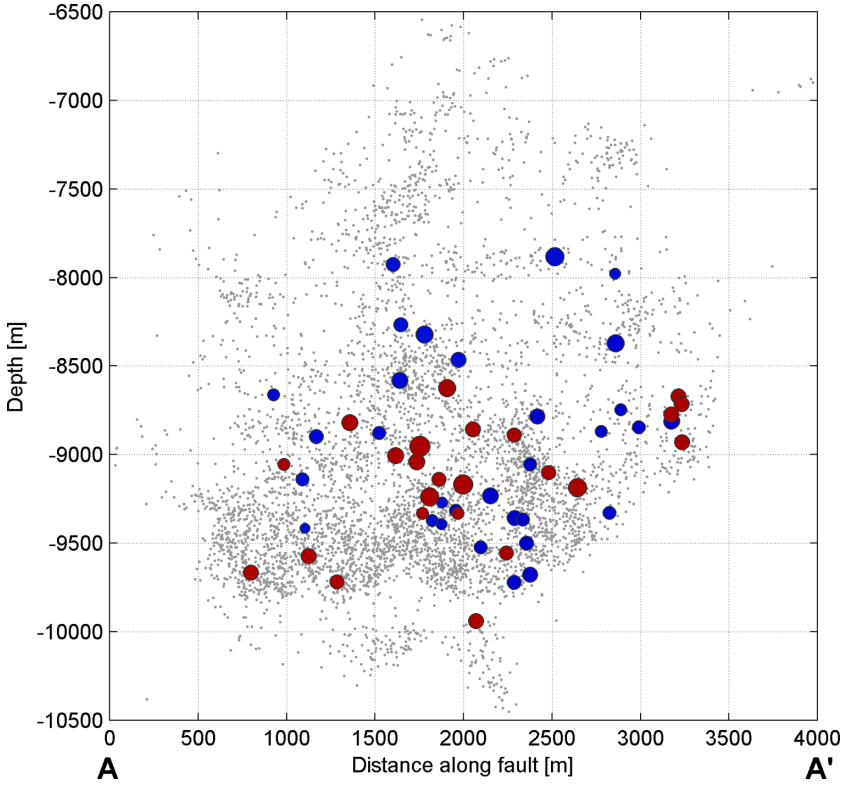

Figure 2. Distribution of hypocenters in the 2000 (blue) and 2008 (red) swarms along the fault plane (viewing from ENE to WSW). Size of the circles corresponds to seismic moment. Located by hypoDD location program (Waldhauser & Ellsworth 2000) in 1-D inhomogeneous velocity model (Málek *et al.* 2000).

of the events in these two periods we analyze them together with emphasis on 2008 swarm. We selected only events with clear and simple P pulse to eliminate multiple or complicated rupture processes. Accordingly, we eliminated the multiple events identified by Fischer (2005). These criteria allowed us to process events down to $M_L = 0.8$. The most limiting criterion was the signal-to-noise ratio, which did not allow us to reliably process smaller earthquakes at distant stations.

We analyzed *P* waves recorded on vertical components of short period seismographs SM-3 and LE-3D sampled by 250 sps. The frequency band was limited by the corner frequency of the velocigraphs (0.5 Hz for SM-3 and 1 Hz for LE-3-D) and by the sharp antialias filter in the recording unit at 80 and 100 Hz for the 2000 swarm and 2008 swarm, respectively. Data were transformed to displacement and no filtration was applied.

The displacement spectrum $U(f, R)$ of the source $S(f)$ can be decomposed as follows:

$$U(f, R) = I(f)G(R)P(f)L(f)S(f) \quad (1)$$

(e.g. Garcia-Garcia *et al.* 1996), where $I(f)$ is the instrument response, *G(R)* stands for geometrical spreading, $P(f)$ is anelastic attenuation, $L(f)$ is site effect, f is frequency and R is hypocentral distance.

The geometrical spreading term *G(R)* is frequency independent and is applied for calculating the seismic moment M_0. The frequency-dependent attenuation is expressed by anelastic attenuation $P(f) = \exp[-\pi ft/Q]$ and site effect $L(f) = \exp[-\pi f\kappa]$, where Q is quality factor and κ expresses the near surface attenuation. The unknown parameters Q and κ show the same functional dependence on frequency, which makes their separation impossible. Accordingly, we neglected κ and included the near surface attenuation into a single attenuation term $\exp[-\pi ft/Q]$. Our approach is justified by the fact that the hypocentral area is small (approximately 3 km in diameter) and rays are traveling along very similar paths (see Figs 1 and 2).

In our case, we could neglect the instrument response function $I(f)$ because all the earthquake corner frequencies were at least six times higher than the corner frequency of the instruments (we corrected the records for sensitivities only). Therefore the analysis was always carried out in the interval of the flat response of the instrument. Hence, for retrieving the amplitude source spectrum $S(f)$ two effects must be corrected for: (1) frequency-dependent anelastic attenuation (amplitude decrease with distance and broadening of the pulse in time domain) and (2) frequency-independent geometrical spreading (amplitude decrease with distance).

2.2 Spectra analysis

The frequency analysis is common and extensively used method for obtaining basic estimates of source parameters (e.g. recent studies: Abercrombie & Rice 2005; Allmann & Shearer 2007; Dobrynina 2009; Kwiatek *et al.* 2011) since the theoretical spectrum of circular rupture model was presented by Brune (1970). Although other improved and more realistic models of earthquake source were proposed (e.g. Sato & Hirasawa 1973; Boatwright 1980) we use the Brune (1970) source model (point source) because it is widely used and therefore a comparison with other studies can be performed. The advantage of this model is its simplicity. Commonly observed ω^{-2} spectral high-frequency falloff (e.g. Andrews 1986; Abercrombie 1995; Garcia-Garcia *et al.* 1996; Shi *et al.* 1998; Oth *et al.* 2010) fits our data well. More precisely, the observed spectra can be adapted to this model by finding the appropriate Q-value. We assume this model being sufficient enough to describe the sources of $0.8 \leq M_L \leq 3.3$ microearthquakes at hypocentral distances of about 6–30 km in the West Bohemia region.

For determination of source parameters, we used the absolute spectral approach applied to *P* waves on vertical component. The method is designed for routine processing of seismograms from the WEBNET network and is implemented in the SEISMON processing package (Mertl & Hausmann 2009; Michálek *et al.* 2011).

A time window of 1 s duration was used to calculate the spectrum. It contains 0.5 s of noise and the remaining part includes the signal of *P* wave with almost 100 per cent of its energy. The noise spectrum was calculated from the first half of the time window and replicated while the signal spectrum from the whole window (Fig. 3) using the multitaper method (MTT). Spectrum was interpolated in order to obtain equidistant frequency spacing in the logarithmic scale (10 points per decade). We did not apply any smoothing operator because the MTT itself smooth the spectrum naturally. The resulting displacement spectra were compared to the model

$$\Omega(f) = \frac{\Omega_0 e^{-\pi f t/Q}}{1 + \left(f / f_c\right)^n} \quad (2)$$

(Brune 1970) with the attenuation term, where Ω_0 is the low-frequency spectral level proportional to seismic moment, t is the *P* wave traveltime, Q is the quality factor for the whole ray path, f_c is the corner frequency and $n = 2$. The exponential part is responsible for the attenuation along the ray path. Because we assume a point source (i.e. no effects of source directivity), f_c is assumed to be the same for all stations.

2.3 f_c determination

By minimizing the logarithmic sum of residuals between the model (eq. 2) and data in L2 norm (residual function), we obtained a single corner frequency f_c for each earthquake and N values of attenuation factors Q (for N stations). In this way, multiple Q-factors were retrieved for each station for different events; their variation may account for example for the neglected source directivity and other source-dependent effects. As the hypocentral zone (Fig. 2) is rather small and the ray paths from all events to individual stations are similar we expected the Q-factors to be similar at each station because they include similar station-dependent effects of ray path and local site conditions. All the stations are surface stations built on a hard rock (crystalline or metamorphic units) and therefore we used $Q = 200$ (Stein & Wysession 2003) as an initial value for the inversion process. We used the simplex method (MATLAB implemented) to find the minimum of the residual function.

Using multiple stations for determining f_c led to stabilizing the process of obtaining the corner frequency compared to determining f_c from single-station data, which is also tested before each common inversion process. Stations HRC and SKC with strange pulse shape and $f_c > 50$ Hz from individual inversion were excluded from the common inversion to eliminate unrealistic results. We also excluded distant station ZHC because of the low signal-to-noise ratio. We evaluate the uncertainty of f_c by testing the shape of the residual function. Lower and upper error bounds of f_c were determined at frequencies corresponding to the 5 per cent increase above the minimum of the residual function (Viegas *et al.* 2010). We attributed all the deviations of the high-frequency spectral falloff from the ω^{-2} model to the effect of anelastic attenuation, assuming the frequency independence of Q.

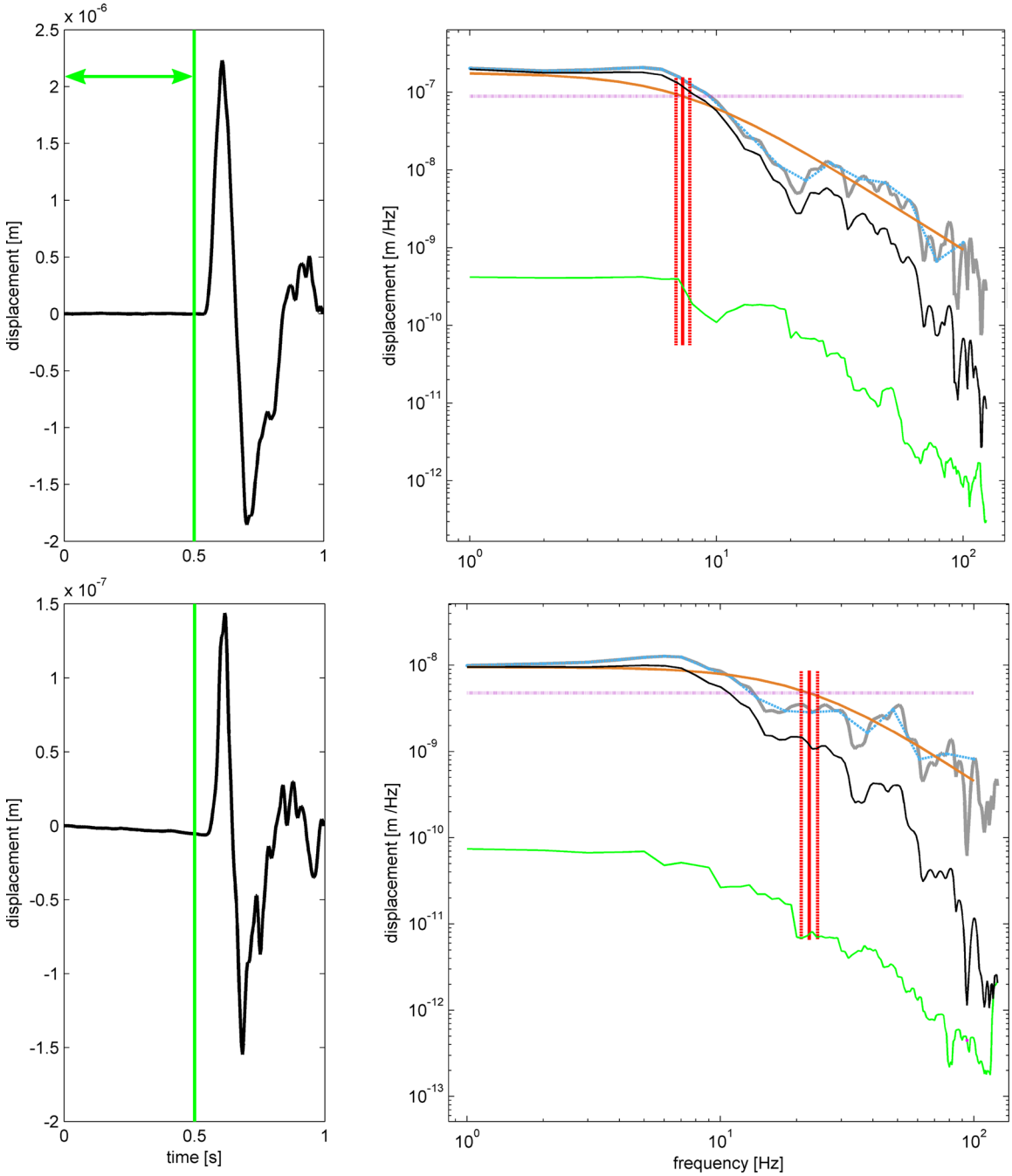

Figure 3. Ground displacement of the P pulse (left) with noise window marked by green arrow. Example of the spectral analysis (right) of event with (a) $M_L = 3.1$ (ID: X2411A) and (b) $M_L = 1.7$ (ID: X402A) at station BUBD. Black line is the observed spectrum, green line is the noise spectrum, both not corrected for Q. Observed spectrum (grey), interpolated observed spectrum (blue) and model spectrum (orange) are all corrected for $Q = 277$. The pink horizontal line is the half value of Ω_0 (intersection with spectrum line is at f_c for Brune's model). f_c (vertical red line) and its uncertainty estimates (dashed red line) were obtained by a single-station inversion of the corrected spectrum.

2.4 Scalar seismic moment

The low frequency spectral level Ω_0 was determined as a mean of $\Omega(f)$ for the three lowest frequencies (i.e. 1–3 Hz; MTT gives smooth and stable spectra) at each station. We can afford to fix the Ω_0 and not invert for it because the influence of Q in the low-frequency band is negligible (changes of Ω_0 are up to 2 per cent for Q between 200 and 400 and typical 2 s traveltimes). Moreover, Ω_0 can vary by factor of two just because of radiation pattern or directivity effects (e.g. Abercrombie & Rice 2005), which is discussed below.

Rupture velocity is assumed constant as 0.9β, where $\beta = 3.5$ km/s and $\alpha = \sqrt{3}\beta$. The rupture radius r is calculated according to

$$r = k\beta / f_c, \tag{3}$$

where $k = 0.32$ (Madariaga 1976). The seismic moment is determined as

$$M_0 = \frac{4\pi\rho\alpha^3 R\Omega_0}{\Re_{\Theta,\Phi} F} \tag{4}$$

(Brune 1970), where $\rho = 2700$ kg/m^3, R is hypocentral distance ($G(R) = R^{-1}$), $\Re_{\Theta,\Phi}$ is radiation pattern correction (Aki & Richards 2002) and F is the free surface amplification which is assumed constant equal to 2 because of the subvertical incidence of the P waves (Horálek *et al.* 2002). The radiation pattern correction is calculated for the typical fault plane orientation (strike $= 169^\circ$, dip $= 80^\circ$, rake $= -30^\circ$), which is almost the same for all events (Fischer & Horálek 2005). In our case, the effect of slightly varying focal mechanisms is not significant; variations of strike, dip and rake within the range of 10° can change the seismic moment by 10 per cent (in terms of the standard deviation of ratios of seismic moments over stations for two focal mechanisms). The seismic moment for each event is calculated as a mean of the logarithmic values from the available stations.

2.5 Stress drop

Stress drop is derived by using two approaches. First, directly from f_c after Eshelby (1957) as

$$\Delta\sigma = \frac{7}{16}\frac{M_0}{r^3} \tag{5}$$

As a second approach we applied the method of Andrews (1986) and Snoke (1987, eq. 3), which uses the integral of the square of the ground velocity spectrum J (after the attenuation correction; including the correction for limited bandwidth) for direct determination of f_c without the need for spectra inversion:

$$f_c(J) = \left(\frac{J}{2\pi^3\Omega_0^2}\right)^{1/3} \tag{6}$$

where $J = J_1 + J_{SP} + J_2$. The term J_{SP} is the integral value calculated from the spectrum. The correction for limited bandwidth in estimation of the integral J consist of two parts; the low frequency part J_1 which is negligible in our case (up to 0.1 per cent) and the high frequency part J_2, which can be more than 50 per cent if the attenuation correction is high (low Q) with respect to original spectrum. However, for our data the high frequency integral correction part is up to 30 per cent.

3 RESULTS

3.1 f_c and Q

Determination of f_c by spectra inversion is illustrated in Fig. 3. The observed spectrum (black) is corrected for attenuation (grey) and after logarithmic interpolation (blue) fitted by the model spectrum (orange). The resulting f_c is indicated by vertical red line, see more details in the figure caption. Fig. 4a shows the P-wave pulses at station SNED used for spectra inversion, sorted according to decreasing magnitude. The corresponding spectra (Fig. 4b) show a clear increase of the corner frequency with decreasing magnitude and decreasing low-frequency level. It is obvious (Fig. 4b) that the scaling between the f_c and Ω_0 is closer to f^{-4} than to f^{-3}, where the

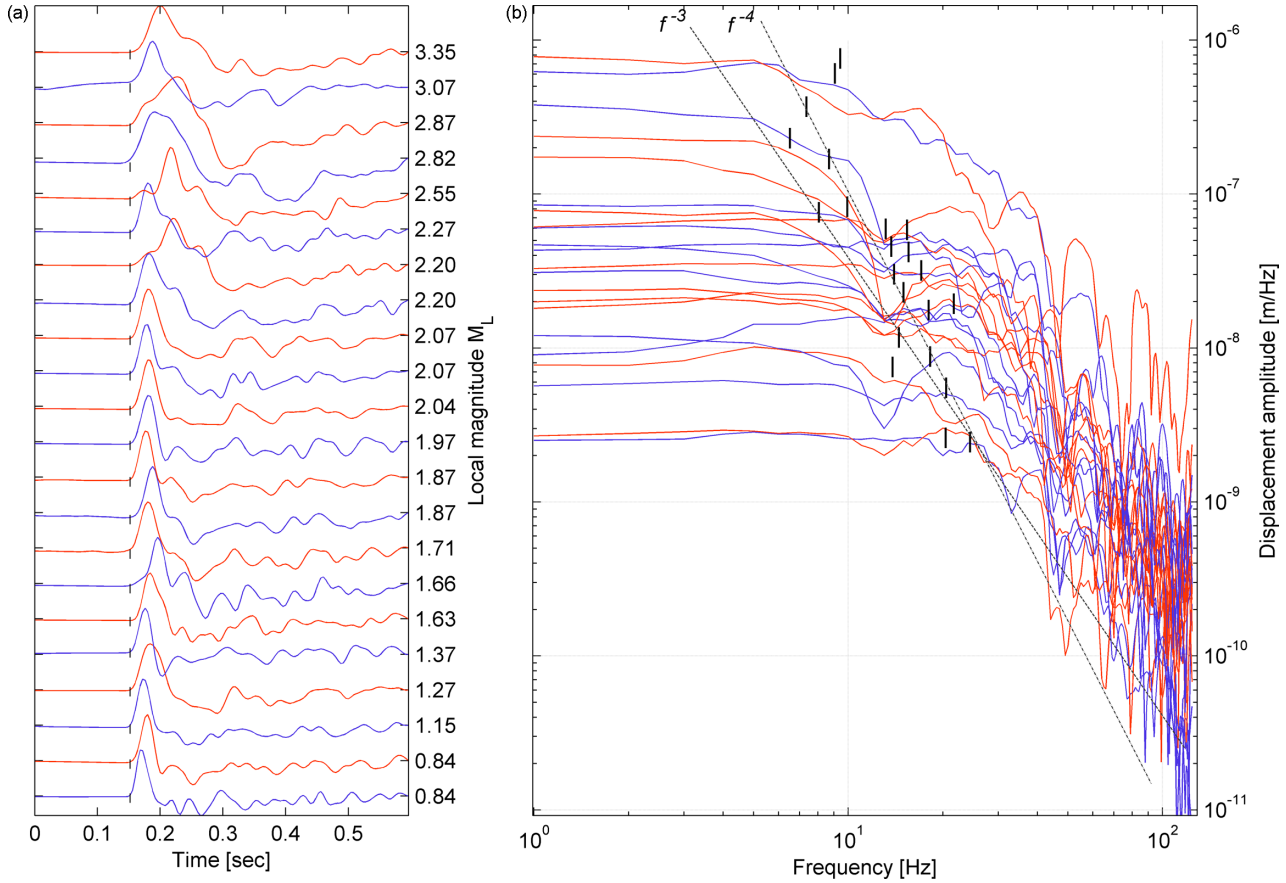

Figure 4. (a) Normalized unfiltered P pulses of displacement from the 2008 swarm sorted according to the decreasing magnitude and (b) the corresponding MTT amplitude spectra after attenuation correction at station SNED. The signals (a) are without correction for attenuation and therefore the time width of the pulses of the weak events are similar. The corner frequencies obtained from the inversion are marked as short vertical lines at Ω_0 amplitude level. It is obvious that the f_c scales as f^{-4} rather than f^{-3} (for constant stress drop).

later is expected for the constant stress drop. Without correction for attenuation of the spectra this dependence would be even steeper.

The way of estimating the uncertainty of the f_c is illustrated in Fig. 5 for a selected $M_L = 3.1$ event. After finding the optimal solution (f_c, Q_i; $i \in (1; N)$ stations; Fig. 5a) we test the trade-off between f_c and Q. To this purpose, we run repeatedly the inversion process for several fixed f_c in the vicinity of its optimal solution to search for the corresponding Q at individual stations. The resulting dependence of Q-factors on the selected f_c (Fig. 5b) shows that Q is almost constant at most of the stations excepting stations NKC and PLED (in this example). This shows that the optimal f_c is robust with respect to the applied correction for attenuation. To verify significance of the possible trade-off we performed a jackknife test by omitting individual stations from the inversion (Fig. 6). The results in Fig. 6a show that variations of the f_c for individual realizations stay within the range of the standard deviation of the solution found from all stations and omitting the problematic station does not decrease significantly the sum of residuals.

To test the sensitivity of Q at individual stations to omitting other stations from the inversion we plot in Fig. 6b the mean values of Q from all jackknife realizations. We find that all except three stations are performing well showing stable Q, independent of including other stations to the inversion. However, despite the three unstable stations, the resulting corner frequency remains stable within the standard deviation found from all stations (Fig. 6a). Note that the variation of f_c is within 7 per cent of the mean value found from all stations. The mean values of Q-factors resulting from inversion of all events range mostly from 80 to 600 (Table 1) with most common values between 150 and 300 at individual stations (median of all means is 230).

The uncertainty of f_c was estimated as an interval where the residual function increases by 5 per cent (grey circles in Fig. 5b).

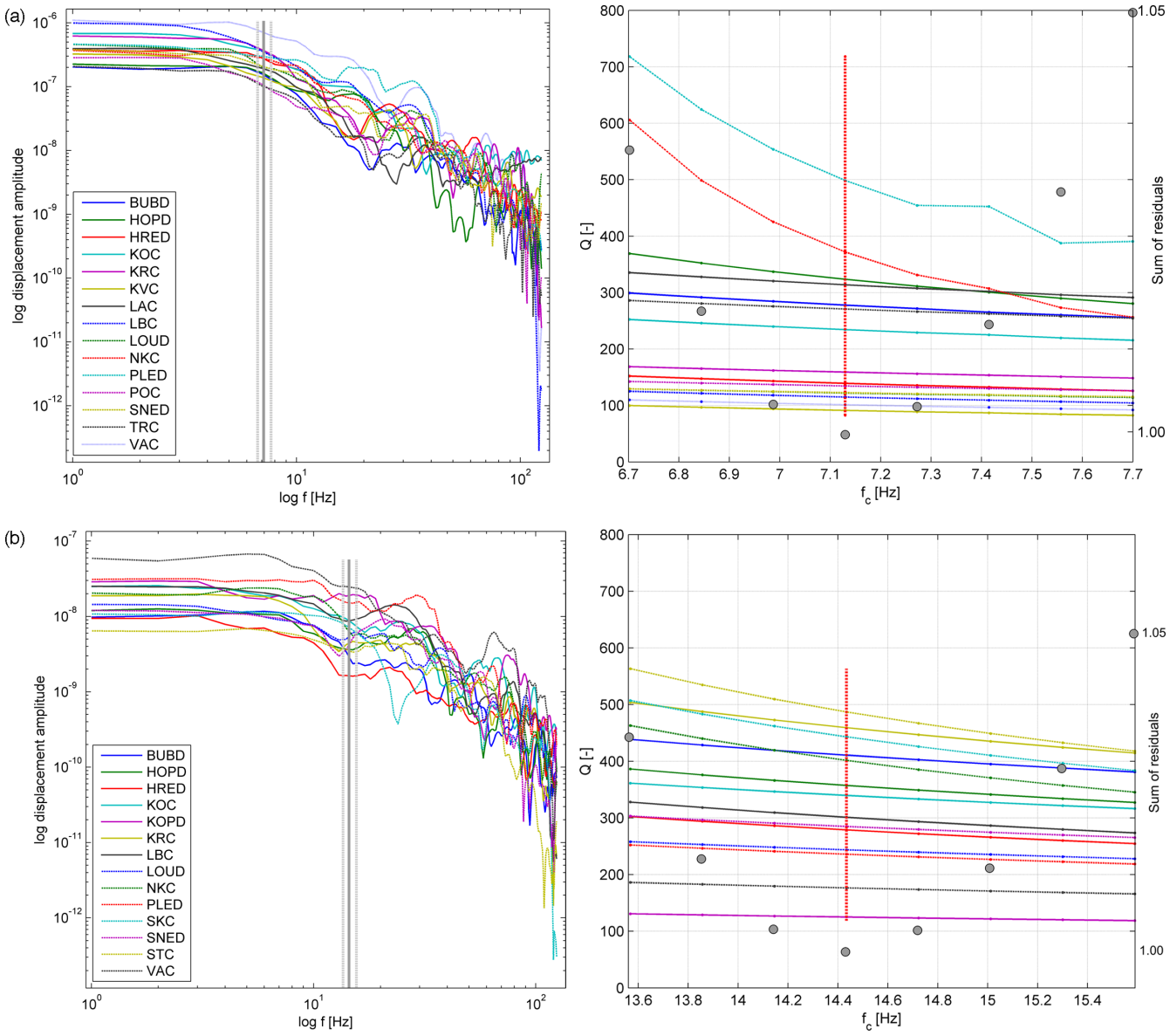

Figure 5. Example of inversion for single f_c and station-dependent Q for $M_L = 3.1$ (a) and $M_L = 1.7$ (b) events from Fig. 3. Spectra (left) are corrected for attenuation with Q corresponding to $f_c = 7.13$ and $f_c = 14.42$, respectively. (right) Testing of stability of Q for changing f_c in the range of ± 20 per cent around the minimum of the misfit function (grey circles). The f_c axis limits corresponds to the 5 per cent increase of the misfit function. These limits are plotted in left plots as dashed vertical lines. The legend on the left relates to both plots.

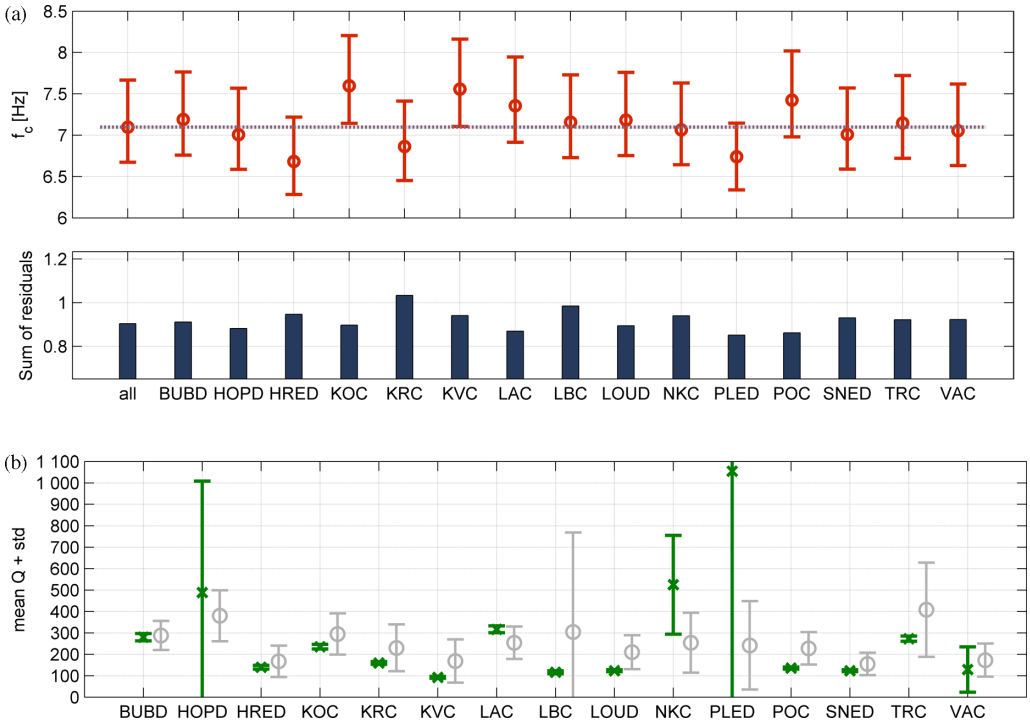

Figure 6. (a) Test of stability of the fitted parameter f_c in the inversion using the jackknife test with omitting individual stations for event $M_L = 3.1$ (id: X2411A). The first column named *all* is result of inversion including all suitable stations. Mean value of this f_c is marked by dashed purple line. (b) The mean values of Q at stations over all realizations of jackknife test (green). The corresponding values of Q resulting from using all events in this study are shown in grey.

Table 1. The quality factor Q for individual stations obtained as a mean value with its standard deviation. The number of available events for each station is in the last column.

Station	Q	errQ	numEv
BUBD	288	68	23
HOPD	380	119	19
HRED	167	74	22
KAC	224	119	15
KOC	295	97	51
KOPD	144	75	18
KRC	230	109	57
KVC	168	101	16
LAC	254	76	26
LBC	305	463	46
LOUD	210	79	24
NKC	254	140	14
PLED	242	206	20
POC	227	76	15
POLD	569	169	4
SNED	155	53	22
STC	208	102	38
TRC	408	220	16
VAC	173	77	48
ZHC	398	17	3

For most events the error does not exceed 1 Hz for small corner frequencies and 3 Hz for large corner frequencies (Table 2).

Finally, we compare corner frequencies obtained by spectra inversion with those determined by the method of Snoke (1987) (eq. 6). Fig. 7 shows the corner frequencies using two approaches: first the attenuation is neglected (black crosses) and second the attenuation is corrected for (red circles) by using the Q-factor estimated by spectra inversion. Snoke's corner frequency $f_c(J)$ is calculated at each station separately as a mean value for each event. In the ideal case, the relation between f_c*(inv)* and $f_c(J)$ should be 1:1. The linear regression has form

$$f_c(J) = 0.967\ f_c(\text{inv}) + 2.317 \qquad (7)$$

with correlation coefficient 0.986. The 95 per cent confidence interval is shaded by light red. There is a systematic shift (+ 2.317) of $f_c(J)$ which can be caused by overestimating the high-frequency correction term while evaluating the J integral after the attenuation correction. If the correction for attenuation is not applied the Snokes's method fails. It is found that if the spectra are corrected for attenuation the Snokes's method gives very similar corner frequencies as the spectra inversion method. Therefore, if we know the correct Q factors the corner frequency could be calculated directly from the corrected data without the inversion process. In the following, we use the corner frequencies determined by spectra inversion.

3.2 Effects of source mechanisms and directivity to M_0 and Q

The angular dependence of the radiation pattern of the source mechanisms affects the resolved scalar seismic moments. We corrected the amplitudes for a typical focal mechanism, which resulted in 15 per cent mean increase of scalar moments. However, the scatter of moments among stations has not decreased; the mean standard deviation of $\log_{10}(M_0)$ for all events before correction was 0.424 compared to 0.466 after the correction. We also tried to apply the individual radiation pattern corrections to events from 2008 for which the focal mechanism was known with sufficient precision but this also did not lead to significant decrease of the mean standard

Table 2. Source parameters.

ID	Date	Time	Lat	Lon	Depth (m)	M_L	M_0 (Nm)	f_c (Hz)	errf_c	r (m)	SD (MPa)	errSD (kPa)	Slip (mm)
X1466A	2008-10-10	03:22:05.110	50.20819	12.45497	8953	3.3	4.9e 14	9.4	0.8	118.8	128.8	66.0	337
X1590D	2008–10-09	22:20:37.760	50.21027	12.45352	9169	3.3	2.0e 14	9.1	0.7	123.5	46.5	23.8	126
X2411A	2008-10-10	11:18:41.466	50.21599	12.45199	9186	3.0	1.5e 14	7.4	0.4	152.2	18.6	4.0	62
P5559A	2000-11-06	23:31:32.660	50.20863	12.45690	8321	2.7	6.1e 13	15.5	0.9	72.5	70.0	15.1	112
X2002A	2008-10-10	04:22:16.491	50.21014	12.46008	8623	2.6	4.4e 13	8.7	0.7	128.8	9.1	4.7	26
P3282A	2000-09-17	15:14:32.939	50.21811	12.45345	8371	2.5	4.9e 13	9.6	0.6	116.5	13.7	3.0	35
P3887A	2000-10-15	19:11:20.533	50.20758	12.45900	8580	2.5	2.9e 13	12.7	0.6	88.1	18.6	2.3	36
P5342A	2000-11-05	01:05:04.577	50.20752	12.45778	8265	2.5	5.4e 12	23.2	1.9	48.2	20.9	10.7	22
X2144A	2008-10-10	06:34:48.785	50.20474	12.45650	8820	2.5	3.5e 13	9.9	0.8	112.7	10.7	5.5	27
P1197A	2000-09-03	17:11:03.056	50.21351	12.45320	9501	2.4	8.6e 12	30.1	2.4	37.2	73.3	37.5	60
P5164A	2000-10-29	05:10:46.834	50.21521	12.45554	7881	2.4	8.8e 13	6.5	0.5	173.2	7.4	2.5	28
X1590C	2008-10-09	22:20:33.917	50.20862	12.45419	9238	2.4	1.3e 14	6.5	0.5	171.7	11.3	5.8	43
P2179A	2000-09-08	09:14:00.927	50.21170	12.45369	9232	2.3	2.5e 13	15.5	0.9	72.1	29.4	6.4	47
X1893A	2008-10-10	03:18:36.206	50.20695	12.45487	9005	2.2	2.6e 13	13.7	1.0	81.7	21.1	7.2	38
X2136A	2008-10-10	06:27:20.585	50.20803	12.45488	9039	2.2	3.0e 13	8.1	0.6	138.8	4.9	2.5	15
X2678A	2008-10-10	16:20:35.324	50.21109	12.45492	9941	2.2	1.9e 13	14.7	0.9	75.9	18.9	4.1	32
X3730A	2008-10-12	06:39:48.481	50.21087	12.45447	8858	2.1	1.5e 13	15.6	1.7	72.0	17.3	23.0	27
P1237A	2000-09-03	18:23:50.733	50.21286	12.45285	9357	2.0	9.5e 12	15.2	0.8	73.5	10.4	1.3	17
P1442A	2000-09-03	23:38:12.296	50.22071	12.45097	8813	1.9	1.0e 13	11.4	0.5	98.1	4.9	0.3	10
P1900A	2000-09-04	16:18:12.444	50.21409	12.45359	8784	1.9	9.4e 12	10.1	0.6	111.0	3.0	0.7	7
P2278A	2000-09-08	12:00:15.233	50.21367	12.45304	9678	1.9	1.5e 13	12.9	0.8	86.8	10.0	2.2	19
X6694A	2008-10-21	03:02:43.457	50.22126	12.45113	8715	1.9	1.0e 13	15.4	1.5	72.8	11.5	11.5	18
X874A	2008-10-08	00:14:40.792	50.20390	12.45478	9719	1.9	8.1e 12	14.0	1.1	80.0	6.9	3.5	12
P1427A	2000-09-03	23:18:37.490	50.22087	12.45164	8809	1.8	5.7e 12	13.5	0.9	83.1	4.3	1.5	8
P3730A	2000-10-15	16:38:47.753	50.20650	12.45870	8876	1.8	2.6e 12	17.3	1.0	64.7	4.2	0.9	6
X1266A	2008-10-08	16:55:00.774	50.20904	12.45368	9138	1.8	4.5e 12	13.8	1.1	80.9	3.7	1.9	7
X1732A	2008-10-10	00:28:08.477	50.21286	12.45311	8889	1.8	5.4e 12	15.0	1.2	74.6	5.7	2.9	9
X2263A	2008-10-10	08:30:22.758	50.21483	12.45510	9102	1.8	4.7e 12	18.2	1.6	61.4	8.8	6.4	12
X3143A	2008-10-11	05:07:10.254	50.22131	12.45131	8930	1.8	1.6e 13	13.6	1.0	82.1	12.3	4.2	22
X3148A	2008-10-11	05:13:27.098	50.22111	12.45120	8669	1.8	1.2e 13	17.1	1.5	65.6	18.1	13.2	26
X840A	2008-10-07	23:49:32.974	50.20264	12.45675	9574	1.8	9.1e 12	21.7	1.9	51.7	28.8	21.0	33
P5475A	2000-11-06	22:11:37.679	50.21027	12.45565	8465	1.7	1.1e 13	9.4	0.7	119.8	2.7	0.9	7
P5516A	2000-11-06	22:51:59.989	50.20728	12.45931	7925	1.7	4.9e 12	21.0	1.5	53.4	14.1	4.8	17
P940A	2000-09-01	08:37:52.979	50.21285	12.45308	9720	1.7	5.2e 12	26.9	1.9	41.7	31.6	10.8	29
X1992A	2008-10-10	04:13:25.704	50.21246	12.45311	9554	1.7	6.2e 12	18.0	1.6	62.1	11.4	8.3	16
X3169A	2008-10-11	05:55:01.819	50.22073	12.45102	8772	1.7	1.1e 13	13.2	1.1	85.1	8.0	4.1	15
X402A	2008-10-06	03:47:54.129	50.19978	12.45766	9667	1.7	9.4e 12	14.5	1.0	77.2	8.9	3.1	15
P1210A	2000-09-03	17:27:29.689	50.21121	12.45378	9522	1.6	3.6e 12	17.3	1.0	64.6	5.8	1.3	8
P3752A	2000-10-15	16:56:54.116	50.20331	12.45910	8898	1.6	6.1e 12	24.9	2.0	44.9	29.4	15.1	29
P6415A	2000-11-09	04:02:52.333	50.20929	12.45448	9270	1.5	3.5e 11	33.7	3.7	33.2	4.1	5.5	3
P1479A	2000-09-04	00:16:13.569	50.21910	12.45147	8846	1.4	3.7e 12	12.0	0.7	93.2	2.0	0.4	4
P3781A	2000-10-15	17:18:44.156	50.21004	12.45487	9316	1.4	3.1e 12	21.3	1.3	52.6	9.2	2.0	11
P3833B	2000-10-15	18:15:01.676	50.20102	12.45829	8661	1.4	7.2e 11	17.6	1.6	63.7	1.2	0.9	2
P5517A	2000-11-06	22:53:44.166	50.20248	12.45804	9140	1.4	1.7e 12	20.5	1.6	54.7	4.5	2.3	5
P1070A	2000-09-03	12:47:05.706	50.21368	12.45317	9056	1.3	2.0e 12	26.2	1.8	42.8	11.0	3.8	10
P1237B	2000-09-03	18:23:49.674	50.21322	12.45229	9367	1.3	1.9e 12	22.6	1.6	49.6	6.9	2.4	8
P1311A	2000-09-03	20:38:54.595	50.21729	12.45264	8869	1.3	1.4e 12	23.0	1.4	48.7	5.4	1.2	6
X1153A	2008-10-08	06:20:50.839	50.20825	12.45418	9330	1.3	1.2e 12	20.5	1.8	54.6	3.4	2.4	4
P5247A	2000-10-29	09:35:20.188	50.21813	12.45385	7977	1.2	5.2e 11	40.1	4.4	27.9	10.4	13.8	6
P5627A	2000-11-07	00:38:12.095	50.20879	12.45470	9371	1.2	7.5e 11	20.4	1.6	54.8	2.0	1.0	2
P1373A	2000-09-03	22:14:29.709	50.21821	12.45191	8747	1.1	1.5e 12	31.5	2.8	35.6	14.3	10.4	11
X1240A	2008-10-08	14:11:49.501	50.20148	12.45758	9055	1.1	9.2e 11	24.4	2.2	45.9	4.2	3.1	4
X1462A	2008-10-09	12:48:36.360	50.21005	12.45396	9331	1.0	8.5e 11	20.4	2.0	54.9	2.2	2.2	3
P3533A	2000-09-19	10:30:42.102	50.21760	12.45158	9328	0.9	2.0e 12	30.9	2.5	36.3	18.3	9.4	15
P6304A	2000-11-08	04:51:11.492	50.20253	12.45741	9417	0.9	1.6e 11	24.7	2.0	45.4	0.7	0.4	1
P3997A	2000-10-16	01:38:42.663	50.20922	12.45422	9391	0.8	5.9e 11	29.7	3.3	37.8	4.8	6.3	4

deviation of the seismic moment (0.323 compared to 0.317 after individual corrections). We thus conclude that the radiation pattern correction does not significantly improve the variance of M_0 in our study.

In our study, we neglected the effects of directivity of the source by using the model of a point source. To test whether this simplification is justified we selected two different focal mechanisms from the 2008 swarm dataset (FM1 and FM3 following Vavryčuk *et al.* 2013), each including up to eight events. The directivity effect would be manifested by change of Q at stations, which are close to nodal lines for one FM type and farther away for another FM type. The result of this test is illustrated in Fig. 8. The mean Q factors range between 100 and 450 and are quite stable for both groups of events with standard deviation usually around 50. Besides, the Q

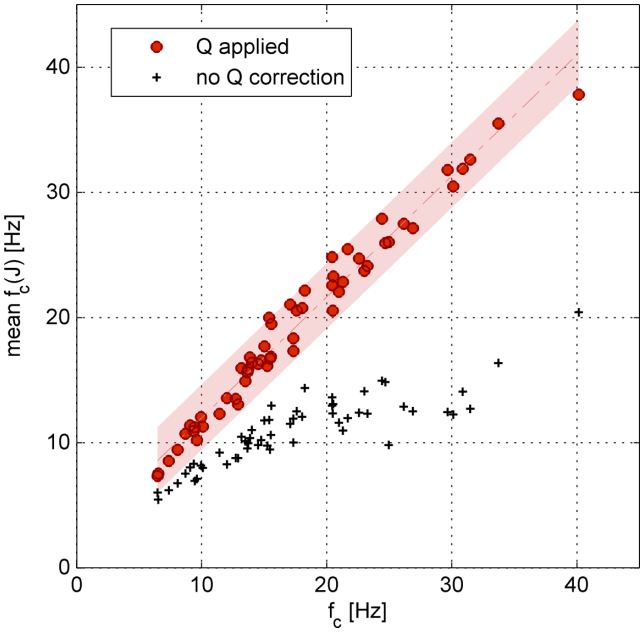

Figure 7. Comparison of two approaches for obtaining f_c—the inversion method and the Snoke's method (vertical axis). The linear regression is shown by red line and the 95 per cent confidence interval is shaded light red.

factors obtained from the two event groups are quite similar. If one omits the stations with too little events (less than 5) only HOPD and TRC show remarkable difference in Q-factors for the FM1 and FM3 groups. However, these two stations show almost the same position on the focal sphere for both FM types, which suggests that the possible directivity does not influence the station Q factors and indirectly also the corner frequency. This simple test shows that for the purpose of inversion for f_c the directivity effects can be included in event-dependent attenuation. In group FM1 are stronger events than in FM3 (Fig. 8c) and therefore the FM1 events were registered at more stations.

3.3 Scaling and stress drop

Fig. 9 shows the dependence of the corner frequency obtained by spectra inversion on seismic moment. Corner frequencies were converted to the rupture size using eq. (3); the resulting dependence of r on M_0 approximated by

$$r = 0.155 M_0^{0.206} \tag{8}$$

with the correlation coefficient 0.80. The rupture radii range from 25 to 200 m and the static stress drops between about 1 and 130 MPa. The error bars in Fig. 9 are for the rupture radii and are calculated from the uncertainty of f_c (in Table 2). These error estimates are most probably underestimated but at least provide the same relative measure of uncertainty for all events. A rather weak scaling of the source radius with seismic moment in the form $M_0{}^{0.206}$ is obtained, which points to the deviation from the constant stress-drop model that would correspond to the scaling in the form $M_0{}^{1/3}$. This is also expressed by the increase of stress drop with seismic moment (Fig. 10) in the form $\Delta\sigma \propto M_0{}^{0.43}$ indicating that events differing by two orders of seismic moment differ by one order in their stress drop. As shown in Fig. 11 the distribution of stress drops along the fault plane does not show any systematic pattern.

Assuming the constant stress-drop model, the slip D along the fault plane should scale similar to the source radius as $M_0{}^{1/3}$, which is found by comparing eq. (5) and the definition of seismic moment $M_0 = \mu DS$, where S is the rupture area. The weak increase of the source radius r with M_0 found in the data should be thus compensated by a stronger scaling of slip D with M_0. This is documented

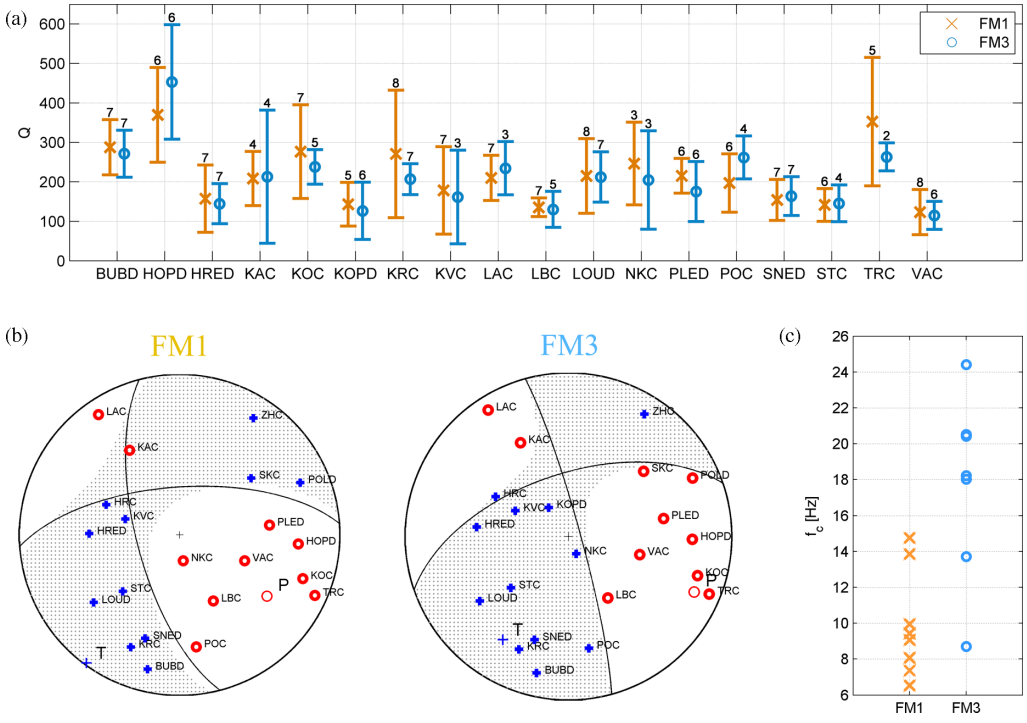

Figure 8. (a) Mean values and standard deviations of quality factors Q obtained for (b) two groups of focal mechanisms FM1 and FM3 (notation as in Vavryčuk et al. 2013). The number above the upper standard deviation limit in (a) is number of events from which the mean is calculated. (c) Corner frequencies of events in each FM group.

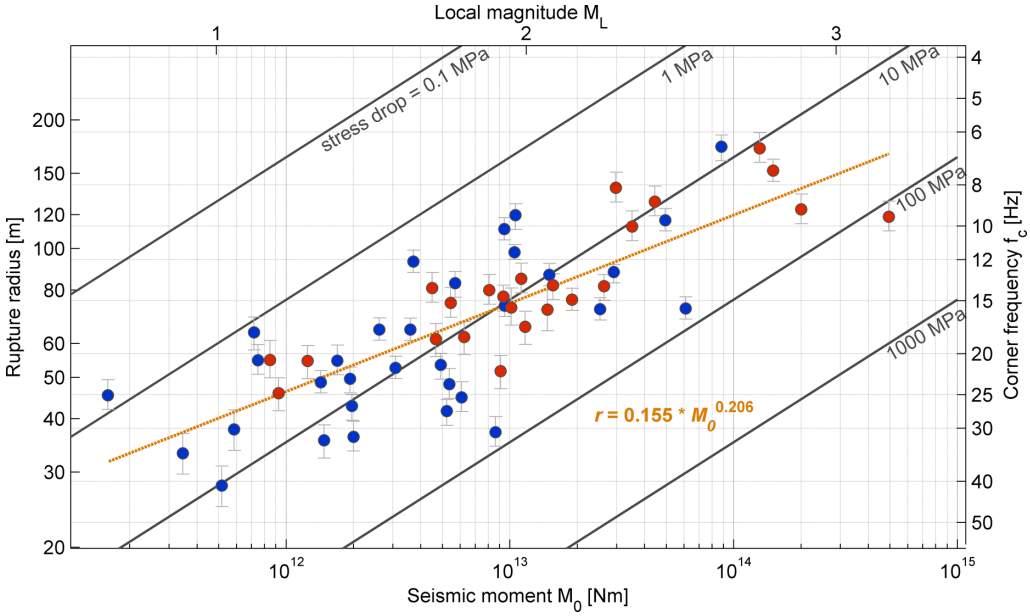

Figure 9. Dependence of the corner frequencies (right axis) and the rupture radii (left axis) on seismic moment obtained by spectra inversion method. The error bars are for rupture radii and are derived from the 5 per cent uncertainty of the f_c (flatness of the residual function). Blue circles are events from the 2000 swarm and red circles events from the 2008 swarm. The orange line is regression of rupture radius r on seismic moment for all the events together. The equation shows their possible relation (correlation coefficient is 0.80). The upper magnitude axis is scaled according to relation found from regression of M_L and M_0 (eq. 11, Fig. 14).

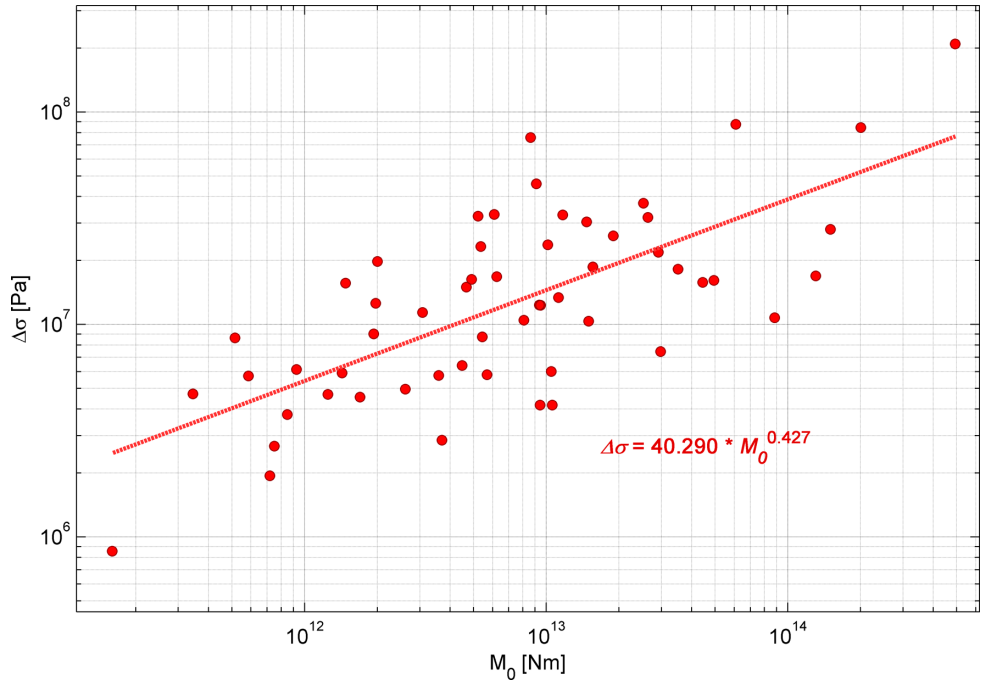

Figure 10. The dependence of the stress drop on the seismic moment. The correlation coefficients are $R(\Delta\sigma_{fc}) = 0.63$ and $R(\Delta\sigma_J) = 0.70$.

in Fig. 12 where the slip D is calculated from seismic moment and source radius. Linear regression in logarithmic scale gives (assuming a constant rigidity $\mu = \rho\beta^2 = 33.1$ GPa) the relation

$$\log D = 0.587 \log M_0 - 9.394 \qquad (9)$$

which shows scaling $D \sim {M_0}^{0.587}$ with much higher exponent that 0.33 expected for a constant stress drop model. The resulting seismic slip ranges from 1 mm to 30 cm for seismic moments between 1.5e11 and 5e14 Nm.

4 DISCUSSION

We analyzed the static source parameters of the earthquakes occurred during the West-Bohemia earthquake swarms 2000 and 2008. Despite the simplifications adopted and errors in the data we find that the obtained stress drop range 1–130 MPa and its tendency to increase with increasing seismic moment are robust results that point to partial breakdown in the self-similarity of the analyzed swarms earthquakes. The self-similarity could be thus understood in terms of the constant range of stress drops rather than strictly

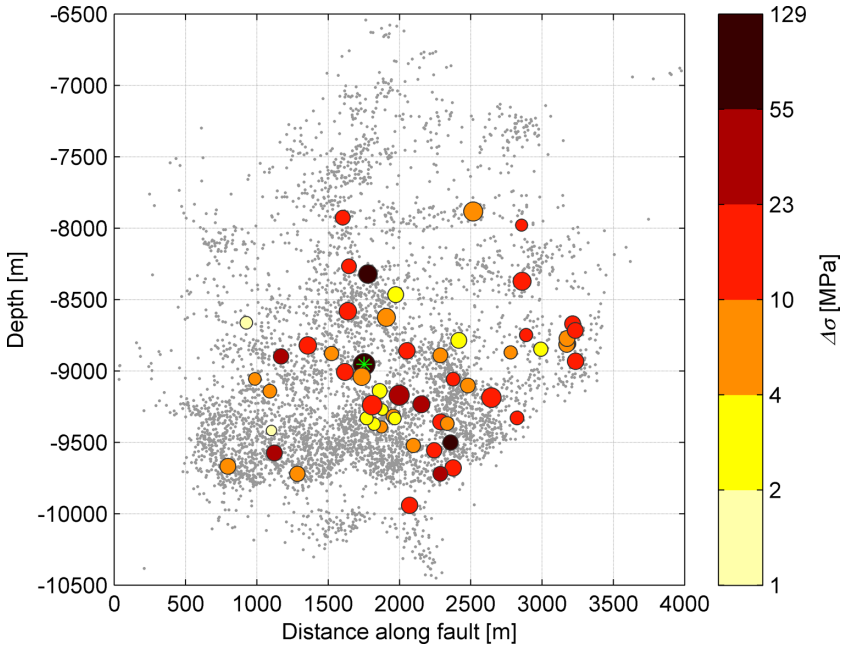

Figure 11. Distribution of stress drop along the fault plane. Event with stress drop higher than 100 MPa is highlighted by green star. Size of the circles corresponds to seismic moment (similar to Fig. 2).

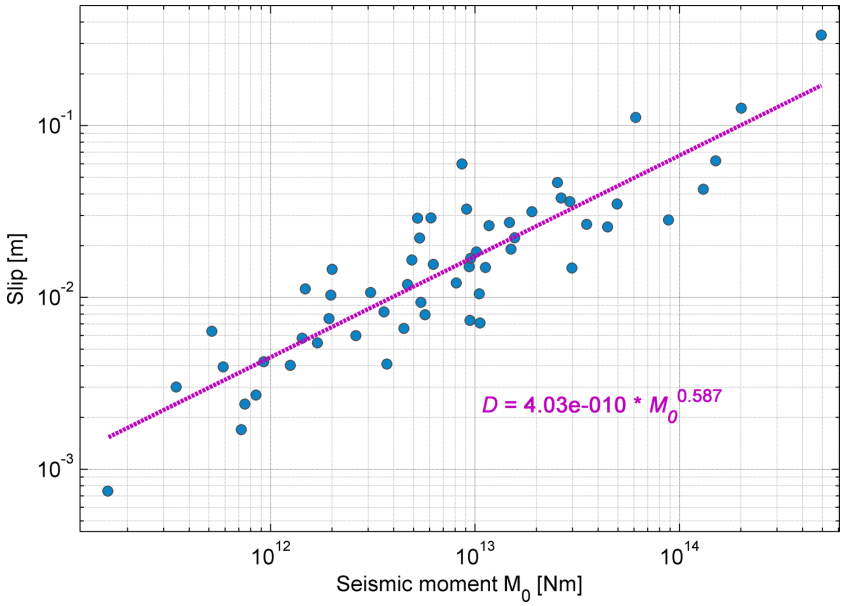

Figure 12. Slip as a function of seismic moment assuming $\mu = 33.1$ GPa. The correlation coefficient is 0.88.

the constant stress drop. In the following, we discuss the possible sources of errors and the resulting scaling relations.

4.1 Spectra estimation and correction for attenuation

The correct estimate of amplitude spectra affects both the resulting corner frequency and the low frequency level of the amplitude spectrum. We have used the MTT approach that gives smoother spectra than other tapers (Park *et al.* 1987). We found that MTT must be applied with care because using low values of time-bandwidth product (parameter *NW*), which favourably flattens the high-frequency amplitude oscillations leads to an artificial increase of the corner frequency whereas high values of *NW* are lacking of any advantages of MTT compared to cosine taper. In our analysis, we used $NW = 4$ (seven Slepian tapers). We tested the MTT method using the synthetic pulse in time window of 1 s length and we found that it performs well even at low frequencies and the bias is much less than using the simple cosine taper.

The anelastic attenuation has significant effect to widening the pulses and decreasing the corner frequencies. This is corrected by the frequency-dependent exponential term in eq. (2) for which the knowledge of Q-factor is essential. Because there is no independent estimate of attenuation for the area of interest we determined an event- and station-dependent Q as a part of the inversion for f_c. The correction for the Q-factor accounts also for the near-surface attenuation that is expressed by a sharp decrease of the spectral amplitudes above f_{max} (Hanks 1982). We do observe this type of decay in the observed spectra at some stations at frequencies above

60 Hz, which however does not overlap with the resulting corner frequencies ranging from 6 to 40 Hz. We thus infer that by limiting the analysis to the $M > 0.8$ events the near-surface attenuation does not affect the resolved corner frequencies. This is also manifested in Fig. 9 by the same scaling of f_c with M_0 for small and large events with no trend to leveling-off of f_c at small seismic moments.

4.2 Scaling relations

The dependence of the source radius on seismic moment (Fig. 9) shows a smaller increase than would be expected for the constant stress-drop model. With respect to the scatter of the resolved f_c and M_0 events differing by one order of seismic moment show the same source size.

Another measure of the similarity of physical processes governing earthquakes of different size is the apparent stress $\sigma_a = \mu E_P / M_0$, where E_P is the radiated energy of P waves calculated as

$$E_P = 4\pi\rho\alpha\langle\Re_{\Theta,\Phi}\rangle^2 \frac{R^2}{\Re^2_{\Theta,\Phi}} J \qquad (10)$$

(Boatwright & Fletcher 1984), where $\langle\Re_{\Theta,\Phi}\rangle = 0.52$ is the average radiation pattern correction for P waves. The radiated energy is calculated at each station separately and for the analysis we use the mean of E_P in logarithmic scale. The apparent stress gives the fraction of total energy radiated by seismic waves and typical values range from 0.01 to 10 MPa (e.g. Kwiatek *et al.* 2011). In Fig. 13 we show the apparent stress of our data set ranging over 2 orders from 0.001 to 0.1 MPa. As the apparent stress increases with the seismic moment we could deduce that the small earthquakes are less efficient in radiating of the energy than the bigger earthquakes, what supports the non-self-similarity (e.g. Aki 1967; Kanamori & Anderson 1975; Mayeda *et al.* 2005). Provided the seismic moment is well determined the values of apparent stress could be underestimated due to the possible underestimation of the radiated energy E_P via J. Although we applied the correction terms for bandwidth limitation of the records (Snoke 1987) it might be still insufficient because one should integrate up to the 10th multiple of the corner frequency to incorporate 90 per cent of the seismic energy (Ide & Beroza 2001). The upper limit in our recordings (either f_{max} or instrument limitations) is around 80–100 Hz, which indicates that for smaller events ($f_c > 15$ Hz; $\sim M_0 < 1e13$ Nm) the radiated seismic energy is proportionally underestimated. On the other hand the corner frequencies obtained from J are similar to those obtained by spectra inversion, which points to insignificant error in determining J.

The relation of seismic moment to local magnitude (Fig. 14)

$$\log M_0 = 1.38 M_L + 10.3, \qquad (11)$$

was obtained from the regression of seismic moment in log scale and local magnitude (correlation coefficient 0.912). The obtained scaling factor of 1.38 is significantly smaller than 1.5 present in the definition of moment magnitude M_W that was derived for a constant stress drop (Kanamori 1977), which gives an independent indication of the non-self-similarity of the analyzed swarm earthquakes.

5 CONCLUSIONS

We studied source parameters of the West Bohemia/Vogtland earthquake swarms 2000 and 2008 in the frequency domain and analyzed 56 events in the magnitude range M_L from 0.8 to 3.3 that were evenly distributed along the fault plane. Direct P waves from 3 to 18 stations at epicentral distances from 0 to 30 km were used. We compared two approaches to determine f_c; (i) spectra inversion using the ω^{-2} Brune's (1970) model to determine a single f_c and station-dependent attenuation correction and (ii) integration of spectra by the method of Snoke (1987). Results of our study, which is the first one addressing the earthquake swarms in the area, can be summarized as follows:

– The corner frequencies of the targeted events range from 6 to 40 Hz, which corresponds to the rupture radii in the range 28 to 150 m using the Madariaga (1976) source model for scalar moments from 1.5e11 to 5e14 Nm.

– The simultaneous inversion for f_c and Q resulted in Q-factor between 80 and 600 at different stations.

– We obtained a good fit between the results of spectra inversion and the Snoke's method, which qualifies the more simple Snoke's method to be applicable for routine determination of the static source parameters of small earthquakes in case that the quality factor Q is known and applied.

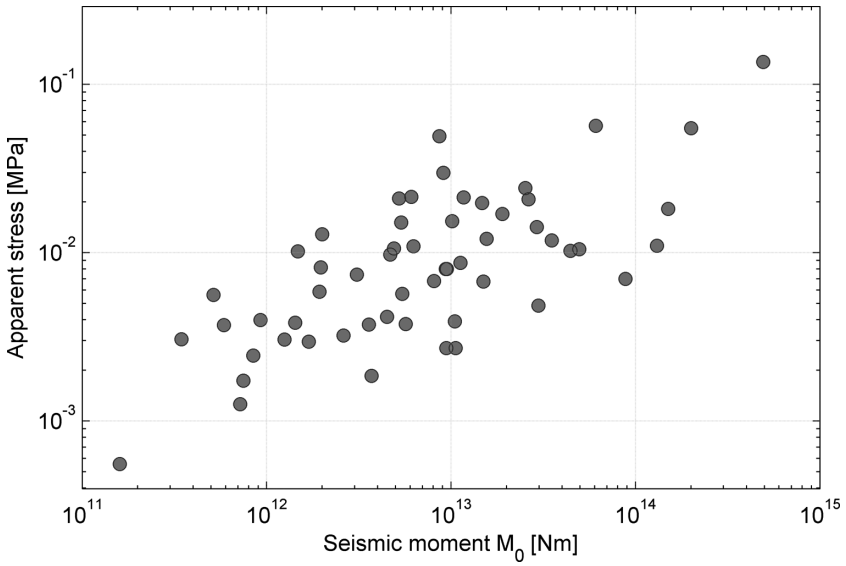

Figure 13. The dependence of the apparent stress on the seismic moment.

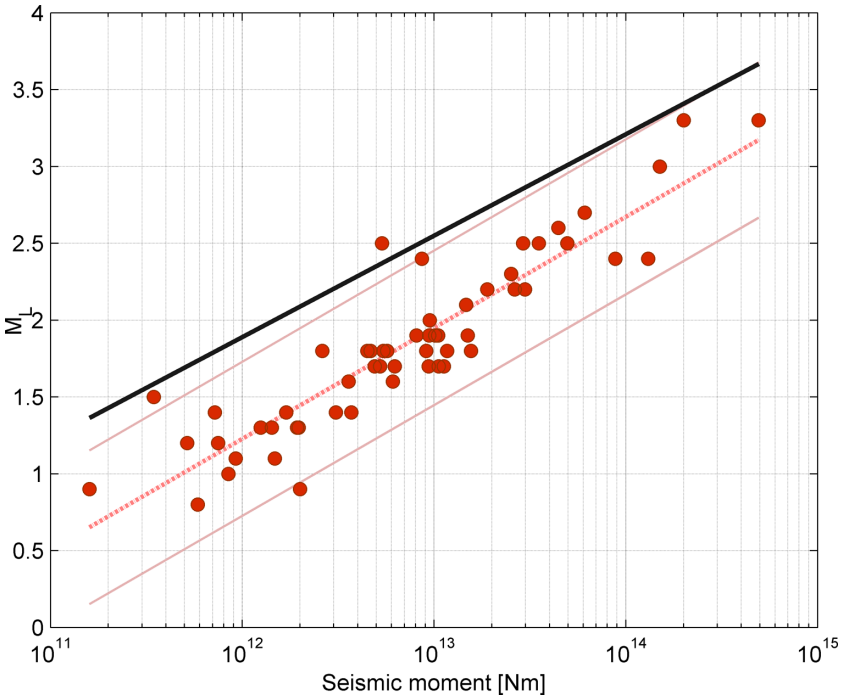

Figure 14. Linear regression between local magnitude M_L and seismic moment M_0 in log scale. The 95 per cent confidence interval is bounded by solid red lines. The relation for moment magnitude $M_W = 2/3^*\log M_0 - 6.03$ (Hanks & Kanamori 1979) is plotted by solid black line.

– Scaling of f_c with M_0 shows an exponent of 0.206, which is smaller than 0.33 that is expected for the constant stress drop model. We observe stress drops in the range from 0.7 to 128 MPa with a tendency to higher stress drops for larger events. The significance of the increase of stress drop with seismic moment is supported by the fact that the same scaling of f_c with M_0 occurs for small and large events.

– Apparent stress ranges over three orders from 0.002 to 2.2 MPa, which supports our finding that the West-Bohemia swarm earthquakes are non-self-similar. Further analysis including more events should be carried out to verify this conclusion.

Results of our analysis of static source parameters of earthquake swarms agree with the results of other authors: we find stress drops ranging between 1 and 130 MPa with a tendency to stress drop increase with increasing seismic moment.

ACKNOWLEDGEMENTS

We thank Josef Horálek, Jiří Zahradník and Václav Vavryčuk for fruitful discussions. The work was supported by Grant Agency of the Charles University, project No. 171310, Grant Agency of the Czech Republic, Grant P210/12/2451 and by the research project of the Ministry of Education of the Czech Republic MSM 0021620855. We also thank the reviewers Rachel Abercrombie, Simone Cesca and one anonymous reviewer for comments which helped to improve the manuscript.

REFERENCES

Abercrombie, R.E., 1995. Earthquake source scaling relationships from −1 to 5 M_L using seismograms recorded at 2.5-km depth, *J. geophys. Res.,* **100**(B12), 24 015–24 036.

Abercrombie, R.E. & Rice, J.R., 2005. Can observations of earthquake scaling constrain slip weakening? *Geophys. J. Int.,* **162**(2), 406–424.

Aki, K., 1967. Scaling law of seismic spectrum, *J. geophys. Res.,* **72**(4), 1217–1231.

Aki, K. & Richards, P.G., 2002. *Quantitative Seismology,* 2nd edn, University Science Books, 108 pp.

Andrews, D.J., 1986. Objective determination of source parameters and similarity of earthquakes of different size, in *Earthquake Source Mechanics,* Vol. 37, pp. 259–267, eds Das, S., Boatwright, J. & Scholz, Ch.H., American Geophysical Monograph.

Allmann, B.P. & Shearer, P.M., 2007. Spatial and temporal stress drop variations in small earthquakes near Parkfield, California, *J. geophys. Res.,* **112**(B4), 1–17.

Babuška, V. & Plomerová, J., 2008. Control of paths of quaternary volcanic products in western Bohemian Massif by rejuvenated Variscan triple junction of ancient microplates, *Stud. Geophys. Geod.,* **52,** 607–630.

Bankwitz, P., Schneider, G., Kämpf, H. & Bankwitz, E., 2003. Structural characteristics of epicentral areas in Central Europe: study case Cheb Basin (Czech Republic), *J. Geodyn.,* **35**(1–2), 5–32.

Boatwright, J., 1980. A spectral theory for circular seismic sources; simple estimates of source dimension, dynamic stress drop, and radiated seismic energy, *Bull. seism. Soc. Am.,* **70**(1), 1–27.

Boatwright, J. & Fletcher, J., 1984. The partition of radiated energy between P and S waves, *Bull. seism. Soc. Am.,* **74**(2), 361–376.

Bräuer, K., Kämpf, H., Niedermann, S., Strauch, G. & Tesar, J., 2008. The natural laboratory NW Bohemia—comprehensive fluid studies between 1992 and 2005 used to trace geodynamic processes, *Geochem. Geophys. Geosyst.,* **9,** Q04018, doi:10.1029/2007GC001921.

Brune, J., 1970. Tectonic stress and the spectra of seismic shear waves from earthquakes, *J. geophys. Res.,* **75**(26), 4997–5009.

Dahm, T., Fischer, T. & Hainzl, S., 2008. Mechanical intrusion models and their implications for the possibility of magma-driven swarms in NW Bohemia region, *Stud. Geophys. Geod.,* **52,** 529–548.

Dobrynina, A.A., 2009. Source parameters of the earthquakes of the Baikal rift system, *Izvestiya, Physi. Solid Earth,* **45**(12), 1093–1109.

Edwards, B. & Rietbrock, A., 2009. A Comparative study on attenuation and source-scaling relations in the Kanto, Tokai, and Chubu Regions of Japan, Using data from Hi-Net and KiK-Net, *Bull. seism. Soc. Am.,* **99**(4), 2435–2460.

Eshelby, J.D., 1957. The Determination Of elastic the field of an ellipsoidal inclusion, and related problems, in *Proceedings of the Royal Society of London,* pp. 376–396.

Fischer, T., 2005. Modeling of multiple-events using empirical Greens functions: method, application to swarm earthquakes and implications for their rupture propagation, *Geophys. J. Int.,* **163,** 991–1005.

Fischer, T. & Horálek, J., 2005. Slip-generated patterns of swarm microearthquakes from West Bohemia / Vogtland (central Europe): evidence of their triggering mechanism? *J. geophys. Res.,* **110,** B05S21, doi:10.1029/2004JB003363.

Fischer, T. & Michálek, J., 2008. Post 2000-swarm microearthquake activity in the principal focal zone of West Bohemia / Vogtland: space-time distribution and waveform similarity analysis, *Stud. Geophys. Geod.,* **52,** 493–511.

Fischer, T., Horálek, J., Michálek, J. & Boušková, A., 2010. The 2008-West Bohemia earthquake swarm in the light of the WEBNET network, *J. Seismol.,* **14,** 665–682.

Garcia-Garcia, J.M., Vidal, E., Romacho, M.D., Martin-Marfil, J.M., Posadas, A. & Luzn, E., 1996. Seismic source parameters for microearthquakes of the Granada basin (southern Spain), *Tectonophysics,* **261,** 51–66.

Hainzl, S. & Fischer, T., 2002. Indications for a successively triggered rupture growth underlying the 2000 earthquake swarm in Vogtland/NW-Bohemia, *J. geophys. Res.,* **107**(B12), 2338–2347.

Hainzl, S. & Ogata, Y., 2005. Detecting fluid signals in seismicity data through statistical modelling, *J. geophys. Res.,* **110,** B05S07, doi:10.1029/2004JB003247.

Hainzl, S., Fischer, T. & Dahm, T., 2012. Seismicity-based estimation of the driving fluid pressure in the case of swarm activity in Western Bohemia, *Geophys. J. Int.,* **191**(1), 271–281.

Hanks, T.C. & Kanamori, H., 1979. A moment magnitude scale, *J. geophys. Res.,* **84**(9), 2348–2350.

Hanks, T., 1982. fmax, *Bull. seism. Soc. Am.,* **72**(6), 1867–1879.

Harrington, R.M. & Brodsky, E.E., 2009. Source duration scales with magnitude differently for earthquakes on the San Andreas Fault and on Secondary Faults in Parkfield, California, *Bull. seism. Soc. Am.,* **99**(4), 2323–2334.

Horálek, J., Šílený, J. & Fischer, T., 2002. Moment tensors of the January 1997 earthquake swarm in NW Bohemia (Czech Republic): double couple vs. non-double couple events, *Tectonophysics,* **356**(1–3), 65–85.

Horálek, J. & Fischer, T., 2008. Role of crustal fluids in triggering the West Bohemia/Vogtland earthquake swarms: just what we know (a review), *Stud. Geophys. Geod.,* **52,** 455–478.

Horálek, J. & Fischer, T., 2010. Intraplate earthquake swarms in West Bohemia/Vogtland (Central Europe), *Joökull,* **60,** 67–87.

Horálek, J. & Šílený, J., 2013. Source mechanisms of the 2000-earthquake swarm in the West Bohemia/Vogtland region (Central Europe), *Geophys. J. Int.,* **194**(2), 979–999.

Ide, S. & Beroza, G., 2001. Does apparent stress vary with earthquake size? *Geophys. Res. Lett.,* **28**(17), 3349–3352.

Imanishi, K., Takeo, M. & Ellsworth, W., 2004. Source parameters and rupture velocities of microearthquakes in Western Nagano, Japan, determined using stopping phases, *Bull. seism. Soc. Am.,* **94**(5), 1762–1780.

Kolář, P. & Růžek, B., 2012. Finite seismic source parameters inferred from stopping phases for selected events of West Bohemia 2000 swarm, *Acta Geodynamica et Geomaterialia,* **9**(4), 435–447.

Kanamori, H. & Anderson, D., 1975. Theoretical basis of some empirical relations in seismology, *Bull. seism. Soc. Am.,* **65**(5), 1073–1095.

Kanamori, H., 1977. The energy release in great earthquakes, *J. geophys. Res.,* **82**(20), 2981–2987.

Kwiatek, G., Plenkers, K. & Dresen, G., 2011. Source parameters of picoseismicity recorded at Mponeng Deep Gold Mine, South Africa: implications for scaling relations, *Bull. seism. Soc. Am.,* **101**(6), 2592–2608.

Lindley, G. & Archuleta, R., 1992. Earthquake source parameters and the frequency dependence of attenuation at Coalinga, Mammoth Lakes, and the Santa Cruz Mountains, California, *J. geophys. Res.,* **97**(B10), 14 137–14 154.

Madariaga, R., 1976. Dynamics of an expanding circular fault, *Bull. seism. Soc. Am.,* **66**(3), 639–666.

Málek, J., Janský, J. & Horálek, J., 2000. Layered velocity models of the western Bohemia region, *Stud. Geophys. Geod.,* **44,** 475–490.

Mayeda, K., Gök, R., Walter, W.R. & Hofstetter, A., 2005. Evidence for non-constant energy/moment scaling from coda-derived source spectra, *Geophys. Res. Lett.,* **32,** L10306, doi:10.1029/2005gl022405.

Mertl, S. & Hausmann, H., 2009. Seismon – a flexible seismic processing software, in *Poster Presentation at EGU, General Assembly,* Vienna, Austria, 19–24 April 2009, Geophys. Res. Abst., Vol. 11, EGU2009-4266.

Michálek, J., Doubravová, J. & Mertl, S., 2011. Usage of SEISMON within the WEBNET seismic network, in *Poster Presentation at EGU, General Assembly,* Vienna, Austria, 03–08 April 2011, Geophys. Res. Abst., Vol. 13, EGU2011-6264.

Mrlina, J. *et al.*, 2009. Discovery of the first Quaternary maar in the Bohemian Massif, Central Europe, based on combined geophysical and geological surveys, *J. Volc. Geoth. Res.,* **182,** 97–112.

Oth, A., Bindi, D., Parolai, S. & Giacomo, D.D., 2010. Earthquake scaling characteristics and the scale-(in)dependence of seismic energy-to-moment ratio: Insights from KiK-net data in Japan, *Geophys. Res. Lett.,* **37,** 1–5.

Oye, V., Bungum, H. & Roth, M., 2005. Source parameters and scaling relations for mining-related seismicity within the Pyhäsalmi ore mine, Finland, *Bull. seism. Soc. Am.,* **95**(3), 1011–1026.

Park, J., Lindberg, C. & Vernon, F., 1987. Multitaper spectral analysis of high-frequency seismograms, *J. geophys. Res.,* **92,** 12 675–12 684.

Prieto, G.A., Shearer, P.M., Vernon, F.L. & Kilb, D., 2004. Earthquake source scaling and self-similarity estimation from stacking P and S spectra, *J. geophys. Res.,* **109**(B8), 1–13.

Sato, T. & Hirasawa, T., 1973. Body wave spectra from propagating shear cracks, *J. Phys. Earth,* **21**(4), 415–431.

Shearer, P.M., Prieto, G.A. & Hauksson, E., 2006. Comprehensive analysis of earthquake source spectra in southern California, *J. geophys. Res.,* **111,** 1–21, B06303, doi:10.1029/2005JB003979.

Shi, J., Kim, W. & Richards, P.G., 1998. The corner frequencies and stress drops of intraplate earthquakes in the northeastern United States, *Bull. seism. Soc. Am.,* **88**(2), 531–542.

Snoke, J., 1987. Stable determination of (Brune) stress drops, *Bull. seism. Soc. Am.,* **77**(2), 530–538.

Stein, S. & Wysession, M., 2003. *An Introduction to Seismology, Earthquakes, and Earth Structure,* Blackwell Publishing, 483 pp.

U.S. Geological Survey (USGS), 2002. Shuttle radar topography mission (SRTM) finished grade data 3-ARC. Available at: http://earthexplorer.usgs.gov/10.1093/gji/ggt286.html, last accessed 1 October 2012.

Urbancic, T. & Young, R., 1993. Space-time variations in source parameters of mining-induced seismic events with M<0, *Bull. seism. Soc. Am.,* **83**(2), 378–397.

Vavryčuk, V., 2002. Non-double-couple earthquakes of January 1997 in West Bohemia, Czech Republic: evidence of tensile faulting, *Geophys. J. Int.,* **149,** 364–373.

Vavryčuk, V., 2011. Tensile earthquakes: theory, modeling, and inversion, *J. geophys. Res.,* **116,** B12320, doi:10.1029/2011JB008770.

Vavryčuk, V., Bouchaala, F. & Fischer, T., 2013. High-resolution fault image from accurate locations and focal mechanisms of the 2008 swarm earthquakes in West Bohemia, Czech Republic, *Tectonophysics,* **590,** 189–195.

Viegas, G., Abercrombie, R.E. & Kim, W.Y., 2010. The 2002 M5 Au Sable Forks, NY, earthquake sequence: source scaling relationships and energy budget, *J. geophys. Res.,* **115,** 1–20.

Waldhauser, F. & Ellsworth, W., 2000. A double-difference earthquake location algorithm: method and application to the northern Hayward fault, California, *Bull. seism. Soc. Am.,* **90**(6), 1353–1368.

Yamada, T., Mori, J.J., Ide, S., Abercrombie, R.E., Kawakata, H., Nakatani, M., Iio, Y. & Ogasawara, H., 2007. Stress drops and radiated seismic energies of microearthquakes in a South African gold mine, *J. geophys. Res.,* **112**(B3), 1–12.